Universidad Pública de Navarra
Nafarroako Unibertsitate Publikoa

Doctoral thesis submitted for the degree of Doctor of Philosophy in Telecommunication Engineering

Waveplates based on Metasurfaces in the THz Range

Presented by: Alexia Moreno Peñarrubia

Supervisors: Dr. Miguel Beruete Díaz

Dr. Bakhtiyar Orazbayev

Pamplona - Iruña, August 2022

https://doi.org/10.48035/Tesis/2454/45639

upna

Universidad Pública de Navarra
Nafarroako Unibertsitate Publikoa

Abstract

Transmissive waveplates based on metasurfaces are key components in electromagnetism, as they allow for a full control of the electromagnetic wave polarization with the advantage of presenting structures more compact than conventional waveplates. Moreover, applying the Pancharatnam Berry (PB) principle to half-wave plate (HWP) metasurfaces allows the manipulation of wavefronts along with the conversion of the handedness of circularly polarized incident waves by simply rotating the meta-atoms that compose the metasurface. For achieving high levels of transmission efficiency with transmissive waveplates based on metasurfaces, multiple layer designs are usually required. It implies bulky structures and complicates the fabrication process, downplaying the aim of the use of metasurfaces.

The purpose of this thesis performed at the Public University of Navarre and at École Polytechnique Fédérale de Lausanne (EPFL) is to offer a technological advantage both for polarization controlling as wavefront manipulation and contribute to the development of metasurface-based devices, including their fabrication and experimental verification. The results include the following:

An ultrathin transmissive half-wave plate based on a bi-layered zigzag metasurface operating at the lower-frequency edge of the THz spectrum with a 90% of transmission efficiency, which is numerically and experimentally demonstrated. A detailed analysis of the device robustness with respect to layer misalignments is carried out by designing and fabricating two additional devices with the maximum possible shift between layers along both transverse directions.

A compact ultrathin metalens based on the Pancharatnam Berry principle with only two layers with a 90% of transmission efficiency, focusing the wavefront of a circularly polarized incident wave and converting its handedness. The structure is semi-analytically and numerically studied and experimentally measured, verifying an excellent behavior as HWP PB metalens at 87 GHz.

A wavefront engineering application for wavefront manipulation is numerically demonstrated in the millimeter-wave range by the integration of the metalens in an antenna-metalens system, which is semi-analytically studied and experimentally corroborated. The system converts the handedness of circular polarized waves, achieving an increment of the antenna directivity from17 dB to ~35 dB at 87 GHz with an AR lesser than 0.5 dB. Finally, two extra system configurations are presented to work around the frequency range extremes comprised between 75 GHz and 105 GHz, with directivities ~32 dB and AR < 3 dB.

Resumen

Los platos de onda basados en metasuperficies son componentes clave en electromagnetismo, ya que permiten un control total de la polarización de las ondas electromagnéticas con la ventaja de presentar estructuras más compactas que los platos de onda convencionales. Además, la aplicación del principio de Pancharatnam Berry (PB) a los platos de media onda (HWP) basados en metasuperficies, permite la manipulación de frentes de onda junto con la conversión de la polarización de las ondas incidentes circularmente polarizadas, simplemente girando los meta-átomos que componen la metasuperficie. Para lograr altos niveles de eficiencia de transmisión con platos de onda basados en metasuperficies, generalmente se requieren diseños multicapa. Esto implica estructuras voluminosas y complica el proceso de fabricación, restando importancia a la ventaja de utilizar metasuperficies.

El propósito de esta tesis realizada en la Universidad Pública de Navarra y en L'École Polytechnique Fédérale de Lausanne, Suiza (EPFL) es ofrecer una ventaja tecnológica tanto para el control de polarización como para la manipulación del frente de onda y contribuir al desarrollo de dispositivos basados en metamasuperficies, incluyendo su fabricación y verificación experimental. Los resultados incluyen lo siguiente:

Un plato de media onda operando en transmisión, ultradelgado y basado en una metasuperficie en zigzag de dos capas que opera en la parte baja del espectro del THz con un 90% de eficiencia de transmisión, que se demuestra numérica y experimentalmente. Se lleva a cabo un análisis detallado de la robustez del dispositivo con respecto a los desalineamientos de las capas mediante el diseño y la fabricación de dos dispositivos adicionales con el máximo desalineamiento entre capas en ambas direcciones transversales.

Una metalente ultradelgada y compacta basada en el principio Pancharatnam Berry con solo dos capas alcanzando un 90% de eficiencia de transmisión, enfocando el frente de onda de una onda incidente polarizada circularmente y convirtiendo su polarización. La estructura es estudiada semi-analítica y numéricamente y medida experimentalmente, comprobándose un excelente comportamiento como HWP PB metalente a 87 GHz.

Una aplicación de ingeniería de frentes de onda para la manipulación de los mismos se demuestra numéricamente en el rango de ondas milimétricas mediante la integración de la metalente en un sistema de antena-metalente, que se estudia semi-analíticamente y se corrobora experimentalmente. El sistema convierte la polarización de las ondas polarizadas circularmente, logrando un incremento de la directividad de antena de 17 dB a ~35 dB a 87 GHz con un AR inferior a 0.5 dB. Finalmente, se presentan dos configuraciones extra del sistema para trabajar entre los extremos del rango de frecuencia comprendido entre 75 GHz y 105 GHz, con directividades ~32 dB y AR < 3 dB.

Acknowledgments

This thesis has been possible thanks to the supervision of Bakhtiyar Orazbayev and Miguel Beruete Díaz. I owe most of my learning and evolution at this stage to them, especially thanking them for their understanding and affection in the difficult personal moments that I have gone through during the development of this thesis.

To my family. For the support of those who are still here and the effort of those who are no longer here. I would not have reached this place, nor at this time, nor would it make sense without you. Sister and mother, I love you. Three was always an even enough team.

To my colleagues and friends, for their tremendous human quality. For the fun moments, for the coffees to vent, for holding the spirits, the discouragement and the absurd moments. The warmth you have given me does not dissipate with distance. You all have made me grow and improve in one way or another. A hug for Alicia Torres, Jose Manuel Pérez, Enrique Vázquez, Ángel Ortega, Carlos Lezaun, David Navajas, Javier Chocarro, Carlos Quemada, Carlos Biurrun, Osmery Fernández, Dayan Pérez, Irati Jáuregui and Iñigo Liberal, for stimulating my critical thinking with intense hours of discussion on theoretical and philosophical matters, always useful and fun.

To my partner and ally during these years. For your valuable technical and personal advice, the moments of debate, your permanent support and your unconditional understanding and affection. You will always be my angel, Unai Beaskoetxea.

Thank you all.

Agradecimientos

Esta tesis ha sido posible gracias a la dirección de Bakhtiyar Orazbayev y Miguel Beruete Díaz. A ellos les debo la mayor parte de mi aprendizaje y evolución en esta etapa, agradeciendo especialmente su comprensión y cariño en los momentos personales difíciles que he atravesado durante el desarrollo de la misma.

A mi familia. Por el apoyo de quien sigue aquí y el esfuerzo de quien ya no está. Ni habría llegado a este lugar, ni a este tiempo, ni tendría sentido sin vosotras. Hermana y madre, os quiero. Tres siempre fue un equipo par y suficiente.

A mis compañeros y amigos, por su tremenda calidad humana. Por los momentos divertidos, por los cafés de desahogo, por aguantar el ánimo, el desánimo y los instantes absurdos. El calor que me habéis dado no se disipa con la distancia. Todos me habéis hecho crecer y mejorar de un modo u otro. Un abrazo para Alicia Torres, Jose Manuel Pérez, Enrique Vázquez, Ángel Ortega, Carlos Lezaun, David Navajas, Javier Chocarro, Carlos Quemada, Carlos Biurrun, Osmery Fernández, Dayan Pérez, Irati Jáuregui e Iñigo Liberal, por estimular mi pensamiento crítico con intensas horas de discusión en materia teórica y filosófica, siempre útiles y divertidas.

A mi compañero y aliado en todo momento durante estos años. Por tus valiosos consejos técnicos y personales, los momentos de debate, tu apoyo permanente y tu comprensión y cariño incondicionales. Siempre serás mi ángel, Unai Beaskoetxea.

Gracias a todos.

List of Figures

List of Tables

Content

Chapter 1. State of the Art

This introductory chapter presents an overview of the State of the Art with the aim to put the topic into perspective and highlight the importance of polarization controlling and wavefront manipulation using metasurfaces in the THz and MMW ranges. The attention is centered on half-waveplates metasurface-based which will be used in subsequent chapters to perform both functionalities, as well as the application of the Pancharatnam Berry principle to these structures, also crucial to set a theoretical basis for part of the work. At the end of this chapter, an outline of the document structure is presented.

1.1 Terahertz and Millimeter range Applications

The terahertz range (THz) is comprised between 100 GHz and 10 THz [1], [2] above the millimeter range and below the optical regime. As such, it draws upon techniques and knowledge from both domains to develop THz technologies, providing an opportunity to consolidate and reconcile the paradigms of microwave engineering with those of optics and photonics. The millimeter-wave band (MMW) is typically defined within the frequency range of 30–300 GHz, just above the microwave range and below the THz range. From a practical point of view, THz and MMW ranges are often overlapped (100–300 GHz) in the engineering community depending on the application involved and thus both bands result potentially useful for applications as spectroscopy, high-volume wireless communications, non-invasive medical imaging, sensing and safe security screening. Therefore, they cover a wide range of fields from biomedical to security and defense [3]–[12] [13]–[18]. Furthermore, MMW enables technology for 5G Cellular communications [19], [20].

Important actors of these applications are the development of the metamaterials. In order to define metamaterials, which is a very broad field, one can attend to their the common attributes [21], [22]: i) The structure can be described by a set of effective homogeneous electromagnetic parameters; ii) the parameters are determined by the collective response of small conducting resonators or meta-atoms; iii) the meta-atoms are placed periodically therein; and iv) the ratio of the operating wavelength to lattice constant is of the order of ten or more. Metamaterials can be engineered to provide a wide range of electromagnetic features at selected frequencies. This includes some characteristics not found in conventional materials, such as values of permittivity and permeability less than unity and even negative [23], overcoming conventional dielectrics commonly used in microwaves and optics. Hence the name “meta”, which implies “beyond” materials.

Bidimensional metamaterials are known as metasurfaces. The core concept of metamaterial and the analogue metasurface design is to craft materials by using artificially designed and fabricated structural units to achieve the desired properties and functionalities. These structural units (the constituent artificial meta-atoms) can be tailored in shape and size, the lattice constant and the ‘interatomic’ interaction can be artificially tuned, and ‘defects’ can be placed at desired locations. By engineering the arrangement of these nanoscale unit cells or meta-atoms into a desired architecture or geometry, it is possible to control both permittivity and permeability to tune the refractive index of the metamaterial to positive, near-zero or negative values and manipulate the waves in a subwavelength range, conferring properties to the entire structure which cannot be found in conventional material surfaces ([24]–[27]). Some examples of metasurfaces operating in THz and MMW for the applications mentioned in this section are depicted in Fig. 1.1.

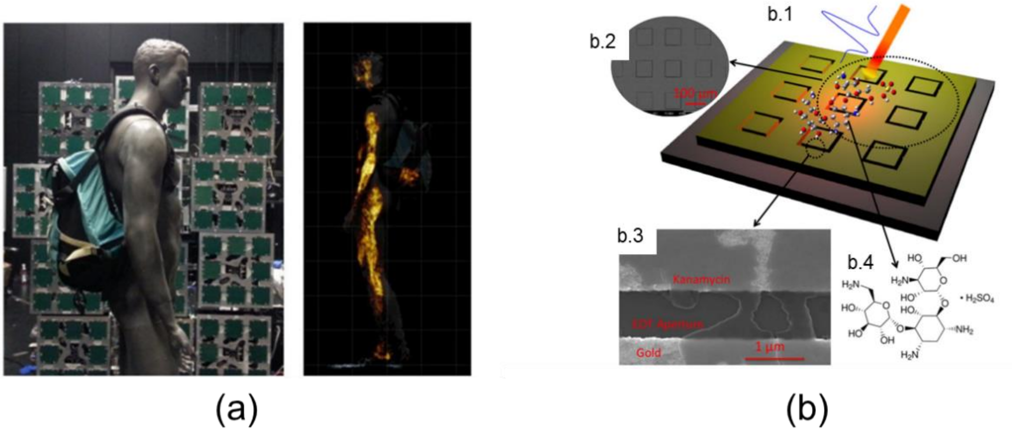

Fig. 1.1. (a) On the left, frequency-diverse screening system in the THz band, consisting of 12 submodules with 6 receiving and 2 transmitting metasurfaces and human-sized mannequin with a backpack containing potential threatening objects. On the right, THz mannequin image obtained with the system. Picture extracted with permission from [9]. (b) Antibiotic sensing application. Metasurface-assisted THz sensing of kanamycin sulfate. (b.1) Schematic of the metasurface structure with kanamycin sulfate molecules deposited on the surface. (b.2) and (b.3), scanning electron microscopy images of the metasurface. (b.4) Kanamycin sulfate molecular structure. Picture extracted with permission from [15].

1.2 Waveplates and Polarization Control

Polarization control devices are essential for a wide range of applications in THz systems, such as chiral structures in biology and chemistry [28] and polarization-division multiplexing for terahertz communications [29]. Polarization control includes polarization conversion [30]–[34] and polarization filtering [35], [36]. Both functionalities are schematized in Fig. 1.2.

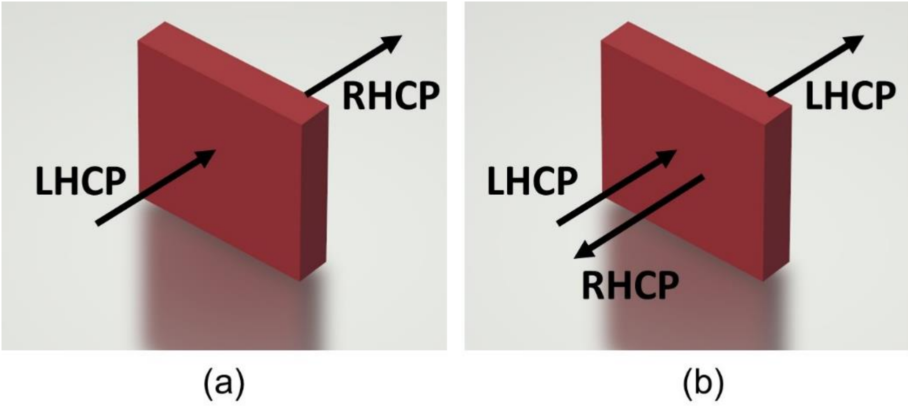

Fig. 1.2. Schematic view of (a) polarization conversion and (b) circular polarization filtering functionalities. In both examples, the red slab represents a metasurface.

The devices responsible for the control of the polarization state of waves are known as waveplates and conventionally they are made of anisotropic crystalline dielectric materials. Their operation mechanism can be explained in terms of phase retardation for orthogonal linear field components. Thereby, by modifying the thickness the slab, the phase difference between the two components can be tuned to get a specific polarization conversion at the operation frequency. However, this strategy usually leads to substantial thickness, narrow bandwidth, and high material losses. Moreover, at oblique incidence, a bulky waveplate exhibits phase deviation and a lateral shift in the beam path, leading to a significant decrease in bandwidth and efficiency. Furthermore, there is a lack of strongly anisotropic birefringent materials with low loss at terahertz frequencies.

As an alternative, metasurfaces have emerged as candidates for polarization control [37]. Highly efficient waveplates can be achieved using metasurface due to their capability of modifying locally the electromagnetic wave response within a subwavelength range. They present improved robustness at oblique incidence due to their subwavelength thicknesses and they can tailor the phase response of the two orthogonal polarization axes by tuning the resonance modes of their constituent meta-atoms. Thus, each individual element of a metasurface interacts locally with the incident wave to impose a phase response customizing the outgoing waves polarization. Besides, metasurfaces allow device miniaturization in a fully planar geometry compatible with conventional manufacturing techniques.

To realize polarization conversion, uniform metasurface waveplates are typically employed, which means that all meta-atoms are identical, see Fig. 1.3 for some examples. These meta-atoms collectively impose a different phase retardation for orthogonal polarization axes. They are referred as quarter waveplate (QWP) [31], [32], [38], [39] or half waveplate (HWP) [30], [34], [40] depending upon whether this phase retardation is 90 or 180 degrees, respectively.

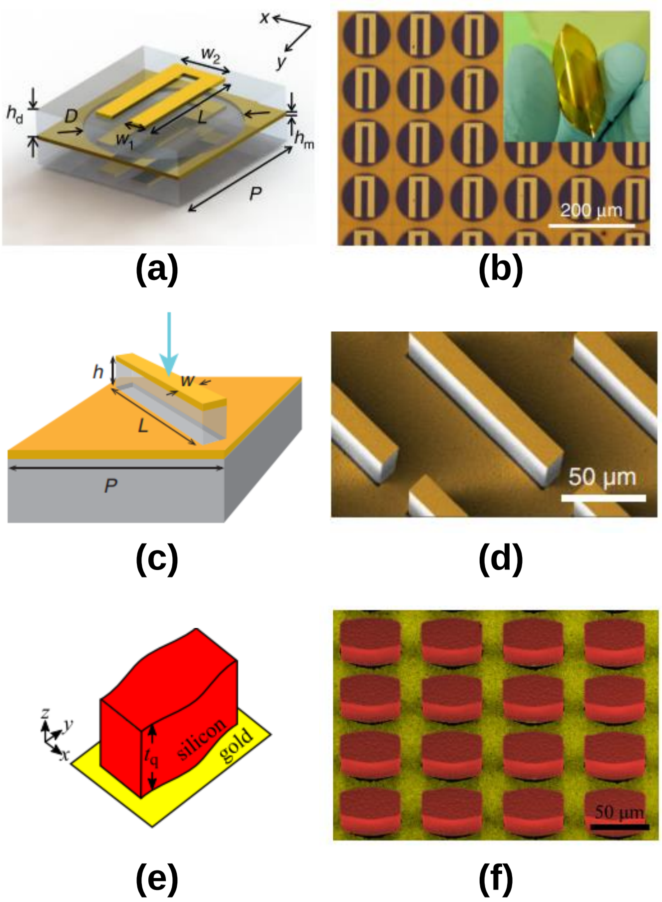

Fig. 1.3. (a)-(b), (c)-(d) and (e)-(f) corresponds with pictures extracted with the permission from [40], [32] and [31] respectively. The column in the left shows the constituent meta-atoms of the uniform metasurfaces depicted in the right column.

Furthermore, there are two ways in which waveplates can operate: reflection or transmission. Attending to the operation mode they are described by Jones matrix as follows,

$$\boldsymbol{R} = \begin{pmatrix} r_{xx} & 0 \\ 0 & r_{yy} \end{pmatrix} \quad \textbf{(1.1)}$$

$$\boldsymbol{T} = \begin{pmatrix} t_{xx} & 0 \\ 0 & t_{yy} \end{pmatrix} \quad \textbf{(1.2)}$$

where $\boldsymbol{R}$ and $\boldsymbol{T}$ are the ideal reflection and transmission Jones matrices [41], [42] respectively, with r_{xx}, r_{yy}, t_{xx} and t_{yy} denoting the reflection/transmission coefficients for the waves polarized along the x and y axes, respectively. Thus, an ideal waveplate operating in reflection and transmission mode with 100% of reflection/transmission efficiency, must obey conditions **(1.3)** and **(1.4)**, respectively.

$$|r_{xx}| = |r_{yy}| = 1, \qquad |t_{xx}| = |t_{yy}| = 0 \quad \textbf{(1.3)}$$

$$|r_{xx}| = |r_{yy}| = 0, \qquad |t_{xx}| = |t_{yy}| = 1 \quad \textbf{(1.4)}$$

In both cases, the phase retardation between orthogonal linear polarization components is defined respectively as

$$\arg(r_{xx}) - \arg(r_{yy}) = \varphi \qquad \arg(t_{xx}) - \arg(t_{yy}) = \varphi \qquad \textbf{(1.5)}$$

where φ = π/2 for QWP devices and φ = π for HWP devices. Some examples of reflective and transmissive metasurface waveplates extracted from the review of [37] are shown in Figs. 1.4 and 1.5, respectively.

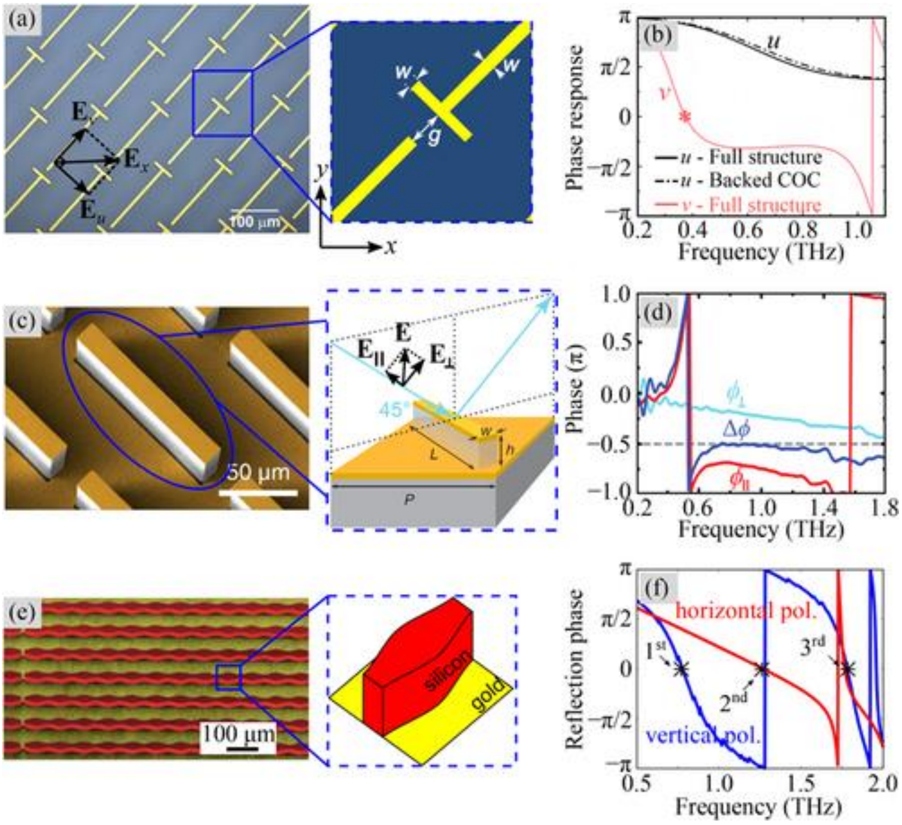

Fig. 1.4. Reflective metasurfaces for polarization control. (a) A linear polarization converter formed by slanted T-shaped resonators and (b) its simulated reflection phase analysis. (c) A quarter-wave metasurface based on gold-coated rectangular pillars and (d) its measured phase spectra for two orthogonal field components. (e) A half-wave metasurface, consisting of sinusoidal-shaped silicon resonators on a gold ground plane and (f) its simulated reflection phases for two orthogonal polarizations. The insets in (a), (c), and (e) show their respective unit cell geometries. The markers in (b) and (f) illustrate resonances of the structures. Picture extracted with the permission from [37].

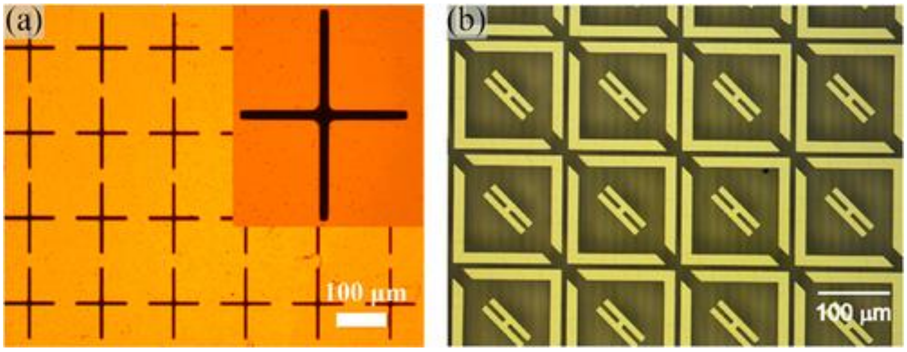

Fig. 1.5. Transmissive metasurfaces for polarization control. (a) Single-layer quarter-wave metasurface consisting of asymmetric cross slots. (b) Three-layer linear polarization converter based on metal gratings together with split-ring and H-shaped resonators. The image in (b) mainly shows resonators in the middle layer. Picture extracted with the permission from [37].

In this thesis we focus on HWP devices operating in transmission mode. These devices are significantly more challenging than those operating in reflection mode [43], [44]. Whilst reflective HWP can reach values of 100% reflection efficiency with a single layer structure, to fulfill the conditions for having a 100% efficient transmissive HWP, a minimum of two layers is required [34] to achieve simultaneously electric and magnetic response. As such, most of the transmissive HWP metasurfaces to date are based on multi-layer designs [30]. Their main disadvantage is a relatively bulky setup. However, they have more degrees of freedom to get an optimal transmissive HWP behavior. One remarkable work based on bi-layer structures are found in the literature [45]. This device accomplishes transmission efficiency values around 80% in a compact HWP with a thickness around $\lambda/10$, see Fig. 1.6.

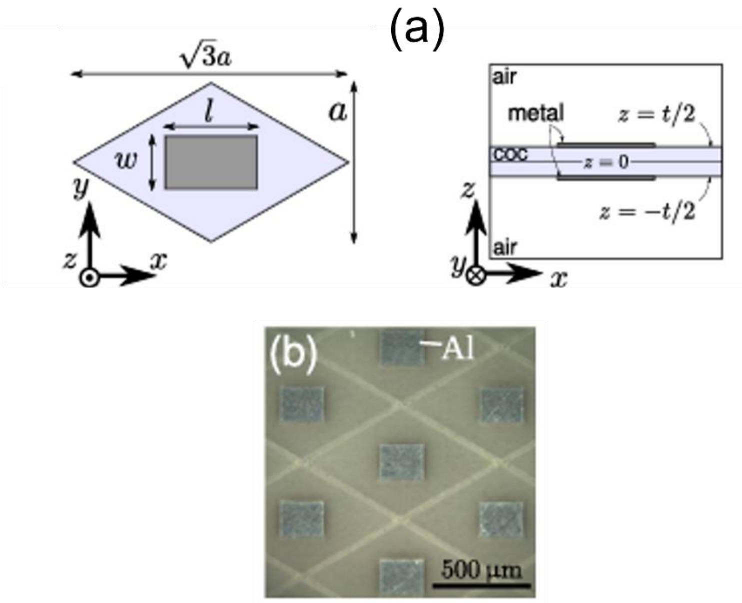

Fig. 1.6. (a) Two views of the bi-layered meta-atom and (b) Zoom view of part of the HWP metasurface. Picture extracted with the permission from [45].

1.3 Waveplates and Wavefront Engineering

The wavefront engineering concept arises from the idea to perform specific patterns in the near- or far- field region of a device for a variety of applications, such as collimate radiation from a point source [46], beam steering [47] or focusing [48]. Conventional wavefront controlling devices based on geometric optics, for instance, lenses, offer a large bandwidth and a low insertion loss. However, practical applications require both compactness and integrability, along with sophisticated functionality and tunability. These requirements are fulfilled by metasurfaces [49]–[51]. Here we will concentrate on metasurfaces operating at THz.

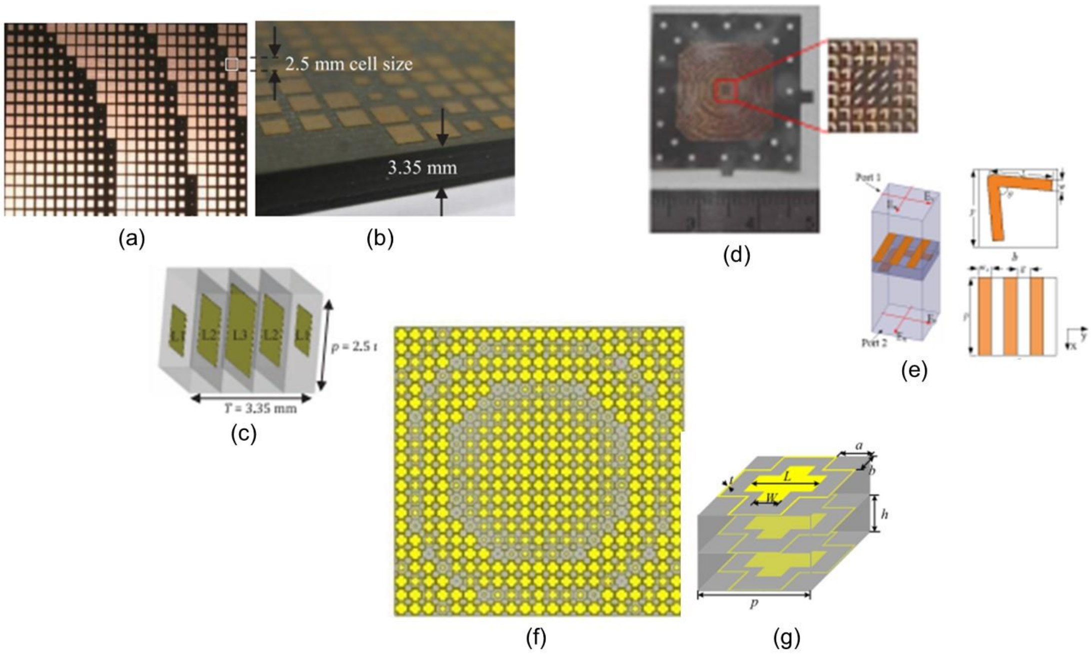

Fig. 1.7. Three examples of nonuniform metasurfaces designed for wavefront engineering. (a) and (b) Two views of part of a metalens and (c) meta-atom example. Extracted with the permission from [52] (d) Zoomed view of a transmitarray metasurface and (e) meta-atom example. Extracted with the permission from [53]. (f) and (g) Metalens and meta-atom example, respectively. Extracted with the permission from [54].

To carry out wavefront engineering using metasurfaces, a spatial phase distribution must be defined on the metasurface, in such a way that every constituent meta-atom introduces the proper phase value accordingly to the metasurface functionality. This spatial phase distribution is usually attained through two different approaches. In the first one, the wavefront-shaping is attained by a nonuniform metasurface made of nonidentical meta-atoms [52]–[58]. The phase response of a meta-atom is predominantly determined by its geometrical parameters. Each meta-atom introduces a phase discontinuity, and when assembled in the metasurface, they collectively alter the phase front of the outgoing waves. As a result, constructive interference takes place in the desired location or direction, while destructive interference happens elsewhere, leading to a prescribed radiation characteristic in the near- or far-field region. Typically, a complete phase coverage of 360 deg introduced by a set of meta-atoms at a specified frequency is necessary for full phase front control. In general, the larger the phase range the better. Thus, for this first approach, an important limitation is to achieve all the phase excursion while maintaining a high efficiency in transmission/reflection, since it is normally worked close to a resonance. Some examples of this sort of metasurfaces are shown in Fig. 1.7.

A completely different approach which ensures complete phase coverage of 360 deg is the use of the so-called Pancharatnam–Berry (PB) phase principle [59], [60]. This concept is associated with a polarization conversion and can be created by using anisotropic, subwavelength scatterers with identical geometric parameters but rotationally varying orientations. This principle can only be applied to HWP metasurfaces, working for circularly polarized incident waves and controlling the component of the circularly polarized transmission with the opposite handedness. Thereby, rotating a meta-atom by an angle θ, the extra phase obtained in that meta-atom position is equal to 2θ. A schematic of the operation principle is depicted in Fig. 1.8.

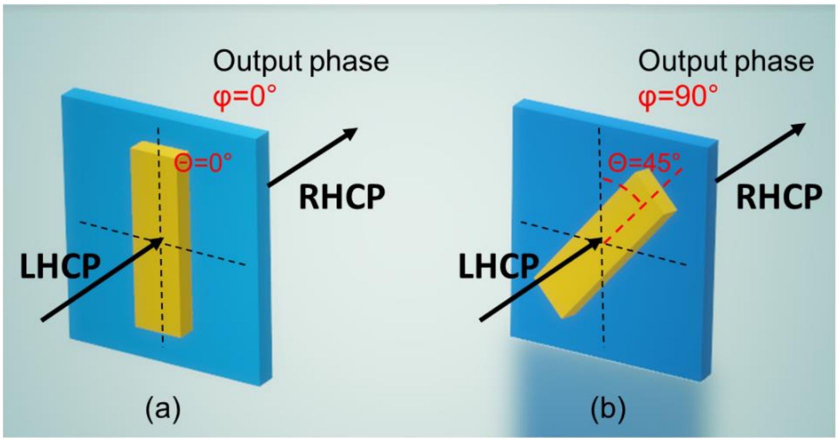

Fig. 1.8. Schematic of the Pancharatnam Berry operation principle applied to a HWP meta-atom. (a) nominal meta-atom (without rotation). (b) Meta-atom rotated 45°.

Pancharatnam–Berry metasurfaces (PBM) have been developed by applying the principle to HWP gradient index (GRIN) metasurfaces [61], [62]. In the last years, several PBM designs have been reported working in the THz range and K and Ka bands [40], [63]–[71]. The parameter used to evaluate the performance of PBM is the transmission efficiency, defined as the maximum level of crosspolar component amplitude at the output of the metasurface. In general, multilayer architectures are required to provide high levels of transmission efficiency. However, multilayer devices result in bulky structures which require intermediate substrate layers that entail strict alignment constraints and, more importantly, tight contact between them to avoid thin air layers that can ruin the performance. Tri-layer PBM designs have been developed, obtaining compact enough structures for controlling wavefronts [40], see Fig. 1.9(a). However, they are still challenging for fabrication due to the alignment constraints. On the other hand, single-layer devices only attain a maximum of 25% transmission efficiency [63], Fig. 1.9(b) and thus, bi-layered devices become more attractive for PBM development.

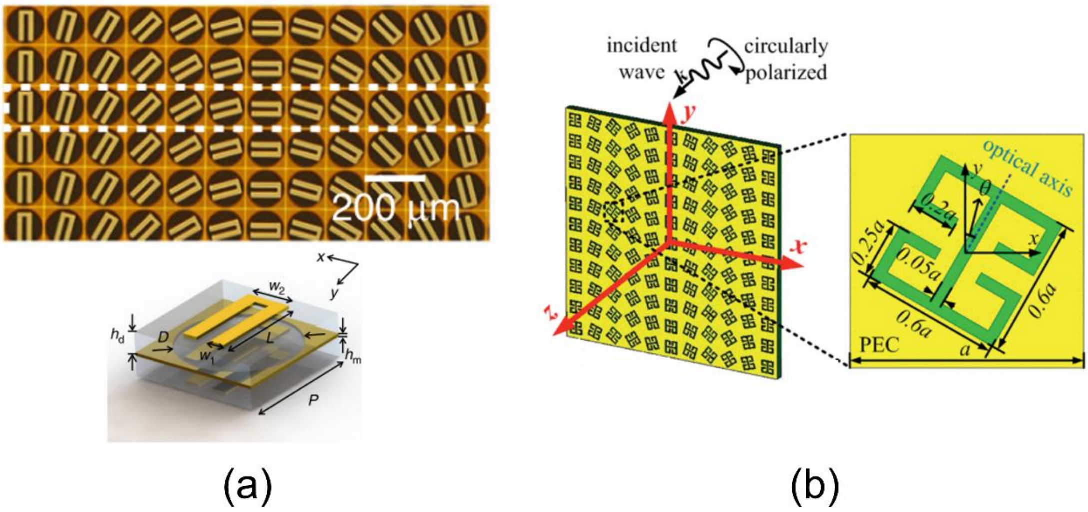

Fig. 1.9. (a) In top a picture of the metasurface is depicted. In bottom the tri-layered meta-atom schematic. (b) In the left image, a draft of the metasurface is shown and in the right image the single-layered meta-atom schematic. Images extracted with the permission from [40] and [63], respectively.

The pursuit of bi-layer devices with efficiency levels similar to tri-layer structures is a challenge, due to the reduced freedom to fine-tune the whole device's impedance matching. However, there are experimental and numerical demonstrations including a recent PB metalens which achieves a transmission efficiency of 82.7% (thickness below $\lambda/8$ [72]), see Fig. 1.10. Although this is a high-efficiency value, it remains below the best tri-layer designs [40].

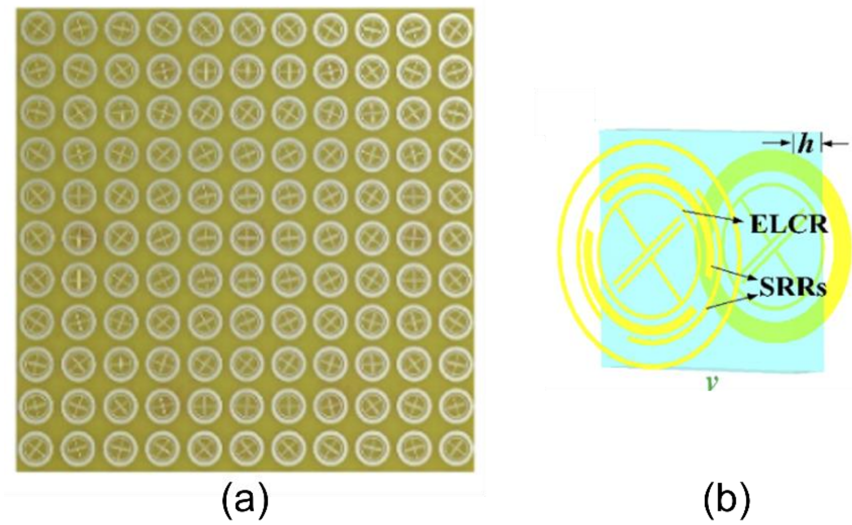

Fig. 1.10. (a) PBM for Vortex generation functionality and (b) bi-layered meta-atom of the structure. Extracted with the permission from [72].

1.4 Outline

The purpose of this thesis is to provide an overview of the research work on HWP metasurfaces and their applications performed during the doctorate program "Communication Technology" from Universidad Pública de Navarra (UPNA), for the degree of Doctor of Philosophy (PhD) in Telecommunications Engineering.

After the introductory State of the Art chapter, the work is divided in two main parts. In the first part, the design, fabrication, numerical study and experimental analysis of a bi-layered HWP for polarization control and two variants of this to test the device robustness are discussed. In the second part, a HWP metasurface based on the PB principle for wavefront engineering is presented and the design, fabrication, numerical and semi-analytical study and experimental analysis, as well as its integration in an antenna-metalens system which is also semi-analytically, numerically and experimentally demonstrated. Finally, the conclusions of the thesis and future lines are presented in chapter 4.

The theoretical principles used (Huygens-Fresnel´s principle) in the design and characterization of the metalens performances can be found in Appendix A. The theory applied to the results for polarization basis transformation is presented in Appendix B and the methods and equipment used for experimental verification of the performance of the fabricated devices, are given in Appendix C. At the end of the thesis, a summary of the author's merits can be found in Appendix D.

Chapter 2. Bi-layered Half-Wave Plate with High Conversion Efficiency

In this chapter, an ultrathin transmissive HWP based on a bi-layered zigzag metasurface operating at the lower frequency edge of the THz spectrum is numerically and experimentally studied. It achieves an amplitude transmission efficiency of over 90% and cross-polarization discrimination around 30 dB within a fractional bandwidth near 9% with a thickness less than $\lambda/20$ at the operation frequency. A detailed analysis of the device robustness with respect to layer misalignments is carried out by designing and fabricating two additional devices with the maximum possible shift between layers along both transverse directions. The chapter ends with a final study to ascertain a physical mechanism that explains the robustness of the device with respect to misalignments. These results complement and extend the reach of metasurfaces in the emerging THz band.

2.1 Background

Polarization is an intrinsic characteristic of electromagnetic waves, and its manipulation in a controlled way attracts an undoubted interest within the scientific community because of its high relevance in some applications, *e.g.*, communication systems [73]. Metasurfaces have led to a remarkable advancement in this field. In these devices, by designing individual unit cells instead of the entire structure, it is possible to manipulate the amplitude and phase of the electromagnetic waves and control the electromagnetic wavefront propagation. These days, with the ever-increasing demand for planar devices, research is shifting toward tunable devices and metasurfaces with novel functionalities [74] [75]. In this context, waveplates are vital components in photonics and modern optics, as they allow full control of the electromagnetic wave polarization.

2.1.1 Polarization and Waveplates

The polarization of an electromagnetic wave refers to the orientation of the oscillating electric field. Since electromagnetic waves are transverse waves, this vibration is perpendicular to the wave propagation direction and thereby defined in the transverse plane to this direction. Attending to the path described by this vibration in the transverse plane, three possible states are defined, linear (vibration describes a line), circular (vibration describes a circle) or elliptical (vibration describes an ellipse). As introduced in the first chapter, the polarization state of an electromagnetic wave can be modified when the wave crosses through devices that introduce a phase retardation between orthogonal linear polarization components. These devices are known as waveplates and depending on the retardation value they introduce, one can get a QWP (90 deg retardation) [76], [77] or a HWP (180 deg retardation) [78]. Waveplates made of conventional birefringent materials a present slightly different refraction index for both polarization components [79]. Thus, the component polarized along the fast axis encounters a lower index of refraction and travels faster through the waveplate than the component polarized along the slow axis. The output polarization state depends on the angle between the incident polarization components and the ratio between the fast and slow axis indices.

With the aim to facilitate the treatment of complicated polarization problems such as the propagation of waves through several polarizing components such as the waveplates, in 1941 Clark Jones developed a matrix calculus [80] initially intended for the study of optical systems but applicable to generalized electromagnetic problems. This Jones calculus involves two-by-one and two-by-two matrices (Jones vector and Jones matrix respectively) with matrix elements which are in general complex. Thus, the polarization state of an electromagnetic plane wave propagating along the *z*-axis can be represented by the Jones vector in the complex plane by the amplitudes (A_x, A_y) and phases (δ_x, δ_y) of the transverse electric field components [80] as follows,

$$\vec{J} = \begin{bmatrix} \tilde{E}_x \\ \tilde{E}_y \end{bmatrix} = \begin{bmatrix} A_x e^{i\delta x} \\ A_y e^{i\delta y} \end{bmatrix}, \tag{2.1}$$

where $\tilde{E}_x$ and $\tilde{E}_y$ are the complex amplitudes of the electric field. In Fig. 2.1 the linear relationship between the polarization components of a wave before and after going through a waveplate is schematized on top. This linear relationship between input and output polarization components can be expressed as,

$$\begin{aligned} E_x^o &= M_{xx}E_x^i + M_{xy}E_y^i \\ E_y^o &= M_{yx}E_x^i + M_{yy}E_y^i \end{aligned} \tag{2.2}$$

Being E_x^l and E_y^l, the orthogonal polarization components for the incident ($l = i$) and output ($l = o$) waves and $M_{xx}, M_{xy}, M_{yx}, M_{yy}$ the transformation factors applied to the field components by the waveplate. This system can be rewritten as a function of Jones vectors and Jones matrices as,

$$\begin{bmatrix} E_x \\ E_y \end{bmatrix}^o = \begin{bmatrix} M_{xx} & M_{xy} \\ M_{yx} & M_{yy} \end{bmatrix} \begin{bmatrix} E_x \\ E_y \end{bmatrix}^i \quad \text{or} \quad \overrightarrow{J^o} = \boldsymbol{M}\overrightarrow{J^i}, \tag{2.3}$$

where $\boldsymbol{M} = \begin{bmatrix} M_{xx} & M_{xy} \\ M_{yx} & M_{yy} \end{bmatrix}$ is a complex matrix called Jones matrix and $\vec{J^o}$ and $\vec{J^i}$ are the Jones vectors for the input and output waves, respectively. The crossed terms M_{xy}, M_{yx} = 0 for a waveplate with axes aligned with x and y. In addition, and ideal waveplate with total transmission has $|M_{xx}|$, $|M_{yy}| = 1$. Hence, the Jones matrix can be written as follows,

$$\boldsymbol{M} = e^{i\phi} \begin{bmatrix} e^{i\frac{\varphi}{2}} & 0 \\ 0 & e^{-i\frac{\varphi}{2}} \end{bmatrix}, \quad \textbf{(2.4)}$$

Where ϕ is the phase factor or phasor common for both axes and for simplicity it is usually omitted. For a waveplate, the parameter of interest is the phase difference or retardation between orthogonal polarization components, ($\varphi = \delta y - \delta x$). Thus, for a QWP, this value is φ=$\pm$ 90 deg and for a HWP, φ= $\pm$180 deg. The sign depends on the alignment of the polarization components respect to the fast and slow axis.

In Fig. 2.1(b) two examples of polarization transformation for a QWP and a HWP cases are depicted assuming an incident wave with linear polarization at 45° and a right-handed circular polarization, respectively. The output polarization state can be easily obtained using Jones calculus in both cases.

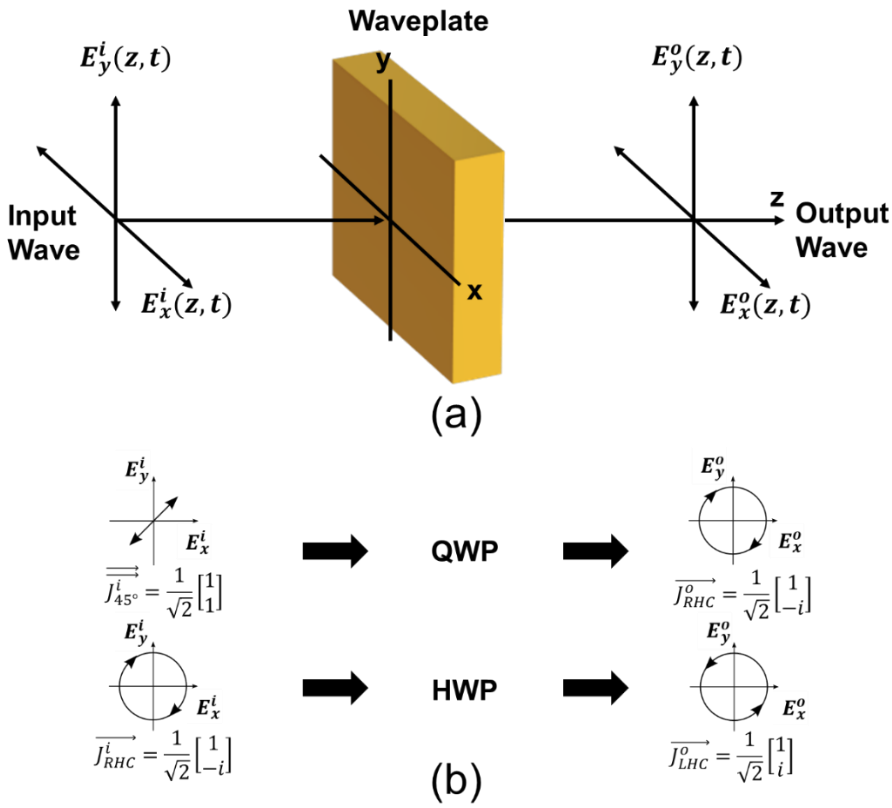

Fig. 2.1. (a) Schematic of the linear relationship between the polarization components of a wave before and after going through a waveplate. (b) QWP and HWP functionality examples for two different polarization states in each case.

2.1.2 Waveplates based on Metasurfaces

In the previous section, waveplates based on conventional birefringent materials were briefly introduced. These structures are key for polarization control and they are based on the accumulated retardation between two orthogonally polarized electric fields when the wave propagates a distance much larger than its wavelength in the birefringent material. The reason is that waveplates are mainly used at optical frequencies where the wavelength is on the order of microns. Added to this is the fact that the ordinary and extraordinary indices of birefringent materials are normally very similar. Therefore, to accumulate a significant phase difference, the wave must travel a large distance compared to the wavelength. Often, this results in bulky configurations and limits the functionalities when compactness is required. With the rise of the metasurfaces unprecedented capabilities for manipulating waves in surface-confined configurations with subwavelength spatial resolutions have emerged, all with planar elements that ensure compactness and facilitate integration compatibility. Thus, in the last few years numerous researchers have proposed designs based on anisotropic, bianisotropic, and chiral metasurfaces [81]–[84].

The operation principle of waveplates based on metasurfaces is the same as for those based in birefringent metamaterials and the Jones calculus applies in the same way. However, unlike birefringent materials that introduce a continuous phase retardation, the phase retardation introduced by the metasurfaces involves an abrupt change as it must take place within a deeply subwavelength thickness. Despite the advantage of these compact devices, the realization of ultrathin metasurfaces waveplates implies a huge design challenge, especially when they operate in transmission mode. In fact, most examples of HWP working at THz found in literature operate in reflection mode, [43], [44]. This is due to the difficulty of achieving a high level of transmission efficiency (given by the amplitude of the desired output polarization state) with a small number of metasurface layers. Thus, usually, devices achieving 100% of efficiency require of multilayer designs [85], [86]. Moreover, as it was mentioned in the previous chapter, the minimum number of layers required to get the simultaneous fine-tuning between the electric and magnetic response to get a 100% of transmission efficiency is two, since a single-layer device only attains a maximum of 25% transmission efficiency [63].

There are numerous QWP designs with high transmission efficiency levels [38], [87], [88]. However, HWP designs reaching similar levels of efficiency to QWP with a small number of layers are less common in the literature. A remarkable THz bi-layer HWP was demonstrated in [45] using cut-wire-pairs metasurfaces working in transmission mode. However, the polarization conversion efficiency was below 80%, and the overall thickness was relatively high, around $\lambda/10$. In [89], a plasmonic metasurface HWP operating in the sub-THz range was introduced, achieving a broadband operation with an efficiency above 80%. These transmission efficiency levels can be improved using multi-layer designs, such as the one studied in [85] where an efficiency near 90% around 10 GHz has been demonstrated.

2.1.3 Motivation and self-complementary structures

A simple idea to design a bi-layered HWP device capable to improve the transmission efficiency is to stack two QWP devices with a high efficiency. An excellent candidate for this is the self-complementary zigzag (ZZ) QWP transmissive metasurface, reported in [90]. This design exhibits a very high conversion efficiency, around 90%, as well as other interesting characteristics such as high stability at oblique incidence and an experimental 3-dB-axial-ratio (AR) fractional bandwidth (BW) of 53%. The structure is designed to operate at microwaves but it can be scaled to other frequency regimes. Thereby, this work was taken as a starting point with the aim to widen the technological reach of the zigzag geometry towards another band of technological interest nowadays (THz) and where the manufacturing and experimental characterization is more challenging. The operation principle of the reported QWP is based on self-complementary surfaces. The main rationale behind the operation of self-complementary structures and their application in polarizing devices is summarized below. It is emphasized that the content of this section has been extracted from [90] and [91] and is not an original contribution of the author of this thesis.

A typical example of a self-complementary structure [90] is depicted in Fig. 2.2(a): it is possible to interchange the black shapes with the grey shapes and its complementary structure is identical with that of the original structure. Self-complementary metasurfaces have gained significant attention due to their unique frequency-independent transmission and reflection properties and the possibility of the polarization transformation of plane waves. These properties are a consequence of Babinet's principle (valid for complementary structures using lossless conductors and dielectrics) and are excellent for obtaining a linear to circular polarization conversion. The operation of this kind of structures is graphically explained in Fig. 2.2(b).

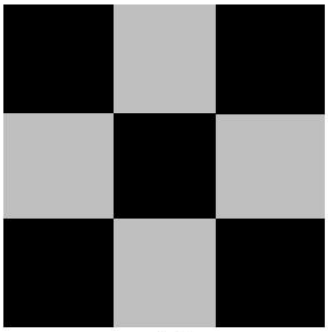

(a)

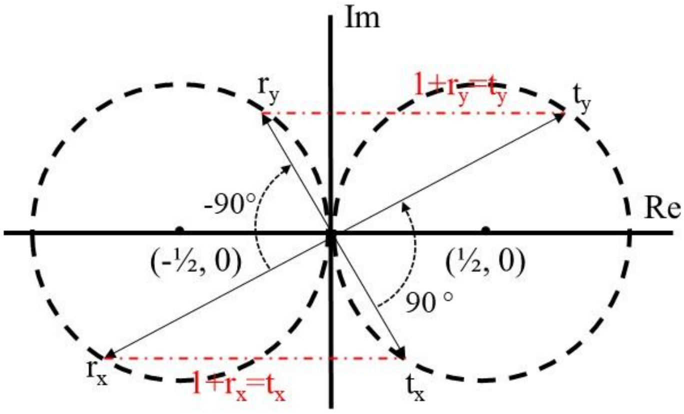

(b)

Fig. 2.2. (a) Self-complementary structure example. (b)Theoretical diagram of the reflection and transmission coefficients, in the complex plane, for polarized waves in x and y-axis.

Consider a screen illuminated by a normally incident plane wave with *x* and *y* field components where wave propagation is from medium 1 to medium 2 and r_x, r_y and t_x, t_y are the metasurface reflection and transmission coefficients in *x* and *y*-axis. Analyzing the operation in terms of S-parameters, we have the following general equality:

$$1 + S_{11} = S_{21}, \tag{2.5}$$

or equivalently

$$1 + r_x = t_x, \;\; 1 + r_y = t_y \tag{2.6}$$

Furthermore, from the law of energy conservation, it is obtained that:

$$|r_x|^2 + |t_x|^2 = 1, \; |r_y|^2 + |t_y|^2 = 1 \tag{2.7}$$

which means that in the absence of loss, the sum of the reflected and transmitted power is equal to unity. Combining 2.6 and 2.7,

$$\left|r_x + \tfrac{1}{2}\right| = \left|r_y + \tfrac{1}{2}\right| = \left|t_x - \tfrac{1}{2}\right| = \left|t_y - \tfrac{1}{2}\right| = \tfrac{1}{2} \tag{2.8}$$

Thereby, the reflection and transmission coefficients take values in the trajectory of a circumference in the complex plane, with radius equal to ½ and centered in the point (-½,0) for reflection and (½, 0) for transmission. From the Babinet's principle [92], it is obtained that:

$$r_x = -t_y^c,\ r_y = -t_x^c, r_x^c = -t_y,\ r_y^c = -t_x, \qquad \textbf{(2.9)}$$

where the superscript *c* stands for the complementary structure.

Due to the self-complementarity, $t_i^c = t_i$ and $r_i^c = r_i$, with $i = x$ or y. And consequently, substituting in 2.6:

$$t_x + t_y = 1\ ,\ r_x + r_y = -1 \qquad \textbf{(2.10)}$$

From 2.8 and 2.10 it can be demonstrated that the scalar product of transmission (reflection) coefficients in the complex plane is 0 and additionally,

$$\arg(t_y) - \arg(t_x) = -(\arg(r_y) - \arg(r_x)) = \pm 90° \qquad \textbf{(2.11)}$$

Thereby, the movement of t_x and t_y (r_x and r_y) in the circumference of Fig. 2.2(b) is guaranteed to preserve $\pm 90°$ angle between them independently of the frequency.

For a QWP device, in addition to a phase difference of $\pm 90°$, it is necessary to ensure equal amplitude between orthogonal linear polarization components of the transmission (reflection) coefficients to obtain circular polarization at the output. In [90], the equality of amplitudes was achieved by implementing a ZZ geometry and tuning its angle.

These interesting properties of self-complementarity and the excellent results derived from them made this structure the ideal candidate to achieve an equivalent bi-layered HWP in the THz range (with the corresponding scaling factor) by the stacking of two ZZ QWP separated by a dielectric spacer. Thus, an initial proof of concept with two ZZ plates varying the spacer thickness served as a starting point for the present work. However, as it was expected, the addition of a second layer and a spacer falls out of Babinet's theorem conditions [92] and breaking self-complementariness. Thereby, the design was redesigned deviating slightly from self-complementary metasurfaces to get HWP operation.

2.2 Design and simulation of the HWP

The initial design stage consisted in a tuning of the structure parameters to achieve the HWP desired behavior, leaving behind the pure self-complementarity constraints. Furthermore, different designs were done to be test the performance against possible misalignments resulting from the fabrication process. Thus, three different ZZ metasurface HWPs were designed and manufactured, the nominal one, with both layers aligned and two more, one with layers shifted along the *x*-axis and another shifted along the *y*-axis (see the unit cells in Fig. 2.3).

All the devices have the same parameters (shown in Table I as *Ideal*) and consist of a bi-layered ZZ pattern made of copper strips layers (passivized with aluminum) of thickness t_a = 0.55 μm separated by a thin flexible polypropylene (PP) film with permittivity 2.25 and thickness t_s = 0.1 mm. PP was intentionally chosen as the substrate material due to its low dielectric losses (tan δ= 1×10^{-3}) and low dispersion in the THz band [93]. In all the calculations performed with the commercial simulator CST Studio Suite®, the aluminum conductivity was taken as 2.7×10^7 S/m, smaller than the DC nominal value to account for the extra loss introduced by roughness.

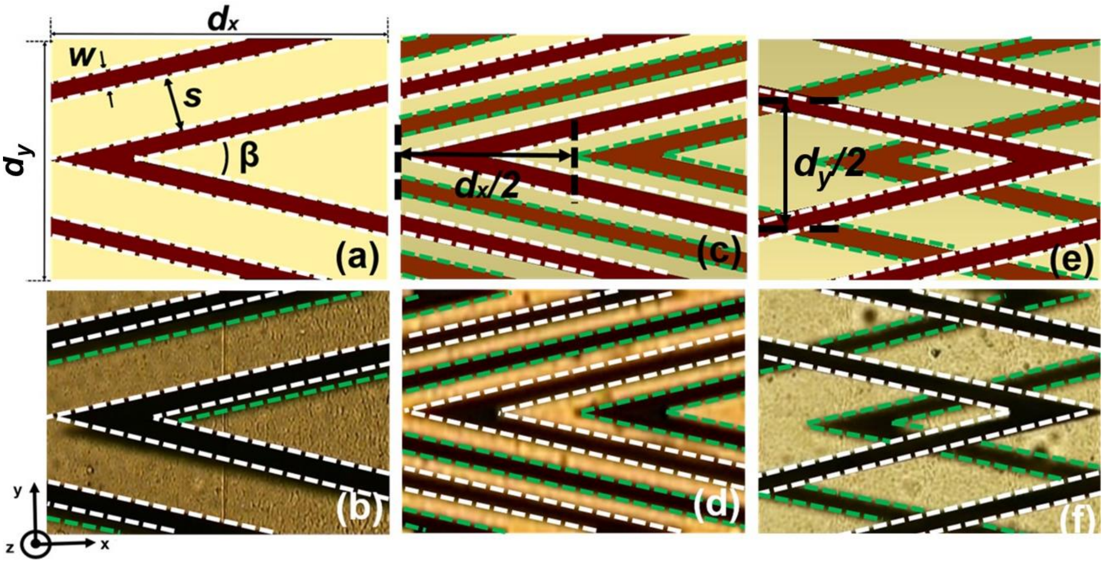

Fig. 2.3. Schematic (top) and microphotograph (bottom) of the ZZ-HWP unit cells corresponding to: (a) and (b) no-shifted, (c) and (d) x-shifted, and (e) and (f) y-shifted structure. The shifted structures have maximum shift increments between layers for x- and y-axis, Δx = dx/2 and Δy = dy/2, respectively. The green and white dashed lines have been included to help visualize opposite metallic layers (dark strips). The photographs of the fabricated devices were taken with a Mitutoyo Hyper MF U176-402-43 microscope with 20 × zoom and using the bottom light illumination to observe both faces simultaneously.

TABLE I. IDEAL AND MANUFACTURED PARAMETERS

Param.	*Ideal*	*no-shift*	*x-shift*	*y-shift*
w (μ)	*20*	*31*	*19*	*21*
β (º)	*25.0*	*24.5*	*25.8*	*25.1*
s (μm)	*60*	*61*	*61*	*60*

In the first design, hereinafter referred to as *no-shift* in the following, the ZZ patterns in both faces are parallel. Therefore, they are apparently overlapped in the schematic representation of Fig. 2.3(a). A fine-tuning of the design was mandatory to get a proper HWP operation around 150 GHz with the widest possible frequency BW. This tuning was performed using the frequency domain solver of CST. A fine tetrahedral mesh with 134000 cells was used with a minimum and maximum edge mesh cell lengths of 0.48 μm (2.48×10$^{-5}\lambda_0$) and 286 μm (0.14λ_0), respectively. Unit cell periodic boundary conditions were defined in both *x*- and *y*- axes and open space in *z*. The excitation was done with two Floquet ports using circular polarization modes. After this fine-tuning, the final parameters of the ZZ were obtained.

As it was introduced in section **2.1.1**, an ideal HWP completely switches the polarization state of a circularly polarized wave at the input to the orthogonal polarization with maximum power transfer at the output. As shown in Fig. 2.4, having parallel ZZs is the best configuration for optimal HWP performance out of the three devices explored. In the simulation results of Fig. 2.4(a), a maximum magnitude of the cross-polar transmission coefficient (T_{XP}) around –0.7 dB is obtained, whereas the magnitude of the co-polar transmission coefficient (T_{CP}) falls below –30 dB, meaning an excellent polarization conversion at the design frequency. The performance is evaluated more accurately by the cross-polar discrimination (XPD), defined as the ratio between the cross- and co-polar transmission coefficient magnitudes:

$$XPD = 20\log\left|\frac{T_{XP}}{T_{CP}}\right| = 20\ \log\left|\frac{T_{LR(RL)}}{T_{RR(LL)}}\right|, \qquad \textbf{(2.12)}$$

where the subscripts *R* and *L* refer to right-handed and left-handed circular polarization, respectively. From the definition (2.12), it is clear that the design criterion for an HWP is to maximize the parameter XPD as much as possible. In the simulation curve of Fig. 2.4(b), a peak value near 30 dB is obtained at the design frequency with a fractional BW of 8%, where the BW is defined as the frequency span where the XPD is above 10 dB.

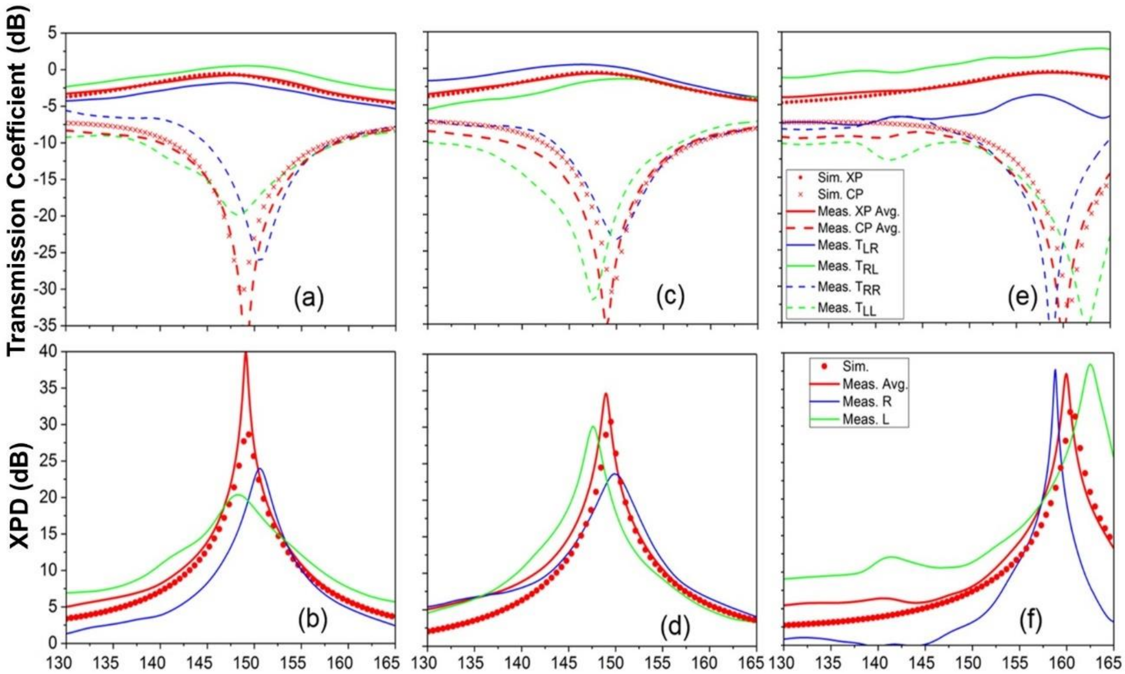

Fig. 2.4. Transmission coefficient magnitude for the (a) no-shift, (c) x-shift and (e) y-shift cases. XPD for the (b) no-shift, (d) x-shift and (f) y-shift cases. In the legend, "Sim." stands for simulation, "Meas." for

measurement, “XP” for cross-polar, “CP” for co-polar, “Avg.” for average, “T” for transmission coefficient, and the subscripts “R” and “L” for right-handed and left-handed circular polarization.

2.3 Fabrication and Measurement Method

To experimentally corroborate the ZZ-HWP performance, three prototypes with non-shifted and shifted metasurface layers were fabricated [see Fig. 2.3(b,d,f)]. Before micropatterning, the PP film was metalized on both sides via thermal deposition of aluminum in vacuum. The ZZ-pattern was created afterward using a contact photolithography technique, as described in [93]. The measurements were performed with the setup depicted schematically in Fig. 2.5. It consists of an ABmm™ millimeter-wave vector network analyzer (VNA) operating in the D-band of the millimeter-wave spectrum that extends from 110 to 170 GHz and is equipped with a quasioptical bench [see Appendix C.2]. For the characterization, a vertically polarized Gaussian beam with high purity is emitted into free space by a corrugated horn antenna (TX), and a pair of elliptical mirrors collimates the beam at the sample location. The transmitted beam is then redirected by another pair of mirrors towards the receiving antenna (RX), a corrugated horn.

As the performance must be evaluated in a circular basis and the antennas are linearly polarized, four independent measurements are needed, followed by an analytical conversion from linear to circular polarization. The measurement procedure consists of first calibrating the system by recording the free-space transmission with both the TX and RX antennas vertically polarized. Then, the HWP is inserted in two different configurations (0º and 90º), shown as an inset in Fig. 2.5. Two measurements are taken at each configuration by rotating the RX antenna at 0º and 90º to record the vertical and horizontal components, respectively. With this, four linear transmission coefficients (T_{uu}, T_{uv}, T_{vu}, T_{vv}) in a complex domain are obtained, covering all linear co- and cross-polar scenarios, as represented in the insets.

The transmission matrix in a circular basis can be straightforwardly obtained from the linear coefficients by simply applying a basis transformation [see Appendix B]:

$$\boldsymbol{C} = \begin{pmatrix} T_{RR} & T_{RL} \\ T_{LR} & T_{LL} \end{pmatrix} = \frac{1}{2}\begin{pmatrix} T_{uu} + T_{vv} + j(T_{uv} - T_{vu}) & T_{uu} - T_{vv} - j(T_{uv} + T_{vu}) \\ T_{uu} - T_{vv} + j(T_{uv} + T_{vu}) & T_{uu} + T_{vv} - j(T_{uv} - T_{vu}) \end{pmatrix} \quad \textbf{(2.13)}$$

An ideal HWP should have:

$$\boldsymbol{C} = \begin{pmatrix} 0 & 1 \\ 1 & 0 \end{pmatrix} \quad \textbf{(2.14)}$$

That corresponds to:

$$T_{uu} = -T_{vv} \quad \textbf{(2.15)}$$

$$T_{uv} = T_{vu} = 0 \quad \textbf{(2.16)}$$

However, in practice, these conditions are fulfilled only approximately. The matrix C relates the fields amplitude at the input and output in a circular polarization basis:

$$\begin{pmatrix} E_R^o \\ E_L^o \end{pmatrix} = \boldsymbol{C} \begin{pmatrix} E_R^i \\ E_L^i \end{pmatrix} \quad \textbf{(2.17)}$$

where E is the electric field and the superscript i and o stand for input and output, respectively. The results from Fig. 2.4 assume right-handed and left-handed circularly-polarized waves at the input to get a complete characterization. This means that both T_{RR} and T_{LL}, obtained in the complex domain, are considered for the co-polar transmission coefficient. Then their average is calculated, expressing the resulting magnitude in dB and denoted as *CP Avg.* in the plots. Likewise, T_{RL} and T_{LR} (also in the complex domain) are considered for the cross-polar transmission coefficient. Again, an average value is calculated, expressing the resulting magnitude in dB and denoted as *XP Avg.* in the plots. As a side comment, note that calculating an average is essential because, as it will be seen, some curves reach values slightly above 0 dB after the conversion from linear to circular (obviously, unphysical and caused by measurement errors).

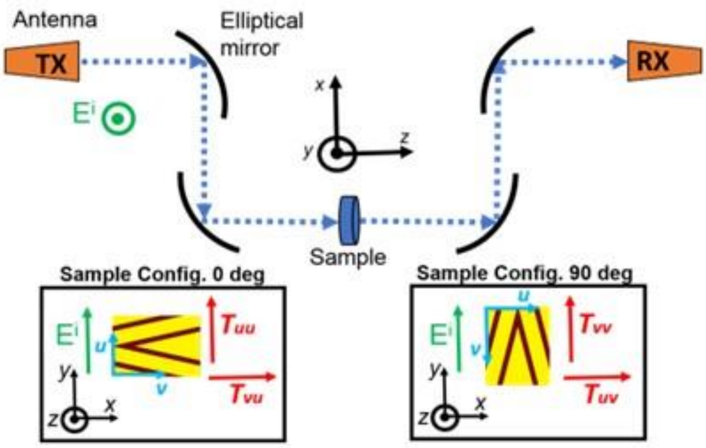

Fig. 2.5. Schematic of the experimental setup. The insets show two ZZ-HWP configurations. For both configurations, the linear transmission coefficients are obtained with both TX and RX antennas parallel to *y* and with the TX antenna parallel to y and the RX antenna parallel to *x*.

Moreover, an apparent discrepancy in T_{RL} and T_{LR} transmission coefficients occurs, being more remarkable in the *y*-shift case, where a difference of almost 5 dB is obtained. This can be attributed to experimental errors such as system position misalignments (the rotation of the RX antenna and the sample were done manually) and noise. Also, as T_{RL} and T_{LR} are calculated from T_{uu}, T_{uv}, T_{vu} and T_{uv}, (complex coefficients), small phase errors in these linear coefficients due to thermal deviations in the VNA can have a significant impact on the results. Typically, the measurements are fast, to avoid these thermal drifts. However, two different measurements are performed for a fixed sample position, co- and cross-polar, by rotating the RX antenna. The calibration is done with antennas in a co-polar position. The rotation of the RX antenna for the cross-polar characterization requires some manipulation time, which might be critical as it can introduce some unavoidable thermal deviation of the VNA in this susceptible measurement. Furthermore, the quasioptical bench plate can have a different effect on vertical and horizontal polarization, usually negligible thanks to the focusing mirrors that guide the Gaussian beam. However, the sample might expand the beam so that it effectively "sees" the ground plane below, leading to a different response under vertical or horizontal polarization. These factors can add accumulatively, leading to a discrepancy between T_{RL} and T_{LR}. Nevertheless, a systematic series of measurements were performed until it was found that the results were consistent with simulations calculating when the average was calculated. As a double-check, the cross-polar transmission isolation (in linear polarization, i.e., with TX and RX antennas in orthogonal positions) was measured in the absence of DUT. It was found to be reasonably low (below –25 dB).

2.4 Experimental Results

Following the method described, the rest of the curves shown in Fig. 2.4(a) were obtained. Both cross-polar components T_{LR} (solid blue) and T_{RL} (solid green) reach a peak at the operation frequency, and their average value XP (solid red) shows outstanding agreement with the simulation. Regarding the co-polar components, T_{RR} (dashed blue) and T_{LL} (dashed green) both exhibit a clear dip around the operation frequency, and the average value CP (dashed red) almost coincides with the simulated curve. This excellent performance is corroborated in the XPD results of Fig. 2.4(b). Again, two cases are considered assuming right-handed (blue) or left-handed (green) polarization at the input. The XPD is calculated as appears in the rightmost term of **(2.12)** in either case.

A pronounced peak near the operation frequency is obtained in both left and right-handed circular polarization cases, in good agreement with the simulation curve, with a maximum value almost reaching 40 dB. This value, higher than the theoretical one, is obtained using *XP* and *CP* average magnitude values (drawn in red solid and dashed lines, respectively, in the leftmost graphs of Fig. 2.4). However, note that the value in each measurement is lower, around 30 dB, so it could be a fortunate effect of the selected averaging method. Therefore, an XPD of approximately 30 dB was taken as a realistic performance. Thus, from the previous analysis, it can be affirmed that the *no-shift* design has an excellent behavior, with very low experimental insertion loss (< 1 dB), meaning a circular polarization conversion efficiency of around 90%, high *XPD* (~ 30 dB), and relatively wide fractional BW (~ 8.3%). The main performance parameters are summarized in Table II to offer a more detailed view.

TABLE II. ZZ-HWP PARAMETERS FOR MEAS. AVG.

Model	*XPD_{max} (dB)*¤	*f_{XPD} (GHz)*¤¤	*Tx (dB)**	*BW (%)***
No-Shift Sim.	28.87	149.25	-0.742	8.09
No-Shift Meas.	39.14	149.11	-0.785	8.98
x-Shift sim	31.11	149.35	-0.709	8.27
x-Shift Meas.	34.75	149.08	-0.668	9.20
y-Shift Sim.	34.30	159.02	-0.650	9.16
y-Shift Meas.	37.03	159.04	-0.751	9.72

¤ XPD_{max} maximum XPD value.
¤¤ f_{XPD} frequency at XPD maximum.
* *Tx* corresponds to the transmission amplitude value at the frequency where *XPD* is maximum.
** *BW* is the frequency bandwidth considering *XPD* values higher than 10 dB.

2.5 Robustness analysis with misaligned devices

Even though the previous results are encouraging, it is known that the manufacturing process can introduce some inevitable deviations. The alignment between layers is especially relevant, as the microphotograph of Fig. 2.3(b) reveals. As demonstrated in the previous section, those slight imperfections were not essential and did not deteriorate the ZZ-HWP behavior from the simulation results. Nevertheless, as a proper layer alignment might be time-consuming in a massive production, the device's robustness against misalignments is evaluated in the following. Two additional designs were tested, considering the worst case of maximal shifting along *x*- and *y*-directions, shown in Fig. 2.3(c), (d) and Fig. 2.3(e), (f), and hereinafter called *x-shift* and *y-shift*, respectively.

Concentrating first on the *x-shift* design, one can notice the robustness of the ZZ-HWP with respect to misalignment errors in this dimension: both the simulation and experimental results are nearly coincident with those of the *no-shift* prototype studied above. The average measurements almost overlap with the simulation curves, as shown in Fig. 2.4(c). Similarly, the average *XPD* value reaches a high peak at the operating frequency with a maximum value of approximately 30 dB, low insertion loss (< 1 dB), and a fractional bandwidth near 8%. In contrast, when the misalignment is applied in the *y*-direction, the response of the ZZ-HWP is severely affected, see Fig. 2.4(e). The main spectral change observed is a frequency upshift of the optimal polarization conversion that now takes place near 160 GHz, i.e., a deviation of 6.4% with respect to the design frequency. Nevertheless, the device still works well as HWP, with experimental insertion losses below 1 dB, a maximum *XPD* larger than 35 dB, and a fractional bandwidth of 14%. The most representative values for every model are displayed in Table II-II. A comparison of the present structure with other recent works of HWP based on metasurfaces is presented in Table III. As observed there, devices working in reflection mode achieve a significant broader BW than those operating in transmission mode. Some transmission devices have obtained high enough levels of BW as the case of [89], with 10.7% (being the highest level in TX in the table), with a simultaneous excellent *XPD* value (26.74 dB). However, this device implies a thickness near λ/4, less compact that the present work. In the present work the ZZ-HWP reaches an outstanding level of *XPD* value (39.14 dB) and a broad operation BW near 9%, demonstrating a remarkable result for a device operating in transmission. In addition, the structure is extremely compact (ultrathin), around λ/20.

TABLE III. COMPARISON WITH OTHER HWP DEVICES

REF	*Mode*	*Layers*	XPD_{max} (dB)	f_{XPD}¤ (THz)	*BW** (%)	*Thickness (λ)*
[43]	RX	2	~20	2	32	~1/12
[44]	RX	2	~25	95	42	~1/5
[40]	TX	3	13.97	0.6	2	~1/5
[45]	TX	2	18.06	0.5	0.6	~1/14
[89]	TX	1	26.74	0.14	10.7	~1/4
[85]	TX	2	13.06	0.0101	4.9	~1/20
[86]	TX	3	25.2	0.0105	7.6	~1/8
Present Work	TX	2	39.14	0.149	8.98	~1/20

¤ XPD_{max} maximum XPD value.
¤¤ f_{XPD} frequency at XPD maximum.
* *BW* is the frequency bandwidth considering *XPD* values higher than 10 dB.

A detailed analysis to explain the robustness with respect to a shift in the *x*-direction and the sensitivity to a change along *y* is performed. The numerical analysis considers two-parametric sweeps: varying Δx and Δy from zero (fully aligned) to the maximum misalignment value, $d_x/2$ or $d_y/2$, respectively, assuming circular polarization.

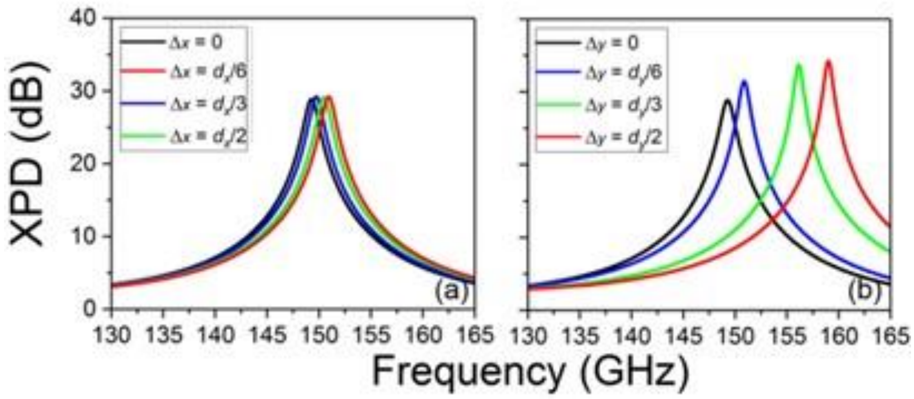

Fig. 2.6. Simulated XPD for several misalignments: (a) Δx and (b) Δy.

From the results presented in Fig. 2.6, it is observed that the HWP operation frequency increases in both cases, but the effect is considerably more substantial for Δy. As observed in the figure, the response is insensitive to Δx and presents some negligible dependence on Δy, with a variation in magnitude of less than 0.2 dB and in phase of less than 5º at the operation frequency. Thus, under vertically polarized excitation (***E*** parallel to *y*), the device is mainly transparent with a transmission coefficient magnitude close to 0 dB in the entire frequency span and a phase near 0º at the operation frequency, see Fig. 2.7.

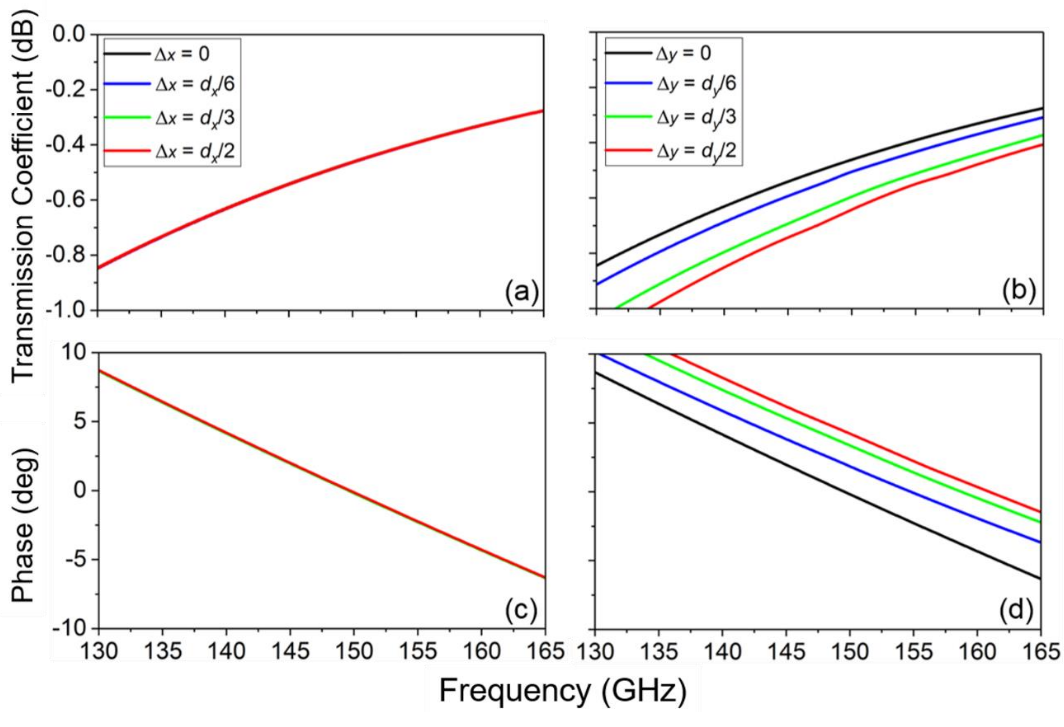

Fig. 2.7. Simulated vertical polarization transmission coefficient for various (a), (c) Δx and (b), (d) Δy cases. Top and bottom panels show magnitude and phase, respectively.

In contrast, the response with horizontal polarization (***E*** parallel to x) is almost insensitive to Δx but demonstrates a marked variation with Δy, as can be inferred from the simulated transmission coefficient in Fig. 2.8. In all cases, there is a peak in the magnitude that happens near but not precisely at the point where the phase is 180 deg and whose location depends strongly on Δy. Overall, from this initial analysis, it is clear that the horizontal polarization component is the main responsible for the performance of the misaligned ZZ-HWP. Thus, hereafter we fix the attention to this case.

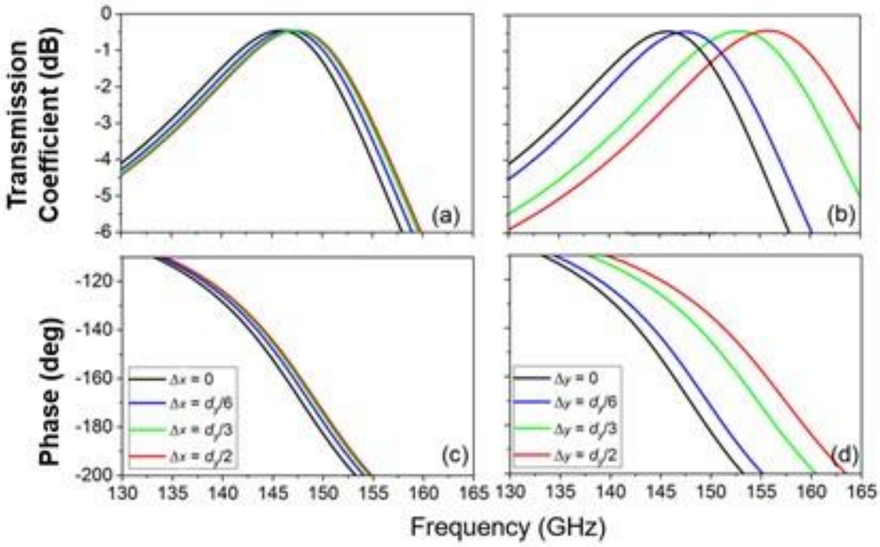

Fig. 2.8. Simulated horizontal polarization transmission coefficient for various (a), (c) Δx and (b), (d) Δy cases. Top and bottom panels show magnitude and phase, respectively.

From the cross-sectional magnetic field distribution in Fig. 2.9, the magnetic coupling can be discarded in either case. In contrast, Fig. 2.10(a) and (b) show a strong electric coupling between layers. As observed in Fig. 2.10(c), when Δx is varied, the electric field lines are nearly identical to the no-shift case, suggesting that this modification still allows an electric coupling between layers similar to the ideal case. Consequently, the operation frequency remains almost unmodified, probably due to a similar value of the capacitance between layers. However, when the misalignment is applied along y, the electric coupling is strongly affected, and the electric field in the dielectric spacer differs substantially from the initial *no-shift* case. From the plots in Fig. 2.10(d), it can be concluded that the electric coupling and hence the capacitance between layers diminishes, explaining the upshift of the operation frequency.

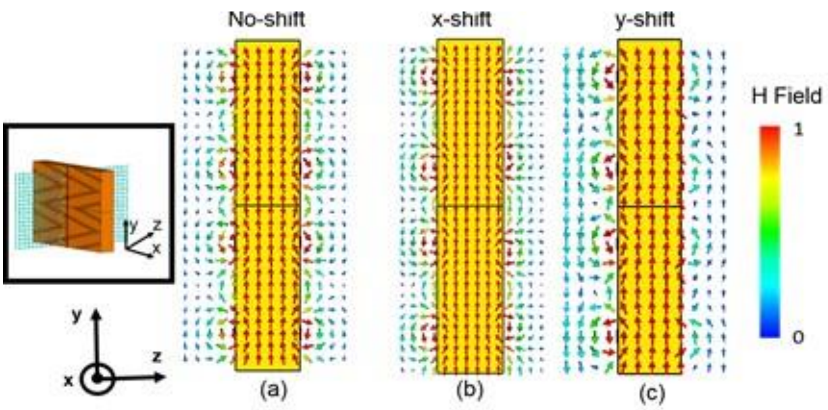

Fig. 2.9. Cross-sectional view (*y-z* plane as shown in the leftmost inset) of the instantaneous magnetic field (represented as arrows) for (a) no-shift, (b) *x*-shift and (c) *y*-shift designs at the respective operation frequency.

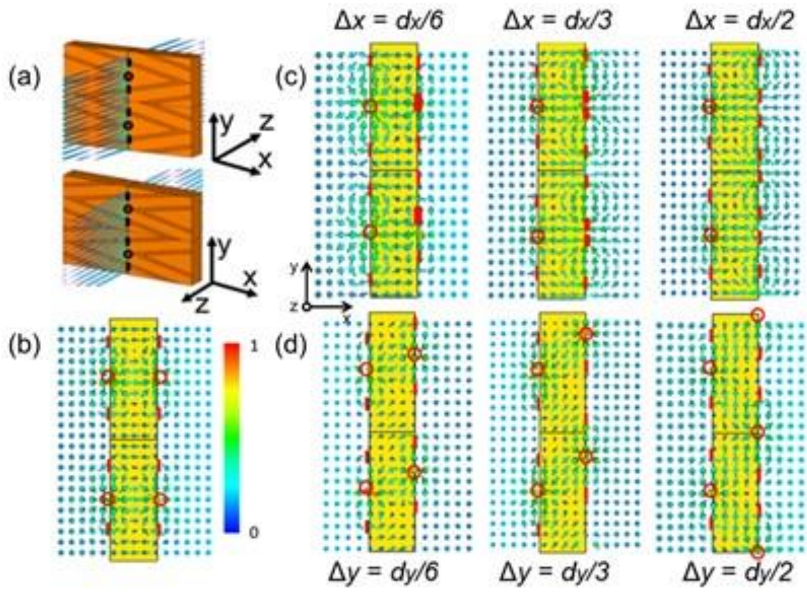

Fig. 2.10. (a) Front (top) and back (bottom) views show the cross-section (no-shift case) where the electric field is evaluated. The cross-sectional view (y-z plane) of the instantaneous electric field (represented as arrows) at the maximum XPD frequency for (b) no-shift, (c) different Δx and (d) different Δy cases. ZZ vertices and the strip cross-sections have been highlighted with red circles and straight segments to aid with the interpretation, following the scheme shown in (a).

2.6 Summary

In this chapter, the performance of the ultrathin transmissive HWP based on a bi-layered ZZ metasurface designed for operation at 150 GHz have been analyzed in detail. Having the thickness of λ/20, the fabricated device revealed excellent agreement with the numerical simulations, reaching a maximum transmission coefficient magnitude of −0.78 dB (i.e., the polarization conversion efficiency is over 90%), and an XPD ∼30 dB, with a fractional BW near 9%. The robustness of the device with respect to possible misalignments between layers introduced in the manufacturing process has been analyzed in detail. From the analysis performed, it has been extracted the extremely robust response with regards to a shift along the x-direction (i.e., perpendicularly to the guiding lines of zigzags), whereas it varies more considerably with a shift along the y-direction (i.e., along the guiding lines of zigzags). Even in the worst case, the performance of the device as a HWP still remains excellent although shifted in frequency. A subsequent study has clarified that the response is very stable for any misalignment under linear vertical polarization excitation, but it is very dependent on misalignments along y under linear horizontally polarized excitation. We have ascertained that this is due to the strong electrical coupling between layers, whose field distribution has a strong dependence on a shift along *y*.

Chapter 3. Half Wave Plate Metalens based on Pancharatnam Berry Metasurfaces

Metalenses are devices based on metasurfaces and designed to focus the wavefront in a single or several spots. Sometimes, these devices are combined with antennas leading to low profile systems. These systems are able to improve the antenna directivity or even change the wave polarization, depending on the metalens properties.

The first part of this chapter is dedicated to presenting a HWP Pancharatnam Berry Metalens (PBM) working in transmission mode achieving a transmission efficiency level of 90.15% and a thickness below λ/13. The second part of the chapter introduces a Pancharatnam Berry Antenna Metalens (PBAM) system based on this structure. The system operates at 87 GHz and achieves a low AR of 0.5 dB, demonstrating circular polarization with high purity and reaching an excellent aperture efficiency of 46% at the operation frequency. An AR below 2 dB is achieved between 82 to 95 GHz with aperture efficiency levels around 30% and directivities close to 32 dB over the whole band. Moreover, it is demonstrated that by shifting the feeder antenna, a good operation can be achieved between 75 and 105 GHz, with directivities around 32 dB, AR below 3 dB, and aperture efficiency levels around 35% and 25% for the lower and higher frequency bands, respectively. A prototype of the metasurface has been fabricated, and both the metalens and PBAM system have been measured experimentally.

3.1 Background on HWP metalenses

In 1873, Ernst Abbe reported that conventional lenses were incapable of capturing some fine details of any given image, being the first scientist to define the term numerical aperture (*NA*) [94] and being credited by many for discovering the resolution limit of the microscope, with the formula (published in 1873)[95]:

$$d = \frac{\lambda}{2\,NA} \qquad \textbf{(3.1)}$$

where *d* is the smallest resolvable distance between two point-source objects so that they can be independently distinguished, λ is the free-space wavelength and $NA = n \sin \theta$, with *n* the index of refraction of the medium being imaged and θ the half-angle subtended by the optical objective lens. Closely related to this concept is the Rayleigh diffraction limit [96], which modifies the calculation of the resolution limit as a result of the difference in how they defined what it means for two distinct sources to be resolved from each other. Thus, whereas in Abbe limit, the sum of the two point-source profiles presents a small dip discernible between the two maxima, in the Rayleigh limit this dip is clearly distinct, see Fig. 3.1.

$$d = \frac{0.61\,\lambda}{NA} \quad \textbf{(3.2)}$$

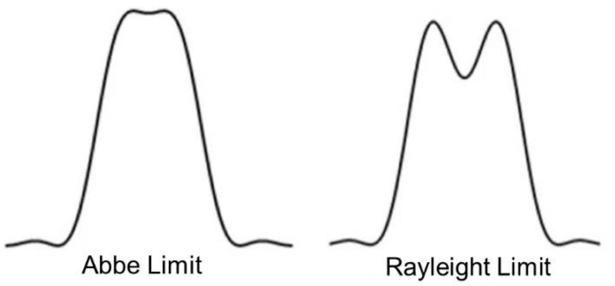

Fig. 3.1. Result of the sum of two point-source profiles according to the smallest resolvable distance for Abbe and Rayleigh.

Once thought impassable, these resolution limits were crossed for first time in 1972 [97] and lately with the emergence of the metalenses, devices based on metamaterials and used as unconventional alternatives to the classical lenses. Thus, in 2000, Pendry went beyond this diffraction limit proposing a negative refractive index metalens [98], coining the perfect lens concept. Since then, exciting lens designs related to this sort of metamaterials have been proposed [98]–[100].

Unlike conventional dielectrics, the permittivity and permeability of a metamaterial can be adjusted independently so metalenses can presumably be better matched to free space than dielectric lenses. Moreover, metalenses implemented with flat and thin structures such as the metasurfaces, do not show spherical aberration due to the lack of curved surfaces in the beam path. The attractiveness of these features has given rise to several planar metasurface-based lenses have been proposed during last decade [49], [101].

Despite the extraordinary performances of the metalenses, the operation principle remains the same as that of an ordinary dielectric lens, being required a specific phase profile provided by the metasurface in order to focus on a spot. Thereby, this phase profile is discretized in the surface according to the phase introduced by every constituent meta-atom. To synthesize this phase two main approaches are followed: the first one uses meta-atoms that are different from each other by modeling their shapes, which gives rise to numerous and elaborate unit cell profiles [52]–[54], [56]–[58], [102]. The second and completely different approach, applicable to the present work, achieves the wavefront control without modifying the unit cell's geometry, using the Pancharatnam-Berry (PB) principle [59], [60]. This principle states that by applying a rotation angle to a HWP device or unit cell excited with a circularly polarized wave, a phase equal to two times the rotation angle appears at the output for the transmitted crosspolar component. This entails a technical advantage in design and fabrication, becoming an appealing technique for the design of diffractive elements. Hence, by applying the PB principle to HWP GRIN metasurfaces [61], [62] it is possible to manipulate wavefronts using rotated identical meta-atoms [66]–[68]. These structures are known as PB metasurfaces (PBM) and the spatial phase profile is engineered by the meta-atoms' rotation angle following the PB principle. This approach presents a remarkable advantage against the first one, achieving full phase coverage (0 to 360 deg) in every meta-atom with a unique unit cell design. In this work a PBM is designed to work as a metalens operating in transmission mode.

In general terms, to qualify the performances of these PBM transmission structures (independently of the device functionality), one of the most significant criterions used is the transmission efficiency, defined as the maximum level of crosspolar component amplitude at the output of the metasurface. Usually, to increase this value, multilayer architectures are required. This is due to the higher number of freedom degrees that stacked structures offer to control phase, amplitude and polarization of the wavefronts providing at the same time impedance matching. Likewise, some PBMs for wavefront controlling operating in transmission mode have demonstrated efficiencies about 60% [103] or even near 100% by using multilayer designs (four cascaded metasurfaces) [104]. However, these devices result in bulky structures (~4λ/3) which require intermediate substrate layers that entail strict alignment constraints and, more importantly, tight contact between them to avoid thin air layers that can ruin the performance.

In respect of PBM metalenses, recent examples of ultrathin tri-layer devices have achieved nearly 68% of transmission efficiency (with a thickness ~λ/6) [55], or even 90% of transmission efficiency (with a thickness ~λ/5) [40]. Despite having good efficiency and compactness, tri-layer devices still are more challenging than single- or bi-layer structures from a manufacturing viewpoint. Single-layer devices operating in transmission mode can only reach 25% of transmission efficiency [63], [105]. Therefore, bi-layer PBM structures are the preferred candidates for leveraging the fabrication constraints. Notwithstanding, it is challenging to design bi-layer devices with efficiency levels similar to tri-layer structures due to the reduced freedom to fine-tune the whole device's impedance matching. Experimental and numerical demonstrations include a recent PB metalens with a transmission efficiency of 82.7% (thickness below λ/8 [72]). Although this is a high-efficiency value, it remains below the best tri-layer designs [40].

To tackle the problem of the transmission efficiency, in the next section, we experimentally demonstrate an ultrathin bi-layer PB metalens which reaches a transmission efficiency of 90.15% with a thickness < λ/13. The numerical analysis and measurements confirmed the device's ability to convert a circularly polarized wave's handedness and focus the wavefront at 94 mm from the metasurface at 87 GHz.

3.2 PBM Metalens

3.2.1 H-shaped Bi-layer Unit Cell Study

With the aim of achieving a PBM structure, a HWP unit cell design is required to consolidate the meta-atoms that will compose the polarization and wavefront controller device. These meta-atoms have to be able of converting the circular polarization as was explained in the State of Art chapter in order to make use of the PB principle. Furthermore, the challenge of the design lies in the persecution of a bi-layer unit cell, being the minimum number of layers that would allow 100% of transmission efficiency, as was mentioned in the text above. Therefore, the initial unit cell layout was thought as a dielectric with two metallic layers in both faces.

As it was introduced in previous chapters, the behavior of the orthogonal components of an incident wave in a metamaterial is not determined by a dielectric constant solely, but because of the metasurface electromagnetic properties derived from the performance of the unit cell geometry, size, shape and the selected material properties. Thus, once the unit cell layout was chosen as two dielectric-sandwiched metallic layers and the initial unit cell geometry chosen as a square, the starting point for the metallic layers shape was selected as an H-shaped piece with identical arm lengths and thicknesses, as a result of a first intuition of how to disturb separately the currents for the two orthogonal components of the incident wave, before applying optimization by software. The unit cell electromagnetic behavior is explained in the following, as well as the final appearance of the device and material features.

Hence, the final PBM's unit cell consists of two aluminum layers of H-shaped elements with a thickness of 0.55 μm patterned on both faces of a thin polypropylene (PP) slab with a thickness of 254±5 μm and dielectric permittivity of 2.25, see Fig. 3.2(a) for a schematic with dimensions and Fig. 3.2(b) for a photograph of a unit cell. PP was intentionally chosen as the substrate material due to its low dielectric losses ($\tan\delta \approx 1\times10^{-3}$) [106]. Before micropatterning, the PP film was metalized from both sides via thermal deposition of aluminum in vacuum. Afterward, a contact photolithography technique [32] was applied to create the H-shaped patterns sequentially on the PP faces. Regarding the numerical characterization, all the simulations were performed using the commercial software CST Studio Suite®. The aluminum conductivity was taken as 2.7×10^{7} S/m, smaller than the DC nominal value, to account for extra losses introduced by surface roughness.

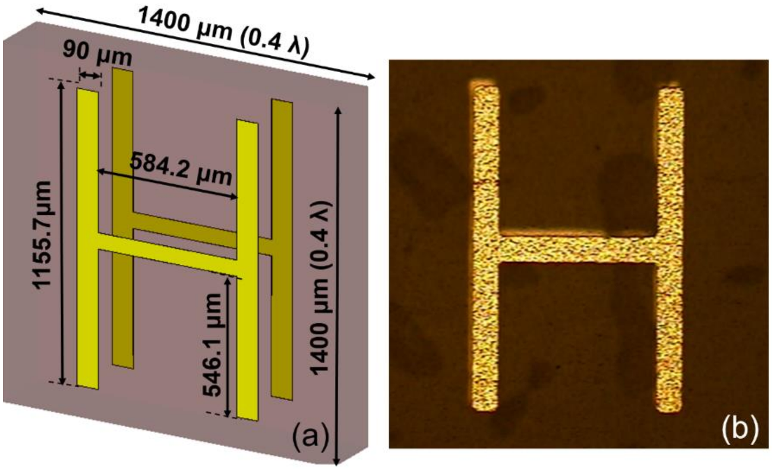

Fig. 3.2. (a) Schematic view of the H-shaped bi-layer unit cell with the main dimensions. The metallic areas are represented in yellow and the dielectric substrate in purple. (b) Microphotograph of a unit cell of the fabricated metalens taken with a Mitutoyo Hyper MF U176-402-43 microscope with 5 × zoom.

To understand the electromagnetic behavior of the unit cell, we performed a detailed unit-cell study under linear polarization excitation (*x*- and *y*- components) to visualize the working principle of the HWP metasurface. The resonant behavior of a single layer element (1-L), depicted in Fig. 3.3(a), was studied and numerically compared with the bi-layered element (2-L), Fig. 3.3(b). For this analysis, we used the frequency domain solver of CST Microwave Studio ® with Floquet periodic boundary conditions and a mesh of 17558 tetrahedrons, applying linear vertical (*y* electric field component) and horizontal (*x* electric field component) polarization excitation, named in the solver as TE mode and TM mode, respectively.

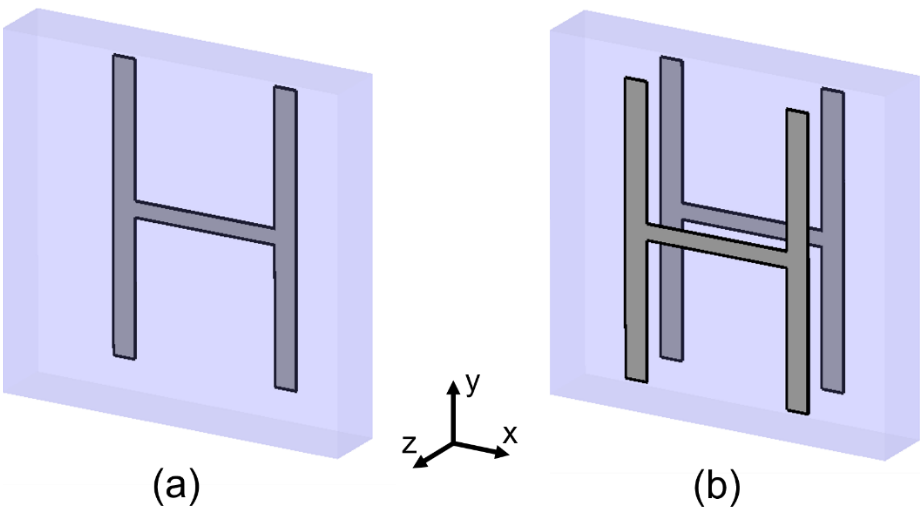

Fig. 3.3. 1-L (a) and 2-L (b) unit cell element. Dielectric substrate is shown in blue and metallization in gray.

The transmission coefficient magnitudes T_{xx} and T_{yy} for 1-L (dashed red and blue lines, respectively) and 2-L (solid red and blue lines, respectively), and the phase difference between them (solid black line for two layers) as a function of frequency are shown in Fig. 3.4(a). The single-layer element under horizontal excitation presents a dip at 58.4 GHz (dashed red curve) caused by the fundamental half-wavelength resonance of a capacitively-loaded dipole, see Fig. 3.4(b), where surface currents are plotted. Note that the vertical arms act as capacitive loading of the horizontal arm.

When two layers are stacked, a resonance hybridization occurs due to the magnetic coupling between layers [Fig. 3.4(d)] introducing two dips in the spectrum [Fig. 3.4(a), solid red curve]. Beyond the second dip, almost full transmission is achieved. The mechanism is similar under vertical polarization. In this case, for the single layer, the dip happens at 115.6 GHz (Fig. 3.4(a), dashed blue curve), caused again by the fundamental dipole resonance [Fig. 3.4(c)]. When two layers are stacked, this resonance undergoes hybridization due to electric coupling (Fig. 3.4(e)), and the lowest frequency dip takes place near 90 GHz, which is preceded by a peak of transmission. The resonance proximity generates a fast phase change, leading to a phase difference between vertical and horizontal polarization of 180° at 86.2 GHz. Such phase difference fulfills the conditions needed for a HWP since transmission is maximum for both components near that frequency.

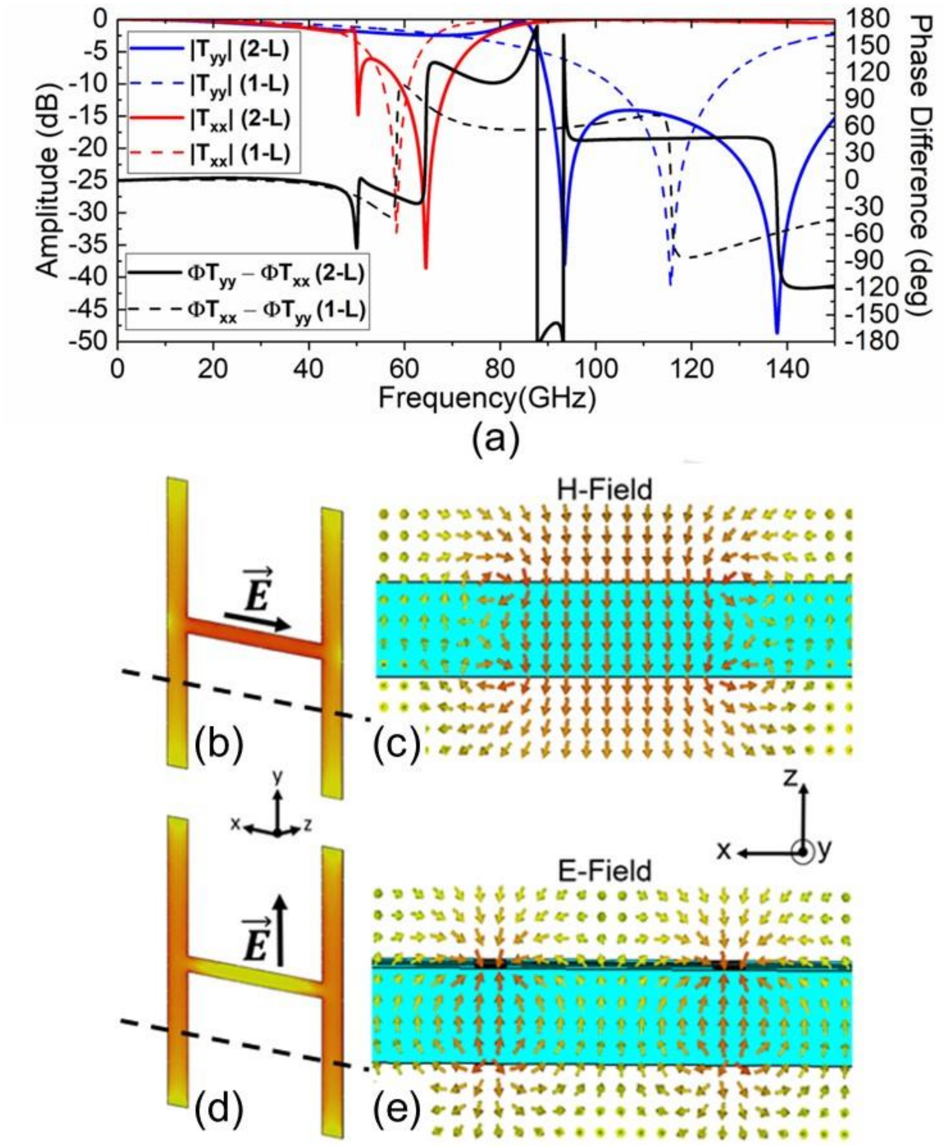

Fig. 3.4. (a) Transmission coefficient magnitude for 1-L (dashed) and 2-L (solid) calculated using linear vertical (blue) and horizontal (red) polarization excitation. Transmission coefficient phase difference between vertical and horizontal polarization for 1-L (black dashed line) and for 2-L (black solid line). (b), (c) Snapshot of the surface currents maximum magnitude for one layer at the dip for x- and y-polarized incident wave, at 58.4 GHz and 115.7 GHz, respectively. (d), (e) Snapshot of the magnetic/electric field lines between the bi-layer design at the cutting plane (black dashed lines) depicted in (b) and (c) at 87 GHz.

3.2.2 Circular Polarization Analysis

Next, the unit cell is analyzed under circular polarization excitation. A simulation in the frequency domain with Floquet conditions is carried out again with a mesh of 17875 tetrahedrons. The transmission and reflection coefficients under left-handed circularly polarized (LHCP) excitation are shown in the decibel scale in Fig. 3.5. From this figure, a cross-polar transmission coefficient (T_{RL}) of around –0.9 dB is obtained at 86.2 GHz, demonstrating a high transmission efficiency (90.15%) of right-handed circular polarization (RHCP). At the same frequency, the reflection coefficients (both R_{LL} and

R_{RL}) and the transmitted co-polar component (T_{LL}) are below –10 dB, indicating a good matching and a proper rejection of the non-desired polarization.

The figure of merit to evaluate the HWP performances is the Cross Polarization Discrimination (XPD), which relates the ratio between the converted and non-converted circular polarization at the output of the device,

$$XPD(dB) = 20\ log\left|\frac{T_{XP}}{T_{CP}}\right| = 20\ log\left|\frac{T_{RL}}{T_{LL}}\right| \tag{3.3}$$

This figure is related to the AR and defined as

$$XPD(dB) = 20\ log\left|\frac{AR-1}{AR+1}\right| \tag{3.4}$$

where the AR is defined in linear magnitude, and T_{XP} and T_{CP} represent the transmission coefficients for the cross-polar and co-polar components, respectively. Note that XPD usually presents the ratio between co-polar and cross-polarization. However, in this case, the desirable polarization component is the opposite of the incident wave. The transmission coefficients and the ratio related to the AR are inverted in the formulation.

The resulting XPD value is above 10 dB within a fractional bandwidth of 3.4%, showing the highest value at 87.7 GHz. An XPD above 10 dB implies an AR below 3dB, so we impose this value as the minimum one required for a proper level of conversion. The maximum T_{RL} and the minimum T_{LL} do not coincide in frequency. Consequently, the maximum XPD (87.7 GHz) and maximum T_{RL} (86.2 GHz) happen at different frequencies. As a trade-off, we fix the metalens operation frequency at 87 GHz, meaning an XPD value of 13.2 dB and T_{RL} of –1.1 dB.

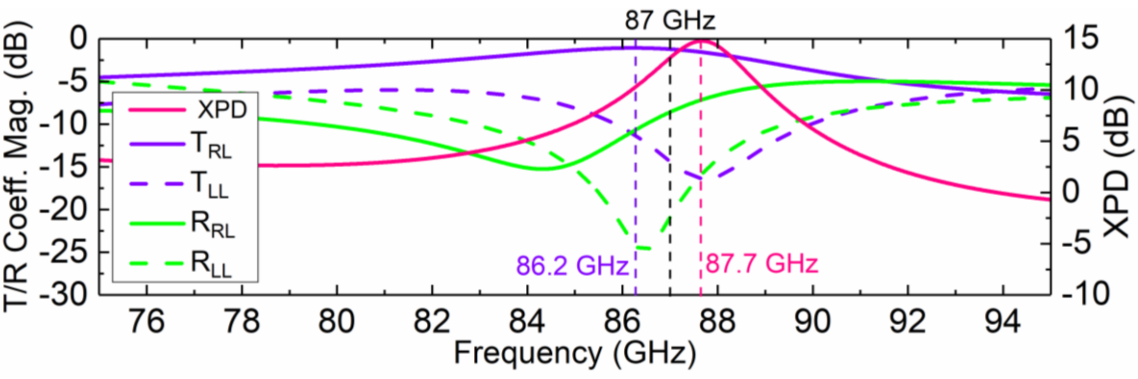

Fig. 3.5. Unit cell transmission (green) and reflection (purple) coefficients magnitude in dB when the structure is excited by a LHCP plane wave at normal incidence. Solid/dashed lines correspond to RHCP/LHCP polarization. Solid magenta line represents the XPD value at the output.

3.2.3 Metalens Phase Profile Design

The metalens is composed by 63×63 unit cells with a period of p=1.4 mm (0.4λ_0) and every unit cell is numerated in along both x and y axes from –31 to 31, being (0,0) the central point of the central unit cell, see Fig. 3.6(a). According to the PB phase principle, the rotation angles for every unit cell of the PB metalens correspond with half of the desired ideal phase shift at each surface position, φ(x,y). This phase shift as a function of the unit cell define a discretized metalens phase profile and it is extracted from the flat converging lens equation,

$$\varphi(x,y) = \frac{2\pi f_0}{c_0}\left(\sqrt{x^2+y^2+FL^2} - FL\right) \qquad \textbf{(3.5)}$$

where x and y are the unit cell central positions in the metasurface, FL is the previously fixed focal length at the design frequency, f_0 and c_0 is the speed of light in vacuum. A schematic of the focusing mechanism is depicted in Fig. 3.6(b).

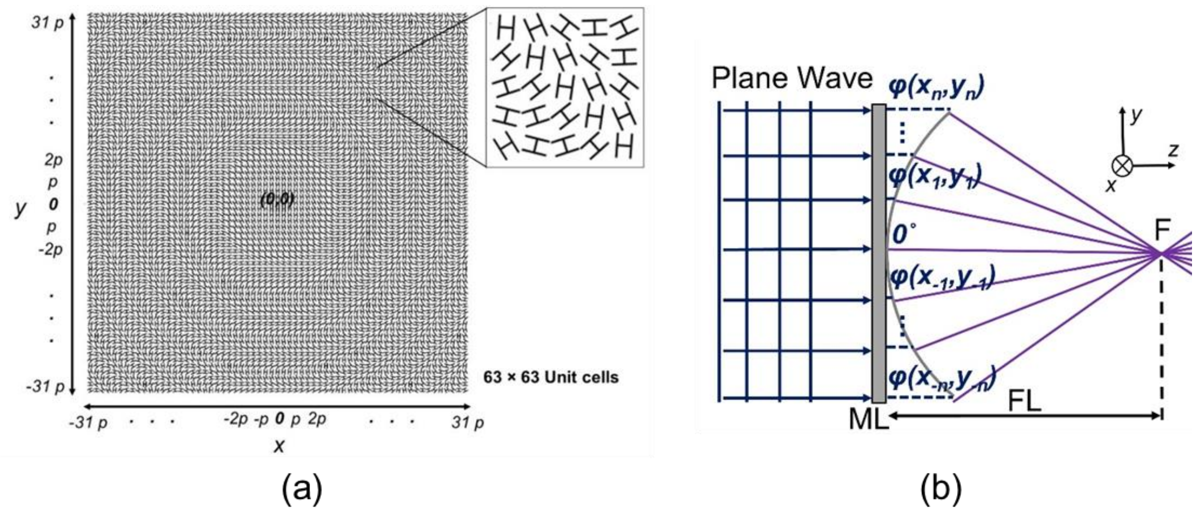

Fig. 3.6. *(a)* Metasurface mask. Every unit cell is located in x and y position from -31p to 31p, with p the unit cell period. *(b) Scheme of operation of the metalens excited by a plane wave which is focused at a focal point (F),* focal length (*FL*).

In our case, the operation frequency is fixed at f_0 = 87 GHz (λ_0=3.45 mm), as explained in the previous section and the FL is set at 70 mm (20.2λ_0).

To characterize the concordance between the PB theory and the simulated metalens, a preliminary unit cell rotation study using a parametric sweep of the rotation angle is performed and the magnitude of the converted circular polarization (T_{RL}) and phase (Φ) values for some of these angles (from 0 to 180 deg with a step of 40 deg) as a function of the frequency are plotted in Fig. 3.7. As it is seen, the optimal phase shift results, for presenting the best agreement with respect to the PB principle and also the maximum magnitudes are obtained around 87 GHz as expected.

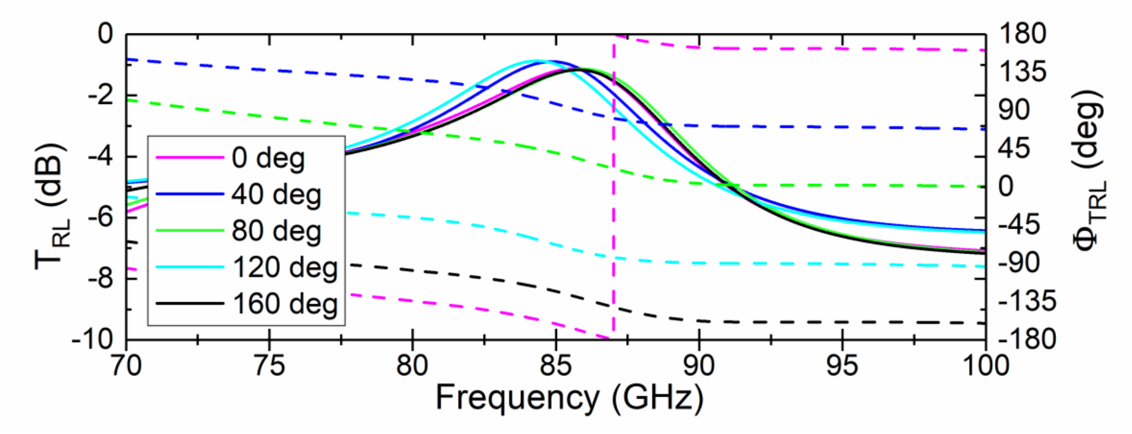

Fig. 3.7. T_{RL} magnitude (expressed in dB) and phase shift obtained as a function of the frequency for the rotation angles comprised between 0 and 160, deg with a 40 deg step.

Only slight discrepancies are appreciated with respect to the ideal phase shift values. However, in order to achieve an optimal metasurface phase response, a correction in the rotation angle of some cells is done. These new rotation values are extracted from the data of Fig. 3.8(a), where is possible to simultaneously visualize the ideal expected function (purple) according to PB principle and the obtained function (cyan) according to the simulated cell rotations. Furthermore, the black dots represent the rotation angles to implement (instead of the theoretical ones) with the aim to obtain the optimal phase shifts. This method is especially useful in the points where the distance with respect to the ideal phase is higher, as those comprised between 20 and 70 deg and between 120 to 160 deg. The correspondent magnitude values for the new rotation angles, which finally are implemented are shown in Fig. 3.8(b).

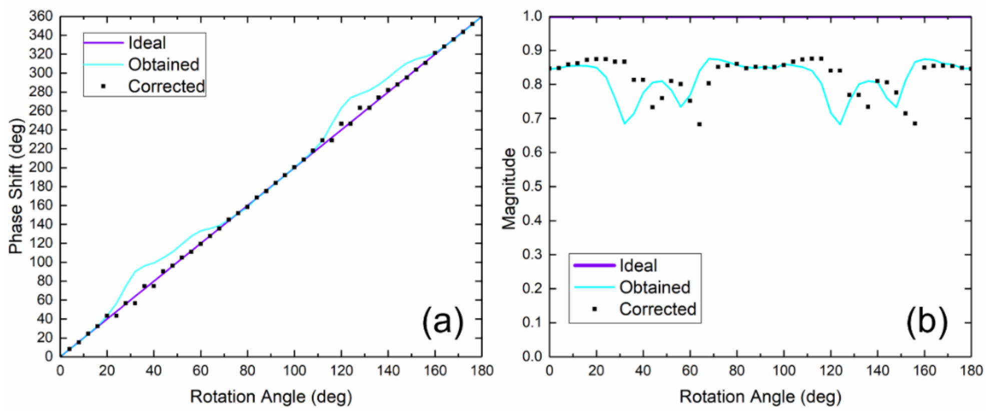

Fig. 3.8. Ideal phase shift (violet line) as a function of the rotation angle following the PB principle at 87 GHz. In cyan, the obtained phase shift in simulation is plotted as a function of the rotation angle. Black dots represent the rotation angle used to achieve closer values to the ideal function.

From this figure, it is possible to appreciate some cases where the magnitude result becomes increased, as the case around 30 deg, 120 deg or 140 deg and others where it is decreased, as near 40 deg, 60 or 150 deg, not presenting in any case substantially lower magnitude points than those observed in the original curve. In fig. 3.9(a), the ideal expected phases from PB theory are mapped along with the results after applying the rotation angle correction (fig. 3.9(b)), demonstrating an almost perfectly coincidence with the ideal values at 87 GHz.

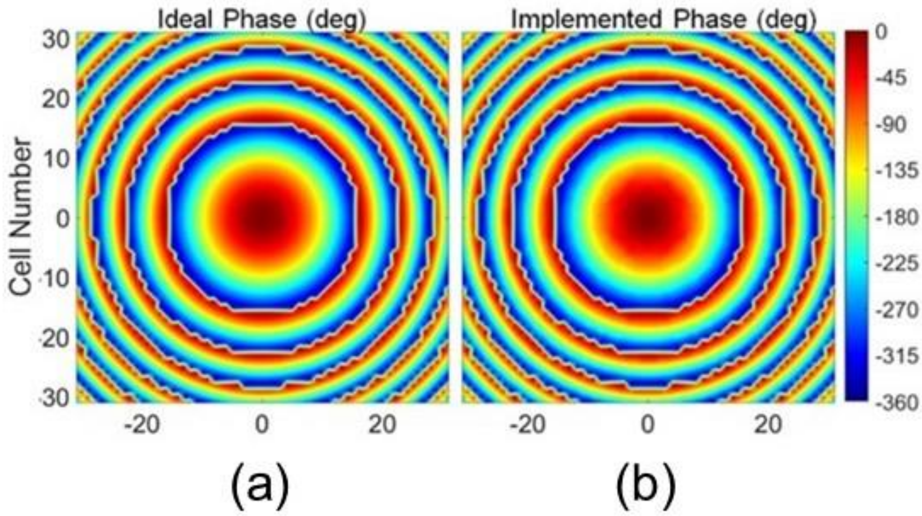

Fig. 3.9. (a) Ideal and (b) implemented discretized phase profile at the PB metalens (63×63 positions) as a function of the meta-atoms position (x,y) at 87 GHz.

For a better visualization of the results, a 1-D plot showing the obtained unit cell phases as a function of the central metalens row is plotted in Fig. 3.10, concluding with an outstanding agreement between the expected and implemented phase profile.

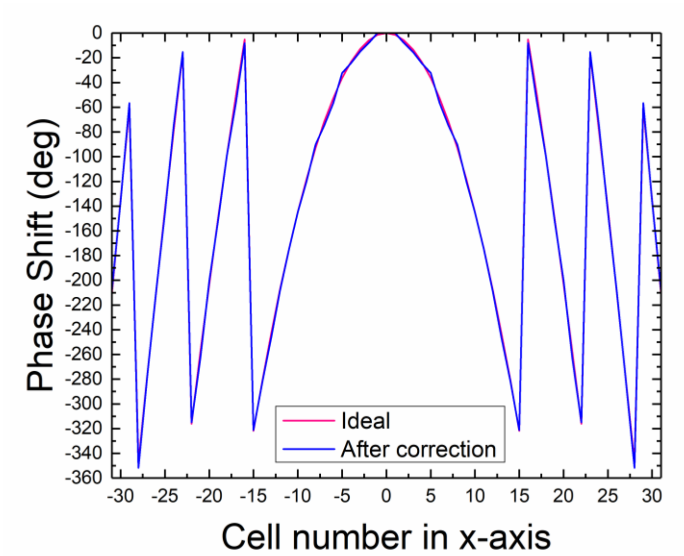

Fig. 3.10. (a) Comparison between ideal and implemented spatial phase profile of the central metalens row (x,0) after applying the rotation angle correction at 87 GHz.

After applying the correction at 87 GHz, the analysis of the metalens phase response is extended to the entire bandwidth with the aim to describe their behavior beyond the design frequency. For this purpose, the frequency domain solver of the electromagnetic simulator CST Studio Suite® is used, applying the software-defined Floquet boundary conditions adapted to periodic problems. In the numerical study, the response was obtained by combining the results of two different simulations using plane waves with horizontal and vertical polarization respectively. The structure was finely meshed with 17,875 tetrahedrons, and excited by a normally incident left-handed circularly polarized (LHCP) mode. A parametric sweep of the unit cell rotation from 0 deg to 180 deg with a step of 4° was done.

As the metalens converts the handedness at the output, we analyze the cross-polar transmission coefficient (T_{RL}) as we did before, both magnitude and phase, as a function of the frequency, see Fig. 3.11(a) and (b), respectively. In view of the results, the maximum T_{RL} magnitude still happens near the operation frequency (87 GHz) but is more stable with respect to the rotation angle at 85 GHz. In addition, the phase shows a variation of 360º with a smooth variation in frequency, which is characteristic of PB-based diffraction devices as the phase shift is achieved by the geometrical rotation and is not determined by a resonance of the unit cell [65].

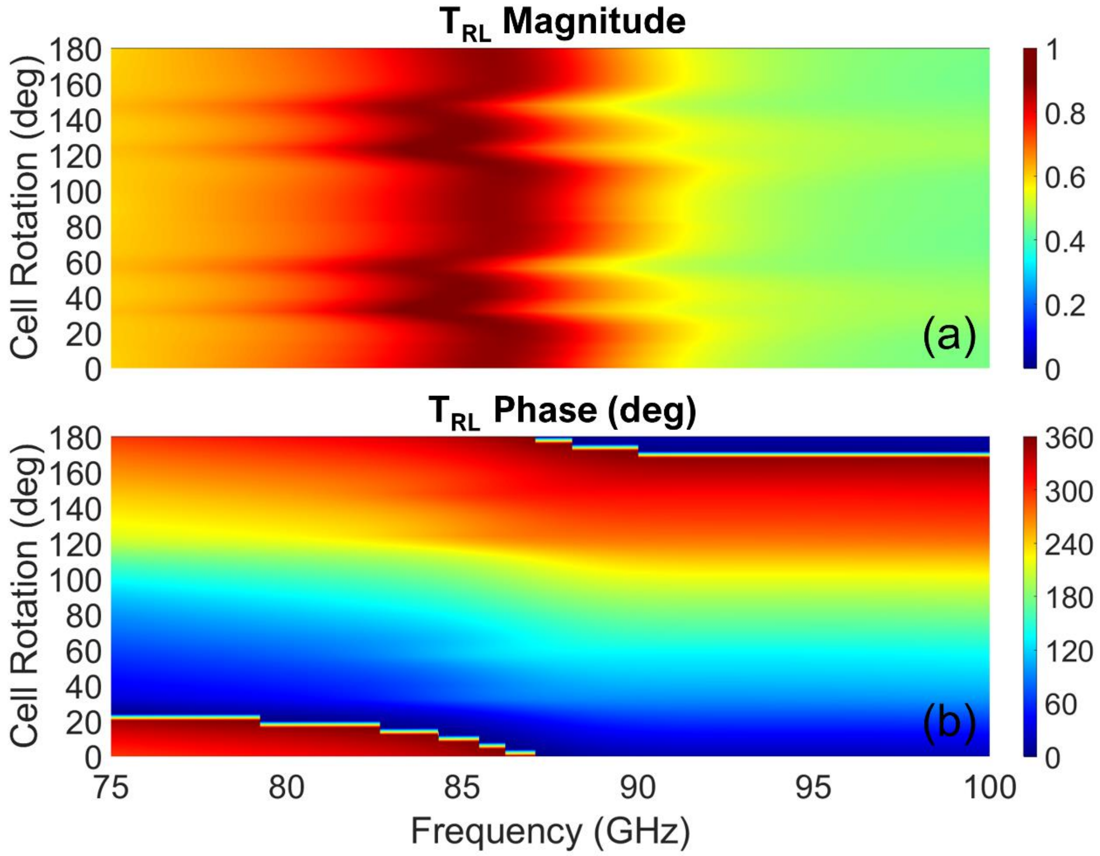

Fig. 3.11. (a) Normalized transmission coefficient magnitude and (b) phase, obtained from unit cell simulation as a function of the frequency and the unit cell rotation angle.

3.2.4 Metalens Focal Performances. Huygens-Fresnel Analysis

The magnitudes and phases as a function of the rotation angle and frequency, shown in the Fig. 3.11 of the previous section, were used to evaluate the focal performance of the device by mean of a semi-analytical study based on the H-F method, see Appendix B for a description. Thus, every metalens unit cell was consider as a point source with the correspondent value of magnitude and phase according to the rotation angle in every metalens position.

Fig. 3.12(a) presents the calculated T_{RL} magnitude (normalized to the maximum) as a function of the frequency and the distance along the optical z-axis at the metalens output. Fig. 3.12(b) shows the XPD. As observed in Fig. 3.12(a) the focus coincides largely but not precisely with the design values (87 GHz and 70 mm) both in frequency and *FL*. The maximum appears at 85 GHz and 67 mm, which is the frequency that has the most stable peak of magnitude as a function of the unit cell rotation angle, according to the results of Fig. 3.11. However, regarding XPD (Fig. 3.12(b)), the highest values (near 40 dB) are observed at the design values, the operation frequency of 87 GHz and *FL* = 70 mm.

From Fig. 3.12, it is evident that the metalens presents chromatic aberration, with an increasing FL for increasing frequency. However, the intensity fades out for frequencies far from the design frequency, especially in the upper band. As a consequence of this chromatic aberration, there is focalization between 60 and 80 mm depending on the operation frequency with XPD values above 10 dB in all cases.

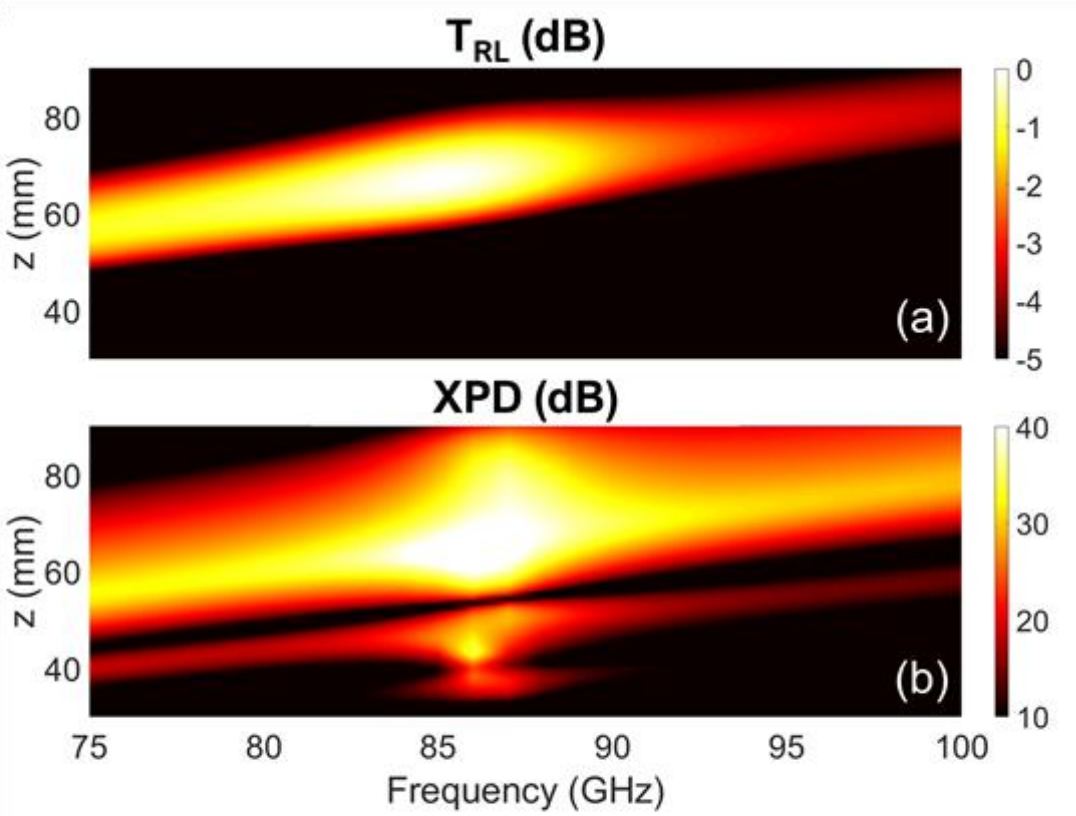

Fig. 3.12. Normalized T_{RL} magnitude (a) and XPD (b) extracted from H-F analysis expressed in dB as a function of the frequency and the distance from the metalens (z-axis) in mm.

3.2.5 Experimental Results and Discussion

The fabricated PB metalens is depicted in Fig. 3.13(a). The rotation of the lens unit cells or meta-atoms, which were defined in the previous section is easily appreciated in Fig. 3.13(b). The device presents a diameter of 87 mm and is embedded in a circular holder (black circle), as shown in Fig. 3.13(c), along with a picture of five constituent unit cells.

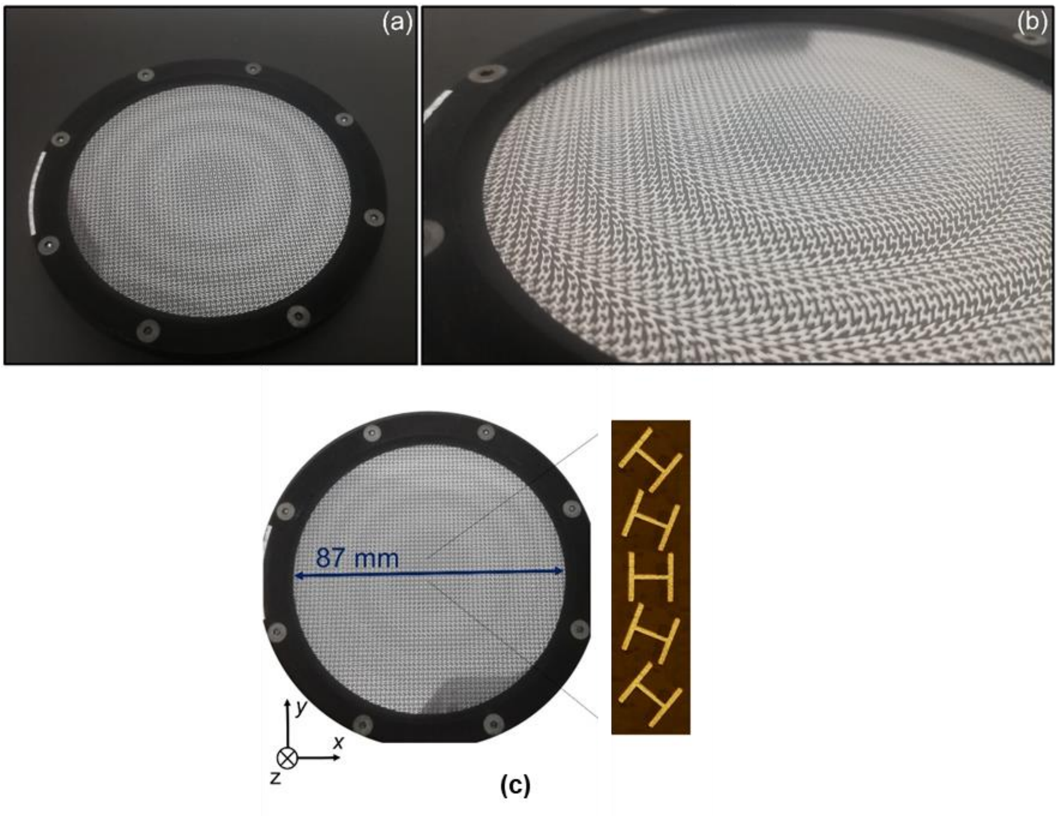

Fig. 3.13. (a) General view of the metalens with a diameter of 87 mm mounted in the circular holder (black). (b) Zoom of the metalens showing the H-shaped rotated elements. (c) Fabricated metalens picture (left) and microphotograph (right) of five central H-shaped, taken with a Mitutoyo Hyper MF U176-402-43 microscope with 50 × zoom.

The experimental setup to experimentally determine the focus is presented in Fig. 3.14(a). The metalens with the holder was embedded in the center of a methacrylate piece and mounted on a metallic part in the center of the measurement bench, Fig. 3.14(b).

In this configuration, the metalens was illuminated by a transmitting antenna consisting of a septum polarizer that feeds a corrugated horn antenna (CHA) with a low axial ratio at the frequencies of interest and is configured to get a LHCP at the output. The electric field at the output was measured along the z-axis with a linearly polarized open-ended rectangular waveguide probe (WR-10 standard waveguide) with sharp edges to reduce scattering. Both the transmitting antenna and the probe datasheets can be found in Anteral S.L. webpage [32]. An exhaustive alignment of the set-up components was carried out using a laser tracker, and a preliminary calibration between the antenna and the probe to center the antenna maximum with the probe center was done before placing the metalens. Both *x*- and *y*-components were obtained by rotating the probe in both horizontal and vertical orientations (polarizations) at each point. The field distribution was raster-scanned at each position in the *xy*-plane from –6 mm to 6 mm with a step of 0.5 mm (25×25 points). The phase error introduced by the probe rotation was corrected in a subsequent post-processing stage.

It must be emphasized that in our measurement set-up, the CHA antenna was placed at 21 cm from the metalens, which is the maximum distance available in our setup. We carefully measured the phase on the metalens plane and concluded that this distance is not enough to ensure a uniform phase incidence on the plane. The experimental results and the consequences derived from this limitation are explained in the following.

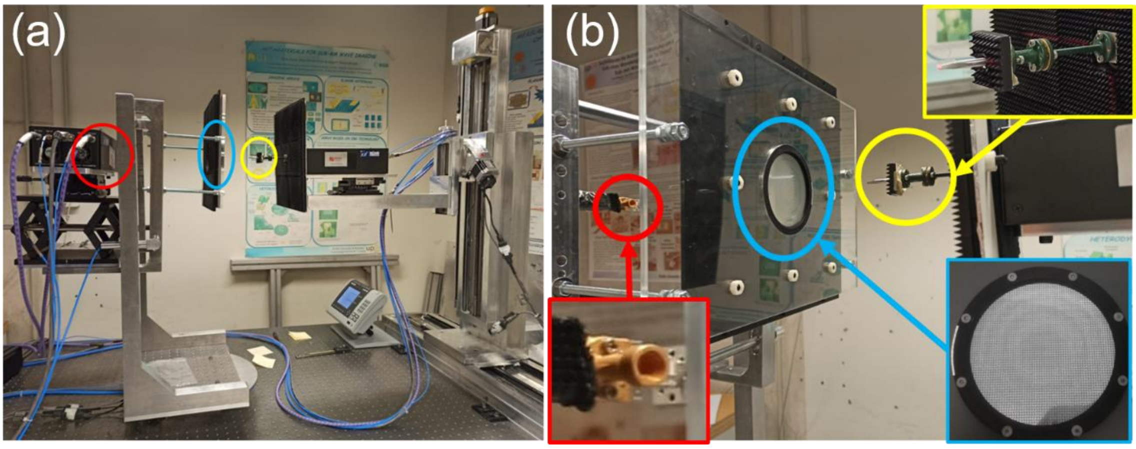

Fig. 3.14. (a) General photograph of the set-up where the transmitting antenna, metalens and receiver are presented in red, blue, and yellow circles, respectively. (b) Zoom photograph of the three main elements marked in (a). Bottom left and top right insets show detailed views of the transmitting antenna and receiving probe. The metalens and receiving probe are surrounded by absorbent material (black tiles).

Fig. 3.15 presents the experimental measurements to characterize the metalens *FL* and operation frequency. The results were obtained by sweeping the probe's location and frequency at each point. The probe was moved along the z-axis in the range [62, 112] mm (with a step of 2 mm), and the frequency was swept in the range [75, 105] GHz (with a step of 0.2 GHz). A subsequent linear to circular basis transformation was done to obtain the circular components. The obtained normalized experimental RHCP E-Field and XPD are shown in Fig. 3.15. There are some striking differences between the results presented in Fig. 3.13 and Fig. 3.15 that require further analysis.

First, we analyzed the illumination of the metalens. In the measurements, the CHA was placed at 21 cm from the metalens (at the limit of our experimental setup). So, to find the illumination profile, we measured the field at 25 mm from the CHA in a plane of 12×12 mm^2 and a step of 0.5 mm, using the mentioned probe. Using this data, we applied a near- to far-field transformation to obtain the electric field distribution at the metalens plane (at a distance of 21 cm from the CHA). This analysis indicates that the phase distribution impinging on the metalens is non-uniform. Fig. 3.16(a) shows the results using the actual illumination phase on the metalens, obtained by applying an H-F analysis. As observed there, when the illumination phase errors are introduced in the calculation, a *z*-axis offset is observed, shifting the *FL* in all the considered frequencies, in good agreement with the experimental values of Fig. 3.15.

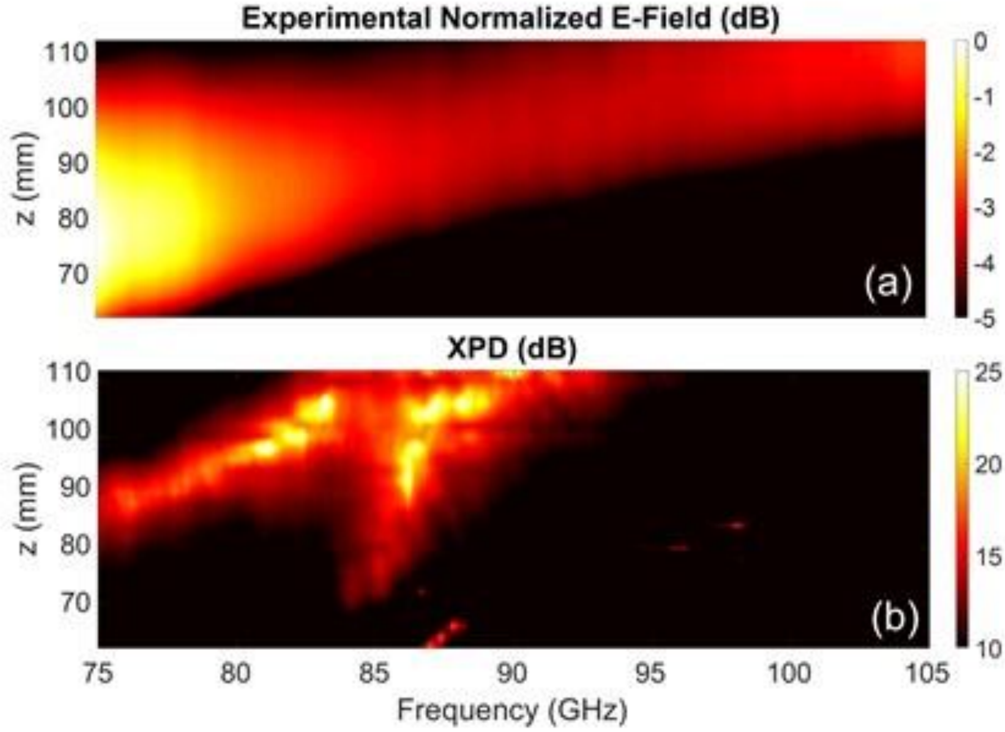

Fig. 3.15. Experimental normalized RHCP E-Field (a) and experimental XPD value (b) expressed in dB as a function of the frequency and the CHA distance from the metalens (z-axis) in mm.

Nevertheless, there are still discrepancies between the maximum value, which appears at 75 GHz in the measurements [Fig. 3.15(a)] and at 87 GHz in the new H-F calculations [Fig. 3.16(a)]. These can be explained by tolerance errors introduced in the metalens fabrication. To evaluate the influence of tolerance errors, the H-shaped elements that compose the metalens were measured by taking fifteen microscope samples of different unit cells and averaging the dimensions. Furthermore, the substrate thickness was also measured at different places to estimate also an average thickness value. The new parameters were introduced in a unit cell study similar to the **3.2.3** section, and the S-parameters were calculated with CST Studio Suite®. Finally, we used both the non-uniform illumination phase and fabrication errors in the H-F analysis. The results are shown in Fig. 3.16(b).

The agreement with the experimental results is unquestionably improved, demonstrating that the metalens operates satisfactorily and that the *FL* at 87 GHz is near 70 mm (the design value) despite the results presented in Fig. 3.15. Moreover, the *FL* shift is due to a non-uniform phase illumination and not due to manufacturing errors of the metalens.

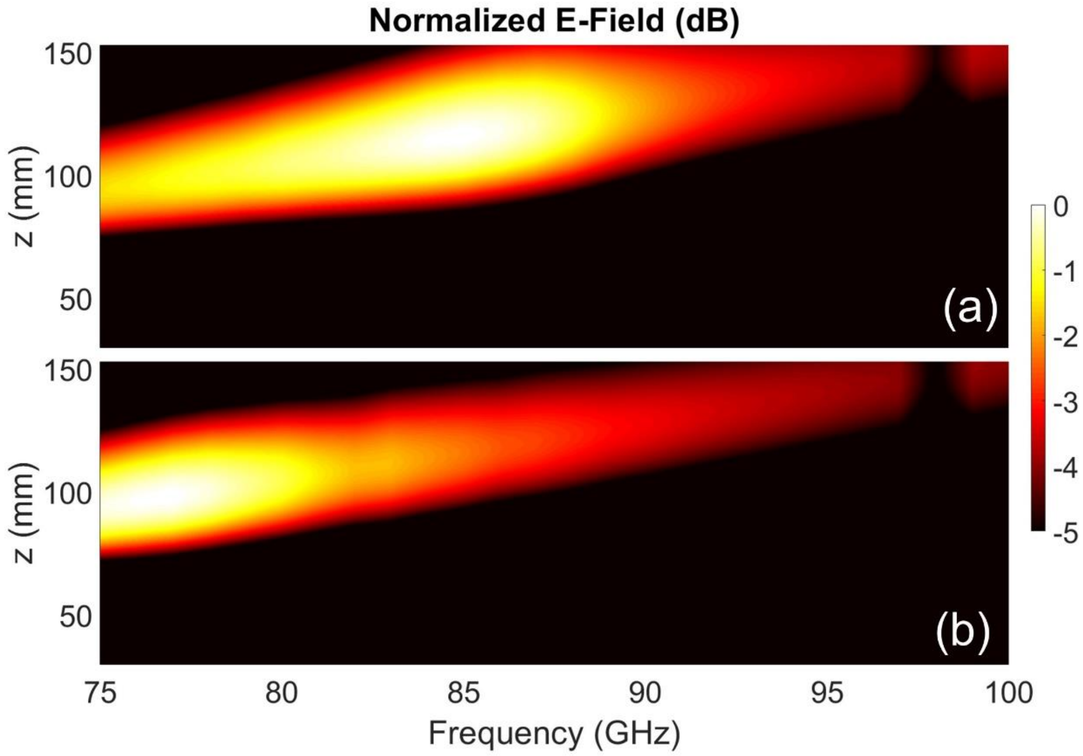

Fig. 3.16. Normalized RHCP E-Field at the metalens output, taking into account only the phases of the non-plane wave provided by the CHA at the metalens plane (a) and taking into account the phases along with the fabrication errors (b).

After this support to a deeper understand of the metalens focal performances behavior, a comparison between H-F numerical simulations and experimental results is depicted in Fig. 3.17 for discussion. For this comparison, it is important to keep in mind that both H-F and simulations, the impinging wave is a plane wave, and thus a uniform phase profile is presented on the metasurface. However, in the experiment, the phase profile of the incident wave is non-uniform, as was commented before.

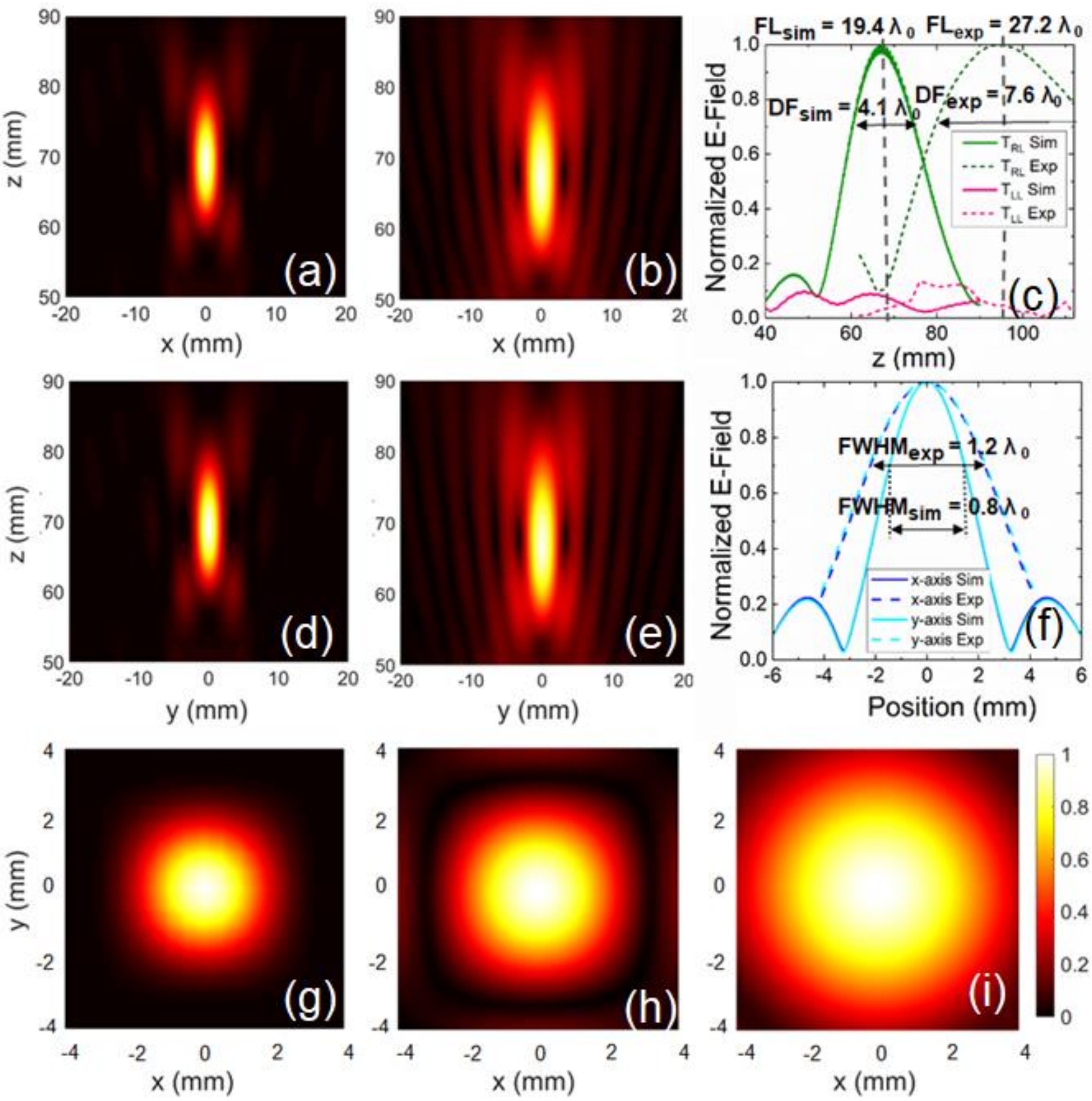

Fig. 3.17. Normalized RHCP E-field magnitude, considering an impinging plane wave at 87 GHz, extracted from H-F analysis and simulation for *xz*-plane (a),(b), *yz*-plane (d),(e) and *xy*-plane (g),(h). (c) Simulated and measured normalized E-field magnitude for RHCP and LHCP along the optical axis (z-axis). (f) Simulated and measured normalized E-field magnitude for RHCP at the focus tracked along x- and y-axes. In (i), the normalized RHCP E-field magnitude at the *xy*-plane of the experimental metalens is depicted at 87 GHz.

The H-F analysis and simulation results are shown in the first two columns of Fig. 3.17, respectively. In that figure, panels [(a),(b)], [(d),(e)] and [(g),(h)] represent the normalized RHCP electric field magnitude in the *xz*-, *yz*- and *xy*- cutting planes, respectively. The agreement between analytical and numerical results is good (see Table I). The small disagreements can be attributed to the coupling between adjacent cells (disregarded in the H-F analysis) and point source approximation in H-F analysis. The full width at half-maximum (FWHM), which define the width between axis points where the field maximum decays 3 dB, is identical for the *x*- and *y*-axis in simulation and H-F, ensuring a nearly perfectly circular shape of the focus. The simulated FWHM is $0.8\lambda_0$, a bit smaller than the Rayleigh diffraction limit ($0.61\lambda_0$/NA= $0.87\lambda_0$), where NA is the numerical aperture of the lens, as it was introduced in the Background section. Furthermore, the simulated focus presents a low sidelobe level of 0.21 (–13.26 dB) at ±4.6 mm, as shown in Fig. 3.17(f).

The experimental measurements, Fig. 3.17(c), shows an experimental *FL* at 94 mm (see Table IV), which deviates from the numerical value by 27 mm ($7.8\lambda_0$). Likewise, the depth of focus (*DoF*) is wider than in the simulation. We estimate a broadening of 13.9 mm ($4\lambda_0$) since it is impossible to measure the actual value due to the *z*-axis stage's limitations (the positioner along z was mechanically limited from 62 to 112 mm with respect to the metasurface). Thus, this estimated value is calculated as the double the width measured between the point for the maximum E-Field value and the point where the E-Field decays by 3 dB (0.7), which happens at 80 mm. By looking at the normalized level of T_{LL} at the focus, an experimental XPD value of 25 (27.9 dB) is observed, which is even higher than the simulated of 12 (21.6 dB), demonstrating an outstanding level of polarization conversion at the focus. The FWHM values for simulation and measurement, depicted in Fig. 3.17(f), also show that the experimental focus undergoes a widening in the *x*- and *y*-axis of 1.4 mm ($0.4\lambda_0$), so the experimental lens resolution is $1.2\lambda_0$ (≈7% above of the Rayleigh resolution limit). The FWHM widening can be observed by comparing Figs. 3.17(g-i), where the H-F, numerical, and the experimental *xy*-planes, respectively, are shown. Moreover, all cases demonstrate the circularity of the focus.

The discrepancies between simulation and measurement have been detailed explained. Manufacturing tolerances in the substrate's thickness may also play a role, although to a lesser extent. Nevertheless, the PB metalens demonstrates an excellent behavior as a polarization converter and a lens simultaneously, reaching a very high level of XPD.

TABLE IV
COMPARISON H-F SIMULATION AND EXPERIMENTAL

Model	*FWHM (mm)*	**DoF (mm)*	*FL (mm)*
H-F	2.0	10.5	69
Simulation	2.7	14.1	67
Experimental	4.1	28	94

**DoF is the depth of focus*

3.3 Antenna-PBM Metalens System

3.3.1 Background

The intensive research on PBM devices has been applied to antenna systems with the aim to get compact and planar devices capable of manipulating the amplitude, phase, and/or polarization of electromagnetic waves, as mentioned in section **3.1**. Thus, the combination of PBM and antenna is intended to achieve high gain or low AR performance with the advantage of having a low profile.

Besides the gain and AR, an important parameter in these lens-antenna systems is the aperture efficiency, which is calculated as A_e/A_p, being $A_e = D\,\lambda^2/4\pi$ the effective aperture area and A_p the physical aperture area, with D the directivity in linear magnitude at boresight and λ the wavelength.

Several PBM systems have been demonstrated to date, such as one operating in the Ka band [64], at 20.7 GHz with an axial ratio (AR) near 2 dB, gain of 21.5 dB, and an aperture efficiency of 29%; or a vortex generator also working in Ka band [69], whose single-beam configuration reaches a peak aperture efficiency value of 39.1% around 27.5 GHz with an AR < 3 dB and a gain of 22.6 dB. There are also interesting examples of devices operating at other frequency bands, such as the system operating at 11 GHz [70], where a peak gain of 21.6 dB and an AR < 3 dB is achieved, presenting an aperture efficiency value near 34%. Moreover, a recent design for CubeSat links in K-band [71] has reached a high aperture efficiency of 57%, with an AR near 0.6 dB operating around 24.6 GHz and 31.6 dB of peak gain.

Despite the excellent performance of the devices analyzed in the mentioned works, all of them are based on tri-layer metasurfaces designs. Bi-layer devices found in the literature are mainly based on non-uniform cell metasurfaces, following the first method previously mentioned in section **3.1**. In Ref. [65], a bi-layer antenna-lens system based on a PB metasurface was reported, but the study was restricted to numerical simulations without experimental proof. In the next section, we experimentally evaluate the performance of the previously introduced metalens as PBAM system.

3.3.2 Experimental Results

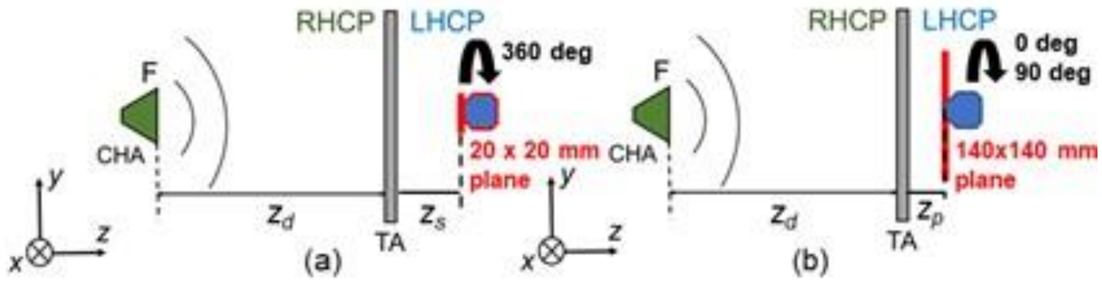

Fig. 3.18. Schematic of the metalens-antenna system. (a) Configuration of the AR ellipse measurement. The CHA is placed at *zd* = 60, 70 and 80 mm from the metalens and the near field is measured at the other side in a 20×20 mm^2 *xy*-plane at *zs* = 25 mm from the metalens. The probe is rotated from 0 to 360 deg around its axis with a 10 deg step. (b) Configuration of the radiation pattern measurement. The CHA is placed at *zd* = 60, 70 and 80 mm from the metalens and the near field is measured at the other side (at *zp* = 50 mm) in every point of a 140×140 mm^2 *xy*-plane with a 1.4 mm step. The probe is oriented in two different position (0 and 90 deg) in each plane to compose the field in a circular polarization base.

The antenna-metalens system was characterized using the setup shown in Fig. 3.17. The illumination was done using a CHA that generates an LHCP wave and operates between 75 GHz and 105 GHz (see full antenna performance in the manufacturer's web page). The CHA aperture edge (coinciding with its phase center) was placed at three different positions: $z = 60$ mm, $z = 70$ mm (metalens focus position), and 80 mm from the metalens to lead a full characterization of the system, taking into account the metalens focalization.

The AR at boresight was extracted from the AR ellipse measured by a near-field probe placed at 25 mm from the metalens in a 20×20 mm^2 *xy* plane centered in the lens axis with a step of 1 mm (Fig. 3.18(a)). At each point the probe was rotated around its axis from 0 deg to 360 deg with a step of 10 deg and the ratio between the maximum and minimum field values obtained from the rotation was calculated. The frequency sweep was done for each angle from 75 to 105 GHz with a step of 0.2 GHz. Fig. 3.19(a) presents the experimental AR results for the CHA alone (black curve) and the PBAM system with the antenna at 60 mm (red curve), 70 mm (green curve), and 80 mm (blue curve) as a function of the frequency. The CHA has a good AR with values below 3 dB for almost the entire band except at its lower part and near 98 GHz, where a peak arises. When the CHA is placed at 70 mm, the AR at the operation frequency is below 1 dB (0.5 dB at 87 GHz). The peak at 98 GHz is smeared out as the metalens act as a polarization filter reflecting the undesired component introduced by the CHA. Likewise, the AR is also improved in the lower frequency band with respect to the CHA alone. When the CHA is placed at 60 mm, the main improvement is found in the low-frequency band, whereas the AR is degraded at high frequencies. Finally, at 80 mm, the best AR happens at high frequencies, but in general, the behavior is worse than the other cases with AR above 1 dB in the entire measured band. These results agree and can be explained by the metalens chromatic aberration observed in Fig. 3.13. Indeed, as shown in Fig. 3.13(a), the intensity at the focal point fades out at high frequencies, indicating a degraded metalens operation.

For the characterization of the directivity and radiation patterns (Fig. 3.18(b)), the electric field (*x* and *y* components) at the output of the lens was measured by rotation (0 and 90 deg) of a linear near-field probe in a 140×140 mm^2 *xy* plane with a step of 1.4 mm at 50 mm from the metalens. At each position, a frequency sweep was performed from 75 to 105 GHz with a step of 0.2 GHz. Afterward, a linear to circular polarization transformation and a subsequent near- to far-field transformation was done by means of a Matlab script to obtain the far field parameters of the PBAM system.

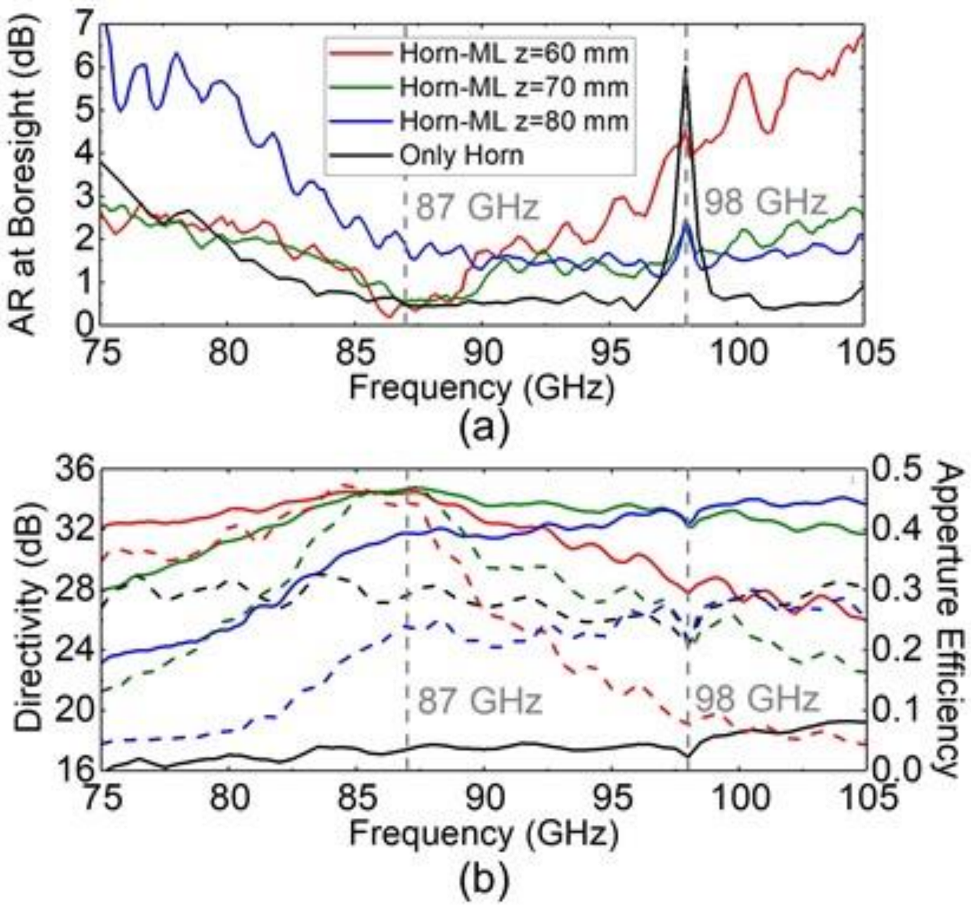

Fig. 3.19. (a) Experimental AR extracted from the polarization ellipse. (b) Directivity and aperture efficiency measured at boresight for the CHA and the PBAM placing for distances zd = 60 mm, zd = 70 mm, and zd = 80 mm from the metalens.

The directivity as a function of frequency is plotted in Fig. 3.19(b). A significant enhancement with respect to the values for the CHA alone is evident for the three measured cases, revealing the system's robustness with respect to the exact CHA position. The average enhancement along the full band at 70 mm is near 14.5 dB, reaching a maximum directivity peak of 34.7 dB at 87 GHz. Once again, shorter distances (60 mm) provide higher directivity at low frequencies and longer distances (80 mm) at high frequencies. Closely related to the directivity, the aperture efficiency is depicted in Fig. 3.19(b). The maximum occurs at 70 mm and 87 GHz with a value near 47%, implying an efficiency enhancement of 18% with respect to the isolated CHA. Moreover, due to the chromatic aberration, the aperture efficiency is above 35% at 60 mm from 75 to 88 GHz and between 20-30% at 80 mm from 85 to 105 GHz.

The radiation patterns obtained at 60, 70, and 80 mm from the metalens for three different frequencies, 75, 87, and 98 GHz, are presented in Fig. 3.20 as a function of the elevation angle (θ) and four different cutting planes in the azimuth angle (φ) of 0, 45, 90, and 135 deg. For simplicity, we call hereinafter co-polarization (CP) to the RHCP mode (solid lines) as this is the one radiated by the antenna-metalens system and cross polarization (XP) to the LHCP mode (dashed lines). For the sake of comparison, in Fig. 3.20(a-c) are represented the patterns of the isolated CHA. The rest of panels correspond to the lens-antenna system with the CHA at z = 60 mm (Fig. 3.20(d-f)), z = 70 mm (Fig. 3.20(g-i)) and z = 80 mm (Fig. 3.20(j-l)).

Before analyzing each case separately, it is evident from the measured results that in all cases, the addition of the metalens narrows the beam at broadside compared with the isolated CHA, leading to an increment of directivity (already seen in Fig. 3.19). The radiation pattern is largely uniform with respect to azimuth, giving evidence of a good revolution symmetry. In addition, sidelobes are relatively low, with a sidelobe level below –20 dB in all cases. Finally, the wave at the output has a good polarization purity with a crosspolar level below –15 dB in most cases.

Focusing now on the results obtained at 87 GHz and 70 mm [Fig. 3.20(h)], we find an excellent undesired polarization rejection around 30 dB at broadside. This value is very similar to the one presented by the isolated CHA [Fig. 3.19(b)], as was expected from the similar AR value of both cases at 87 GHz. Furthermore, an obvious beam narrowing (around 23 deg) with respect to the isolated CHA is observed, presenting a –3dB-beamwidth of only 3 deg for the PBAM versus the 26.3 deg of the CHA, in concordance with the directivity increment observed in Fig. 3.19(b). Moreover, a low sidelobe of –25 dB is obtained. For the other distance configurations at the same frequency [Fig. 3.20(e) and (k)], a similar behavior is observed with XP levels at boresight direction around –30 dB and –20 dB at 60 and 80 mm, respectively, and a significant beam narrowing with respect to the CHA, in both cases with a –3dB-beamwidth near 3 deg.

Regarding the other cases, it is found that the performance at 75 GHz (first column) is optimum when the distance is 60 mm (Fig. 3.20(d)) with a –3dB-beamwidth of 3.4 deg and the radiation pattern is degraded at other distances, as expected. Likewise, the behavior at 98 GHz is optimum for a distance of 80 mm with a –3dB-beamwidth of 2.5 deg.

Finally, in Table V, a comparison between all these configurations is shown, revealing not only the optimal system performances for the case z = 70 mm and at 87

GHz, but also the excellent performance of the system for z = 60 and 80 mm operating at 75 and 98 GHz, respectively.

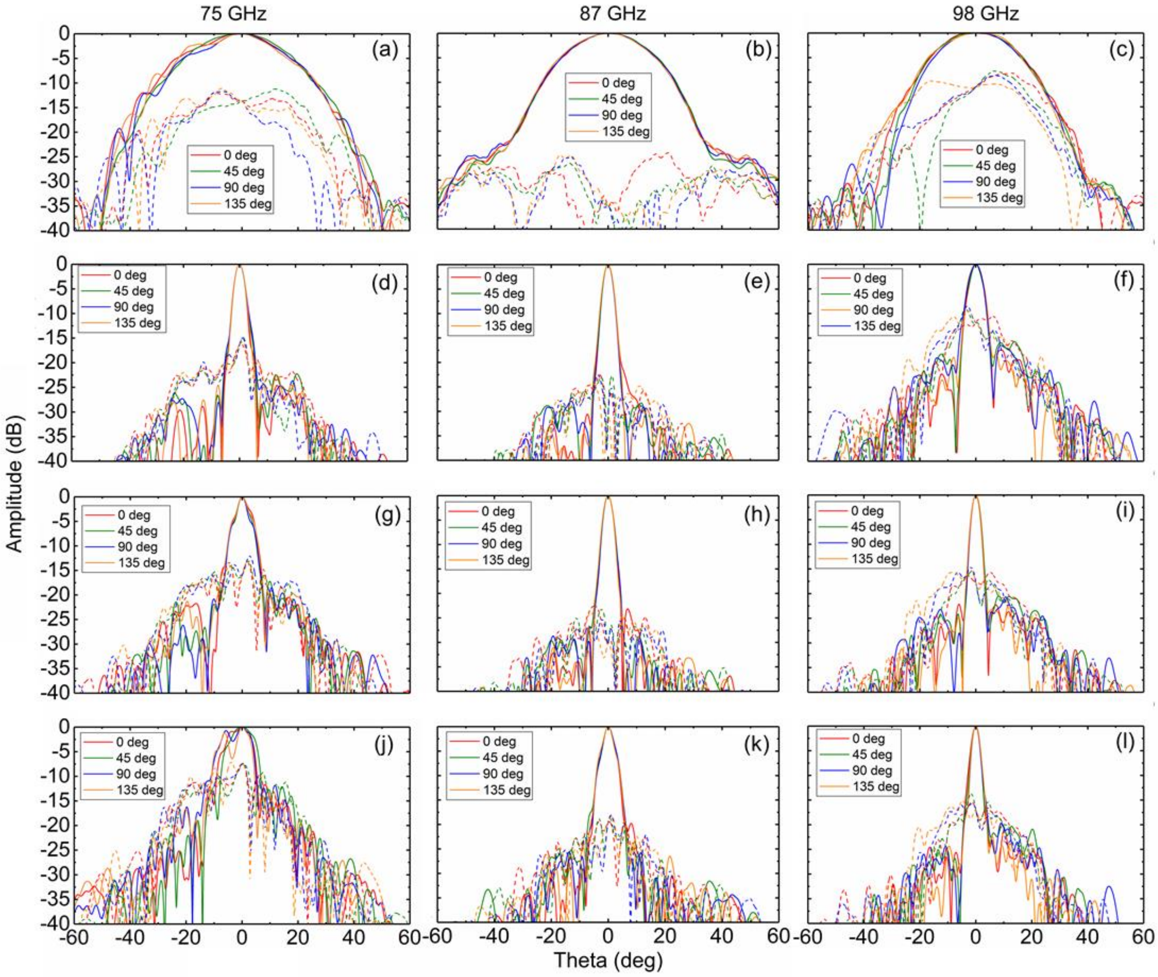

Fig. 3.20. Isolated CHA radiation pattern measured at 75 GHz, 87 GHz, and 98 GHz (a-c) and PBAM radiation pattern for distances between CHA and metalens of 60 mm (d-f), 70 mm (g-i), and 80 mm (j-l) measured at 75 GHz, 87 GHz, and 98 GHz respectively. Solid and dashed lines present CP and XP values, respectively.

TABLE V
HWPTA CONFIGURATION COMPARISON

Config.	*Freq (GHz)*	**D(dB)*	***BW-3dB (deg)*	*AR (dB)*	****Ap. Eff (%)*
CHA	75	15.8	28.5	3.8	26.9
60 mm		32.0	3.4	2.6	34.8
70 mm		27.9	3.9	2.8	13.1
80 mm		25.3	11.4	7.8	4.4
CHA	87	17.4	26.3	0.5	29.1
60 mm		34.5	3.2	0.5	44.2
70 mm		34.7	3.0	0.5	46.9
80 mm		31.7	3.4	1.8	23.9
CHA	98	16.9	26.7	6.0	20.4
60 mm		27.6	3.9	4.5	7.5
70 mm		32.1	2.8	2.2	20.5
80 mm		32.3	2.8	2.5	21.4

**D is the Directivity.*
***BW-3dB corresponds with the beamwidth measured at -3 dB.*
****Ap. Eff is the Aperture Efficiency.*

3.4 Summary

We have presented a PBM lens with only two layers, operating at 87 GHz, which converts the handedness of the CP incident waves with a transmission efficiency of 90.15%. A very high level of XPD (27.9 dB) at the focus is obtained, demonstrating a high level of polarization conversion and almost perfect circular polarization. The PBM lens has been integrated in an antenna-metalens system, achieving the polarization conversion with an AR of 0.5 dB and improving the antenna directivity around 17 dB.

Chapter 4. Conclusions and Future lines

4.1 Conclusions

The research work presented in this thesis comprises the design and experimental realization of half-wave plate polarization converters based on metasurfaces with only two layers. The design point of view for the devices presented in chapter 2 and chapter 3 is different, being the first one centered only in the polarization conversion, making use of the self-complementary structures robustness properties to develop a half-wave plate device for wavefront polarization control with robust circular polarization conversion. Otherwise, the device from chapter 3 makes use of PBM phase properties to create a half-wave plate device for wavefront engineering with a metalens functionality. Furthermore, the second one has been integrated in an antenna-metalens system, achieving a significant improvement of the antenna performances. The idea behind this thesis is to demonstrate the possibility to reach high levels of transmission efficiency with the maximum reduction in the number of layers respect to the devices usually demonstrated. Here we provide a summary of the obtained results and the possible future lines.

- We have analyzed in detail the performance of the ultrathin transmissive HWP based on a bi-layered ZZ metasurface designed for operation at 150 GHz. Having the thickness of $\lambda/20$, the fabricated device revealed excellent agreement with the numerical simulations, reaching a maximum transmission coefficient magnitude of -0.78 dB (i.e., the polarization conversion efficiency is over 90%), and an XPD $\sim$30 dB, with a fractional BW near 9%.
- The robustness of the device with respect to possible misalignments between layers introduced in the manufacturing process has been analyzed in detail. From the analysis performed, it has been clarified that the response is extremely robust with regards to a shift along the x-direction (i.e., perpendicularly to the guiding lines of zigzags), whereas it varies more considerably with a shift along the y-direction (i.e., along the guiding lines of zigzags). It is worth noting that even in the worst case, the performance of the device as a HWP still remains excellent although shifted in frequency.
- A subsequent study has clarified that the response is very stable for any misalignment under linear vertical polarization excitation, but it is very dependent on misalignments along y under linear horizontally polarized excitation. We have ascertained that this is due to the strong electrical coupling between layers, whose field distribution has a strong dependence on a shift along y. The results of this work extend and complement other approaches to develop polarization

conversion devices, in a compact realization and with excellent performance, such as low insertion losses and a relatively broad BW.

- We have analytically, numerically, and experimentally demonstrated an ultrathin ($<\lambda/13$) PBM lens. The structure operates at 87GHz and converts the handedness of the CP incident waves reaching a transmission efficiency of 90.15% with only two layers.
- Furthermore, a very high level of XPD (27.9dB) at the focus is presented, which indicates an outstanding level of polarization conversion and almost perfect circular polarization at the focal point. The energy of the incident wave is focused at 27.2 λ from the metasurface and presents a DOF around 7λ with an enhancement of 19.7dB and an FWHM near λ.
- The advantages provided by these ultrathin PB metalens are the very high cross-polar transmission efficiency and the excellent rejection of co-polarization, allowing circular crosspolarization with high purity. Hence, the proposed device may find application in lens systems operating at millimeter waves where ease of integration is essential and circular polarization conversion with high efficiency and purity are required. Furthermore, due to the full phase coverage presented by the meta-atoms, it is possible to engineer a different metasurface configuration in order to obtain a different functionality, *i.e.*, beamforming.

- We have implemented an antenna-metalens system with a bi-layer metalens based on the PB principle. It has been designed to operate at 87 GHz with a focal length of 70 mm. For these design parameters, the system can convert the circular polarization of the incident wave with an AR value of 0.5 dB, demonstrating an excellent polarization purity.
- Furthermore, the directivity of the original isolated antenna is highly improved by more than 17 dB, presenting an outstanding level of 34.7 dB along with a significant beam narrowing from 26.33 deg (antenna alone) to 3 deg (antenna-metalens).
- Besides, the system presents an aperture efficiency of 47%. Furthermore, the system is demonstrated to operate from 82 GHz to 95 GHz, with an AR lower than 2 dB, directivity higher than 32 dB and aperture efficiency > 0%. Finally, two additional configurations are tested by placing the antenna at 60 and 80 mm from the metalens. This way and due to the chromatic aberration of the metalens it is demonstrated that the system can still work but at different frequencies in the range between 75 GHz and 105 GHz, with directivities ~32 dB and AR < 3 dB.
- High levels of aperture efficiency near 35% and between 20 and 30% for the lower and higher parts of this spectrum have been experimentally demonstrated. These results suggest that the antenna-PBAM system can be a good candidate for telecommunication applications where pure polarization conversion and high directionality are required.

All the analysis presented here are general and could be extended to other frequency ranges by properly rescaling the geometry parameters of the metasurfaces.

4.1 Conclusiones

El trabajo de investigación presentado en esta tesis comprende el diseño y realización experimental de conversores de polarización (platos de onda) basados en metasuperficies de sólo dos capas. Se ha demostrado un dispositivo de plato de media onda para el control de la polarización del frente de onda que presenta una conversión de polarización circular robusta y un plato de media onda para la manipulación del frente de onda con funcionalidad de metalente. Este último ha sido integrado en un sistema de antena-metalente, consiguiendo una mejora significativa de las prestaciones de la antena. La idea detrás de esta tesis es demostrar la posibilidad de alcanzar altos niveles de eficiencia de transmisión con la máxima reducción en el número de capas respecto a los dispositivos demostrados habitualmente. A continuación, ofrecemos un resumen de los resultados obtenidos y las posibles líneas futuras.

• Hemos analizado en detalle el rendimiento de un HWP ultradelgado, que opera en transmisión, basado en una metasuperficie ZZ bicapa diseñada para operar a 150 GHz. Con un grosor de $\lambda/20$, el dispositivo fabricado reveló una excelente concordancia con las simulaciones numéricas, alcanzando una magnitud máxima del coeficiente de transmisión de −0,78 dB (es decir, la eficiencia de conversión de polarización es superior al 90 %) y un XPD de ∼30 dB, con un BW fraccional cercano al 9%. Se ha analizado en detalle la robustez del dispositivo frente a posibles desalineamientos entre capas introducidos durante el proceso de fabricación. Del análisis realizado, ha sido clarificado que la respuesta es extremadamente robusta respecto a cambios en la dirección *x* (es decir, perpendicularmente a las líneas guía de los zigzags), mientras que varía considerablemente más con un cambio en la dirección *y* (es decir, a lo largo de las líneas guía de los zigzags). Vale la pena señalar que, incluso en el peor de los casos, el rendimiento del dispositivo como HWP sigue siendo excelente, aunque cambie de frecuencia de operación. Un estudio posterior ha verificado que la respuesta es muy estable para cualquier desalineamiento bajo excitación con polarización vertical lineal, pero depende mucho de los desalineamientos a lo largo de *y* bajo excitación de polarización horizontal lineal. Hemos averiguado que esto se debe al fuerte acoplo eléctrico existente entre capas, cuya distribución de campo tiene una gran dependencia con el desplazamiento a lo largo de *y*. Los resultados de este trabajo amplían y complementan otros enfoques para desarrollar dispositivos de conversión de polarización, con una realización compacta y excelente rendimiento, así como bajas pérdidas de inserción y un ancho de banda relativamente amplio.

• Hemos demostrado analítica, numérica y experimentalmente una lente PBM ultradelgada ($<\lambda/13$). La estructura opera a 87 GHz y convierte el sentido de polarización de las ondas incidentes circularmente polarizadas, alcanzando una eficiencia de transmisión del 90.15% con solo dos capas. Además, se presenta un valor muy alto de XPD (27,9 dB) en el foco, lo que indica un nivel sobresaliente de conversión de polarización y una polarización circular casi perfecta en el punto focal. La energía de la onda incidente se concentra en 27.2 λ desde la metasuperficie y presenta un DOF de alrededor de 7 λ con una mejora de 19.7 dB y un FWHM cercano a λ. Las ventajas proporcionadas por estas metalentes PB ultrafinas son la muy alta eficiencia de transmisión de polarización cruzada y el excelente rechazo de la copolarización, lo que permite una polarización cruzada circular con alta pureza. Por lo tanto, el dispositivo propuesto puede encontrar aplicación en sistemas de lentes que funcionan en ondas milimétricas donde la facilidad de integración es esencial y se requiere conversión de polarización circular con alta eficiencia y pureza. Además, debido a la cobertura de fase completa que presentan los meta-átomos, es posible diseñar una configuración de metasuperficie diferente para obtener una funcionalidad diferente, por ejemplo, formación de haces.

• Hemos implementado un sistema antena-metalente con una metalente bicapa basada en el principio de PB. La lente ha sido diseñada para operar a 87 GHz con una distancia focal de 70 mm. Para estos parámetros de diseño, el sistema puede convertir la polarización circular de la onda incidente con un valor AR de 0.5 dB, demostrando una excelente pureza de polarización. Además, la directividad de la antena aislada original se mejora considerablemente en más de 17 dB, presentando un nivel sobresaliente de 34.7 dB junto con un estrechamiento significativo del haz de 26.33 grados (solo antena) a 3 grados (antena-metalente). Es más, el sistema presenta una eficiencia de apertura del 47%. Además, se demuestra que el sistema opera de 82 GHz a 95 GHz, con un AR inferior a 2 dB, directividad superior a 32 dB y eficiencia de apertura > 30%. Finalmente, se prueban dos configuraciones adicionales colocando la antena a 60 y 80 mm de la metalente. De esta forma y debido a la aberración cromática de las metalente, se demuestra que el sistema aún puede funcionar, pero a diferentes frecuencias en el rango entre 75 GHz y 105 GHz, con directividades ~32 dB y AR < 3 dB. Así, se han probado experimentalmente altos niveles de eficiencia de apertura cercanos al 35% y entre el 20 y el 30% para las partes inferior y superior de este espectro. Estos resultados sugieren que el sistema antena-PBAM puede ser un buen candidato para aplicaciones de telecomunicaciones donde se requiere conversión de polarización pura y alta direccionalidad.

Todos los análisis presentados aquí son generales y podrían extenderse a otros rangos de frecuencia redimensionando adecuadamente los parámetros geométricos de las metasuperficies.

4.2 Future Lines and General Comments

- Given the high polarization purity observed with the PBM lens operating in the antenna-metalens system and the capability of the this to equalize the AR in those frequency points where the worst values were obtained and the high aperture efficiency presented by the metasurface, even not being the antenna properly designed to maximize the illumination efficiency in this, a new antenna design has been proposed with the aim to obtain the maximum system performance. Thus, a current project in collaboration with the Anteral company is being developed to extend the research.

- A beamforming design with the PBM metasurface by changing the meta-atoms rotation angles has been performed and some preliminary simulation results obtained, being a current researching topic.

During the development of this thesis two more researching lines, different to the topic presented in this work, were open. The first one was related to the design of a topological insulator device and the second one to electromagnetic rainbow-trapping, as an equivalence or translation from the acoustic to electromagnetic waves. Both topics continue opened to research.

4.2 Líneas Futuras

- Dada la alta pureza de polarización observada con la lente PBM operando en el sistema antena-metalente y la capacidad de ésta para ecualizar el AR en aquellos puntos de frecuencia donde se obtuvieron los peores valores y la alta eficiencia de apertura que presenta la metasuperficie, incluso no estando la antena correctamente diseñada para maximizar la eficiencia de iluminación en ésta, se ha propuesto un nuevo diseño de antena con el objetivo de obtener el máximo rendimiento del sistema. Así mismo, actualmente se está desarrollando un proyecto en colaboración con la empresa Anteral para ampliar la investigación.

- Se ha realizado un diseño para formación de haces con la metasuperficie PBM cambiando los ángulos de rotación de los metaátomos y se han obtenido algunos resultados preliminares de simulación, siendo un tema de investigación actual.

Durante el desarrollo de esta tesis se abrieron dos líneas de investigación más, distintas al tema presentado en este trabajo. La primera estaba relacionada con el diseño de un dispositivo aislante topológico y la segunda con rainbow-trapping electromagnético, como una equivalencia o traslado del fenómeno de ondas acústicas a ondas electromagnéticas. Ambos temas continúan abiertos a la investigación

Appendix A. Huygens-Fresnel Principle

Huygens asserts that every point on a wavefront is itself the source of spherical waves. When combined by Fresnel with the principle of interference, Huygens-Fresnel principle arises. This concept states that these secondary waves emanating from different points interfere with each other and the sum of them forms a new wavefront, explaining the key phenomena of diffraction. Apart from mutual interference, the principle contemplates time periodicity and polarization effects. Both Huygens and Fresnel had to neglect backward parts of the wavelets arbitrarily and the problem for scalar waves was more generally solved by Kirchhoff, who approximated his own rigorous result to obtain his useful diffraction formula [107].

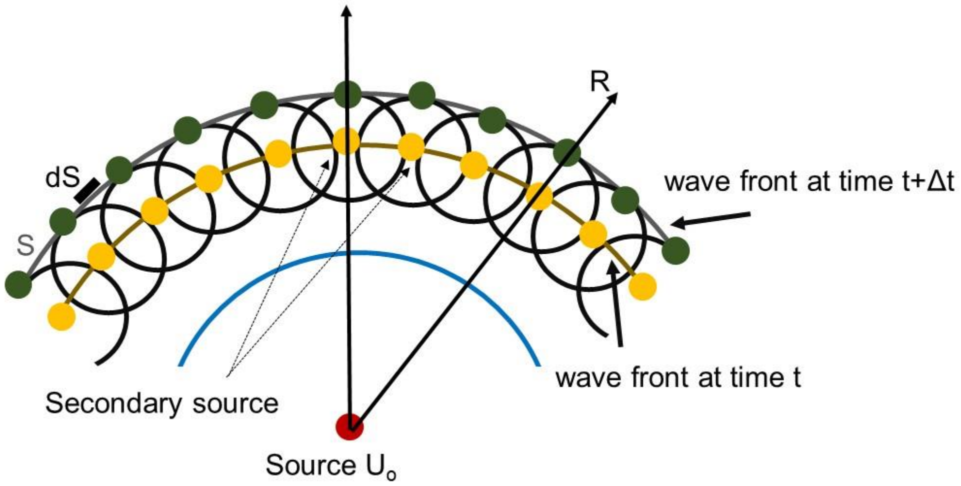

Fig. B.1. Illustration of Huygens-Fresnel principle.

Writing a spherical wave as:

$$U = U_0 e^{j\omega t} \frac{e^{-jk_0 R}}{R}, \quad \text{(B.1)}$$

where $k_0$is the wavenumber in free space, ω the angular frequency, R the distance from the source to the evaluation point and $U_0$the complex amplitude of the source point, the H-F principle can be mathematically written as [108]:

$$dU = U_0 K \frac{e^{-jk_0 R}}{R} dS, \quad \text{(B.2)}$$

where S is a closed surface, K is the Kirchhoff coupling coefficient and dU and dS elementary electric field amplitude and surface area respectively.

In this thesis, we simplify this method by discretizing the radiating surface into an array with a finite number of point sources with coordinates (x_i,y_i,z_i) and applying the arithmetic series of all point sources [109]. All reflections and absorptions are neglected and the amplitudes (A_i) and phases (φ) of the sources are extracted from unit cell rotation analysis performed with CST simulation. The resulting field in each space point is calculating by adding the fields of all sources:

$$A(x,y,x) = \sum_{i=1}^{N} \frac{A_i}{2\, l_i(x,y,z)} \left(1 + \sqrt{1 - \frac{y_i}{{l_i}^2}}\right) e^{j(k_0 l_i(x,y,z)+\varphi)} \tag{B.3}$$

$$l_i(x,y,z) = \sqrt{(x - x_i)^2 + (y - y_i)^2 + (z - z_i)^2} \tag{B.4}$$

where $l_i(x,y,z)$ is the distance between the point source i and point in the space (x,y,z), k_0 is the free space wave vector and (x_i, y_i, z_i) are the position coordinates of the meta-atoms and f_0 the operation frequency.

Appendix B. Linear to circular basis transformation

Being $\begin{bmatrix} a_R \\ a_L \end{bmatrix}$ and $\begin{bmatrix} b_R \\ b_L \end{bmatrix}$ two vectors of a circular basis, where a and b represent the incident and transmitted waves and R and L the right and left-handed circular polarization respectively, the relation between both vectors is given by:

$$\begin{bmatrix} b_R \\ b_L \end{bmatrix} = \bar{\bar{\boldsymbol{M}}} \begin{bmatrix} a_R \\ a_L \end{bmatrix}, \tag{C.1}$$

where $\bar{\bar{\boldsymbol{M}}} = \begin{bmatrix} T_{RR} & T_{RL} \\ T_{LR} & T_{LL} \end{bmatrix}$ is the transmission matrix in circular basis.

The circular polarization vectors can be expressed as a function of linear polarization vectors as follows:

$$\begin{bmatrix} b_R \\ b_L \end{bmatrix} = \bar{\bar{\boldsymbol{C}}} \begin{bmatrix} b_x \\ b_y \end{bmatrix} \tag{C.2}$$

$$\begin{bmatrix} a_R \\ a_L \end{bmatrix} = \bar{\bar{\boldsymbol{C}}} \begin{bmatrix} a_x \\ a_y \end{bmatrix} \tag{C.3}$$

where $\bar{\bar{\boldsymbol{C}}} = \frac{1}{\sqrt{2}} \begin{bmatrix} 1 & -j \\ 1 & j \end{bmatrix}$.

Likewise, two vectors of a linear basis can be expressed as:

$$\begin{bmatrix} b_x \\ b_y \end{bmatrix} = \bar{\bar{\boldsymbol{N}}} \begin{bmatrix} a_x \\ a_y \end{bmatrix}, \tag{C.4}$$

where $\bar{\bar{\boldsymbol{N}}} = \begin{bmatrix} T_{uu} & T_{uv} \\ T_{vu} & T_{vv} \end{bmatrix}$ is the transmission matrix in linear basis.

Substituting equation C.4 in C.2 $$\begin{bmatrix} b_R \\ b_L \end{bmatrix} = \bar{\bar{\boldsymbol{C}}}\, \bar{\bar{\boldsymbol{N}}} \begin{bmatrix} a_x \\ a_y \end{bmatrix} \tag{C.5}$$

and from equation C.3 $$\begin{bmatrix} a_x \\ a_y \end{bmatrix} = \bar{\bar{\boldsymbol{C}}}^{-1} \begin{bmatrix} a_R \\ a_L \end{bmatrix} \tag{C.6}$$

Finally, using C.6 in C.5 the circular basis transmission matrix can be expressed in linear components as:

$$\begin{bmatrix} b_R \\ b_L \end{bmatrix} = \bar{\bar{\boldsymbol{M}}} \begin{bmatrix} a_R \\ a_L \end{bmatrix} = \bar{\bar{\boldsymbol{C}}}\, \bar{\bar{\boldsymbol{N}}} \bar{\bar{\boldsymbol{C}}}^{-1} \begin{bmatrix} a_R \\ a_L \end{bmatrix}$$

$$\bar{\bar{\boldsymbol{M}}} = \begin{pmatrix} T_{RR} & T_{RL} \\ T_{LR} & T_{LL} \end{pmatrix} = \frac{1}{2} \begin{pmatrix} T_{uu} + T_{vv} + j(T_{uv} - T_{vu}) & T_{uu} - T_{vv} - j(T_{uv} + T_{vu}) \\ T_{uu} - T_{vv} + j(T_{uv} + T_{vu}) & T_{uu} + T_{vv} - j(T_{uv} - T_{vu}) \end{pmatrix}$$

Appendix C. Numerical Methods and Equipment

C.1 Numerical Methods

In this work we use CST Microwave Studio™ [110] based on the Finite Integration Technique (FIT) [111] as software package for 3D electromagnetic analysis and design in the high frequency range.

CST Microwave Studio™ contains several different simulation techniques (transient solver, frequency domain solver, integral equation solver, multilayer solver, asymptotic solver, and eigenmode solver) to best suit various applications. Each method in turn supports meshing types best suited for each simulation technique. In this thesis we used transient and frequency domain solvers. The numerical method (FIT) provides a universal spatial discretization scheme applicable to various electromagnetic problems ranging from static field calculations to high frequency applications in time or frequency domain. In order to solve Maxwell's equations in integral form numerically, a finite calculation domain must be defined enclosing the application problem to simulate. The structure is subdivided applying a mesh generation algorithm with the purpose to discretize the structures to be simulated by many small elements (grid cells), which means that the mesh system used is very important. CST has three available mesh types: *hexahedral*, *tetrahedral* and *superficial mesh*. Depending on the solver type used, some of the mesh types will be available. We use the frequency domain solver with tetrahedral mesh in all cases.

Moreover, the simulation software can be driven by MATLAB™ [112], through compiled object-oriented code. This allows to realize a full control over the model and simulation results (create the geometry or save and export the results to different file formats), and perform different operations, such as parameter sweep, optimization of the structure, etc.

C.2 Equipment

For experimental verification of the fabricated devices, we used a Vector Network Analyzer (VNA) MVNA-8-350-4 (Fig. C.2.1(a)), which measures the complex, or vector, transmission and reflection parameters in the millimeter and sub-millimeter frequency domain. It covers the frequency range from 40 GHz up to 1 THz [113].

Fig C.2.1. (a) MVNA-8-350-4. (b) Quasioptical bench.

The VNA allows to obtain both the amplitude and phase of transmitted and reflected signal. In other words, it is possible to obtain the complete response of the tested device, which is located in the signal path of the VNA, in the quasioptical bench, Fig. C.2.1(b). As sources for different bands it has different MVNA heads – active multiplier chains composed of frequency multipliers cascaded with an equivalent medium power waveguide amplifiers delivering 40-1000 GHz. Each millimeter head contains a high-efficiency broadband Schottky device, which is electronically tuned over the full frequency range provide the availability of Full Broadband sources for the bands V (50-75 GHz), W (75-110 GHz), D (110-130 GHz), G (140-220 GHz, WR-5.1), WR-3.4 (220-330 GHz), WR-1.2 (660-1000 GHz). In the MVNA's signal path, the measured millimeter wave signal, which reaches the detector head, is converted by a Schottky diode harmonic mixer to much lower frequency. Then, the converted signal is further processed in the heterodyne vector receiver which uses an internal reference channel. The receiver frequency tuning is achieved with an internal synthesizer.

Besides, in the PBM lens setup, an Agilent VNA E3861C was used (Fig. C.2.2) to obtain the S-parameters of the system. The device has multiple extensions for different bands, covering the range from 0.1 GHz to 550 GHz [114].

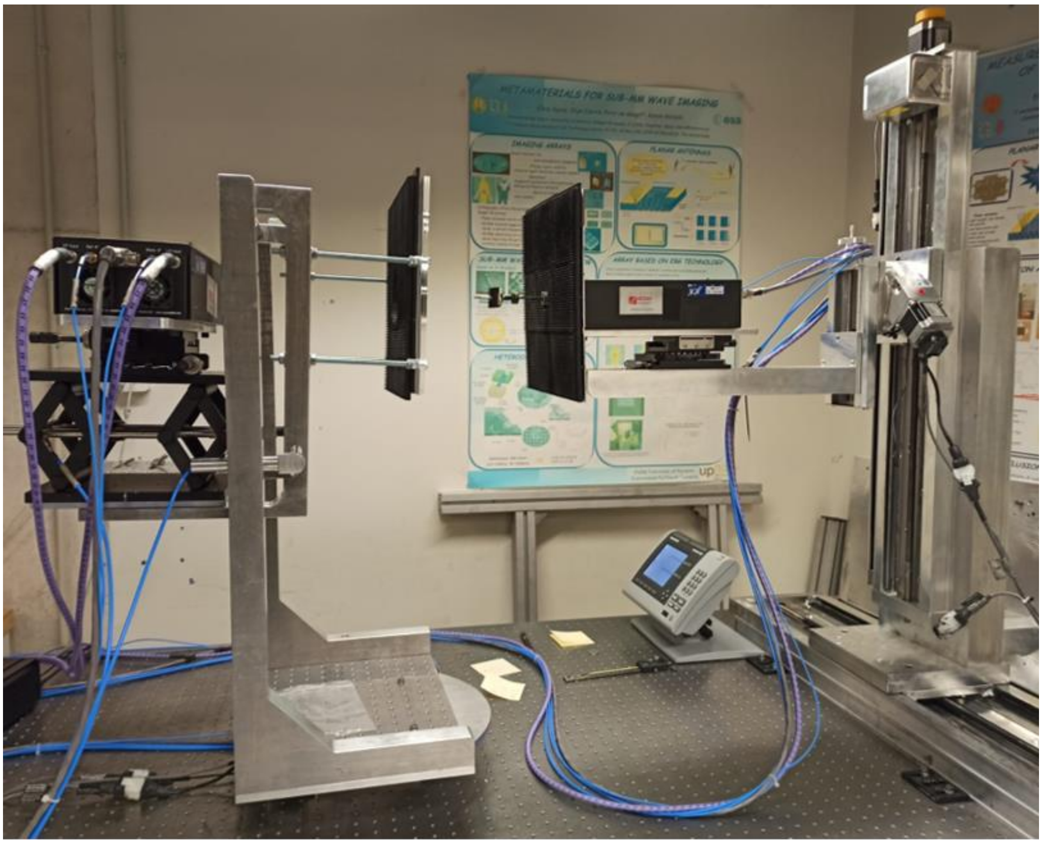

Fig C.2.1. Experimental setup with the extensions of Agilent E3861C VNA for millimeter waves.

Appendix D. Author’s merits

D.1 Journal Publications

1. A. Moreno-Peñarrubia, S. A. Kuznetsov, and M. Beruete, “Ultrathin Subterahertz Half-Wave Plate with High Conversion Efficiency Based on Zigzag Metasurface,” *IEEE Trans. Antennas Propag.*, vol. 68, no. 11, pp. 7700–7704, Nov. 2020.

2. A. Moreno-Peñarrubia, J. Teniente, S. Kuznetsov, B. Orazbayev, and M. Beruete, “Ultrathin and high-efficiency Pancharatnam-Berry phase metalens for millimeter waves,” *Appl. Phys. Lett.*, vol. 118, no. 22, 2021.

3. A. Moreno-Peñarrubia, J. Teniente, S. Kuznetsov, B. Orazbayev, and M. Beruete, “Geometric Phase Metasurface for Lens Antenna System with High Polarization Purity and Efficiency,” *unfinished*, 2022.

D.2 Conference publications

National Conferences

1. A. Moreno-Peñarrubia, S. A. Kuznetsov, and M. Beruete, “Conversor de polarización circular ultra-delgado de alta eficiencia en THz basado en metasuperficies,” XXXIV Simposium Nacional de la Unicón Científica Internacional de Radio, URSI 2019, (2019).

2. A. Moreno-Peñarrubia, J. Teniente, S. Kuznetsov, B. Orazbayev, and M. Beruete, “Highly Efficient Bi-Layer Pancharatnam-Berry HWP Metalensfor MMW Range,” XXXVI Simposium Nacional de la Unicón Científica Internacional de Radio, URSI 2021, (2021).

International Conferences

1. A. Moreno-Peñarrubia, S. A. Kuznetsov, and M. Beruete, “Near-Unity Axial Ratio Ultrathin Zigzag Half-Wave Plate based on Bi-layered Metasurface with High Transmission Efficiency in Terahertz Range,” The International Conference on Metamaterials and Nanophotonics METANANO 2020, (2020).

2. A. Moreno-Peñarrubia, S. A. Kuznetsov, and M. Beruete, “Highly Efficient Ultrathin Zigzag Half-Wave Plate Metasurface in Terahertz Range,” Mediterranean Microwave Simposium 2020, (2020).

3. A. Moreno-Peñarrubia, S. A. Kuznetsov, and M. Beruete, “Ultrathin Zigzag Half-Wave Plate Metasurface with Near-Unity Axial Ratio and High Transmission Efficiency in Terahertz Range,” 14th European Conference on Antennas and Propagation, EuCAP2020, (2020).

4. A. Moreno-Peñarrubia, J. Teniente, S. Kuznetsov, B. Orazbayev, and M. Beruete, “Ultrathin PB Metasurface for Controlling Millimeter Waves,” 45th International Conference on Infrared, Millimeter and Terahertz Waves, IRMMW-THZ 2020, (2020).

5. A. Moreno-Peñarrubia, J. Teniente, S. Kuznetsov, B. Orazbayev, and M. Beruete, “Pancharatnam-Berry Phase Ultrathin HWP for Millimeter Waves,” The 15th International Congress on Artificial Materials for Novel Wave Phenomena, Metamaterials’ 2021, (2021).

References

[1] M. Tonouchi, “Cutting-edge terahertz technology,” *Nat. Photonics*, vol. 1, no. 2, pp. 97–105, 2007.

[2] D. Headland, Y. Monnai, D. Abbott, C. Fumeaux, and W. Withayachumnankul, “Tutorial: Terahertz beamforming, from concepts to realizations,” *APL Photonics*, vol. 3, no. 5, p. 051101, May 2018.

[3] E. K.-E. Peiponen, J. A. Zeitler, M. Kuwata-Gonokami, *Terahertz Spectroscopy and Imaging*, vol. 171. Berlin, Heidelberg: Springer Berlin Heidelberg, 2013.

[4] X. Yang *et al.*, “Biomedical Applications of Terahertz Spectroscopy and Imaging,” *Trends Biotechnol.*, vol. 34, no. 10, pp. 810–824, Oct. 2016.

[5] W. Withayachumnankul, R. Yamada, M. Fujita, and T. Nagatsuma, “All-dielectric rod antenna array for terahertz communications,” *APL Photonics*, vol. 3, no. 5, p. 051707, May 2018.

[6] J. F. Federici *et al.*, “THz imaging and sensing for security applications - Explosives, weapons and drugs,” *Semicond. Sci. Technol.*, vol. 20, no. 7, 2005.

[7] I. Jáuregui-López, P. Rodriguez-Ulibarri, S. A. Kuznetsov, N. A. Nikolaev, and M. Beruete, “THz sensing with anomalous extraordinary optical transmission hole arrays,” *Sensors (Switzerland)*, vol. 18, no. 11, pp. 1–11, 2018.

[8] I. Jáuregui-López, P. Rodríguez-Ulibarri, A. Urrutia, S. A. Kuznetsov, and M. Beruete, “Labyrinth Metasurface Absorber for Ultra-High-Sensitivity Terahertz Thin Film Sensing,” *Phys. Status Solidi - Rapid Res. Lett.*, vol. 12, no. 10, pp. 1–7, 2018.

[9] D. M. Sheen, D. L. McMakin, and T. E. Hall, “Three-dimensional millimeter-wave imaging for concealed weapon detection,” *IEEE Trans. Microw. Theory Tech.*, vol. 49, no. 9, pp. 1581–1592, 2001.

[10] B. Orazbayev, N. Mohammadi Estakhri, A. Alù, and M. Beruete, “Experimental Demonstration of Metasurface-Based Ultrathin Carpet Cloaks for Millimeter Waves,” *Adv. Opt. Mater.*, vol. 5, no. 1, p. 1600606, Jan. 2017.

[11] S. Lin, Y. Wang, Z. Peng, Z. Chen, and F. Hu, “Detection of cancer biomarkers CA125 and CA199 via terahertz metasurface immunosensor,” *Talanta*, vol. 248, no. April, p. 123628, Oct. 2022.

[12] H. Li *et al.*, “High-Resolution Near-Field Imaging and Far-Field Sensing Using a Transmissive Programmable Metasurface,” *Adv. Mater. Technol.*, vol. 7, no. 5, p. 2101067, May 2022.

[13] R. Sharma *et al.*, “Coded-Aperture Computational Millimeter-Wave Image Classifier Using Convolutional Neural Network,” *IEEE Access*, vol. 9, pp. 119830–119844, 2021.

[14] D. R. Smith *et al.*, “Security screening via computational imaging using frequency-diverse metasurface apertures,” in *Passive and Active Millimeter-Wave Imaging XX*, 2017, vol. 10189, p. 101890B.

[15] L. Xie, W. Gao, J. Shu, Y. Ying, and J. Kono, “Extraordinary sensitivity enhancement by metasurfaces in terahertz detection of antibiotics,” *Sci. Rep.*, vol. 5, no. 1, p. 8671, Aug. 2015.

[16] X. Liu *et al.*, “Terahertz metasurfaces based on bound states in the continuum (BIC) for high-sensitivity refractive index sensing,” *Optik (Stuttg).*, vol. 261, no. May, p. 169248, Jul. 2022.

[17] G. Valušis, A. Lisauskas, H. Yuan, W. Knap, and H. G. Roskos, “Roadmap of Terahertz Imaging 2021,” *Sensors*, vol. 21, no. 12, p. 4092, Jun. 2021.

[18] W. Köhler *et al.*, “Non-destructive investigation of paintings with THz-radiation,” *9th ECNDT*, no. January 2006, pp. 1–7, 2006.

[19] D. A. Sehrai *et al.*, “Metasurface-Based Wideband MIMO Antenna for 5G Millimeter-Wave Systems,” *IEEE Access*, vol. 9, no. September, pp. 125348–125357, 2021.

[20] B. Feng, X. He, J.-C. Cheng, and C.-Y.-D. Sim, “Dual-Wideband Dual-Polarized Metasurface Antenna Array for the 5G Millimeter Wave Communications Based on Characteristic Mode Theory,” *IEEE Access*, vol. 8, pp. 21589–21601, 2020.

[21] W. Withayachumnankul and D. Abbott, “Metamaterials in the Terahertz Regime,” *IEEE Photonics J.*, vol. 1, no. 2, pp. 99–118, Aug. 2009.

[22] D. R. Smith and J. B. Pendry, “Homogenization of metamaterials by field averaging (invited paper),” *J. Opt. Soc. Am. B*, vol. 23, no. 3, p. 391, Mar. 2006.

[23] R. Marqués, F. Martin, and M. Sorolla, *Metamaterials with Negative Parameters*. Hoboken, NJ, USA: John Wiley & Sons, Inc., 2007.

[24] S. B. Glybovski, S. A. Tretyakov, P. A. Belov, Y. S. Kivshar, and C. R. Simovski, “Metasurfaces: From microwaves to visible,” *Phys. Rep.*, vol. 634, pp. 1–72, May 2016.

[25] J. Jung, H. Park, J. Park, T. Chang, and J. Shin, “Broadband metamaterials and metasurfaces: a review from the perspectives of materials and devices,” *Nanophotonics*, vol. 9, no. 10, pp. 3165–3196, Aug. 2020.

[26] K. Achouri and C. Caloz, “Design, concepts, and applications of electromagnetic metasurfaces,” *Nanophotonics*, vol. 7, no. 6, pp. 1095–1116, Jun. 2018.

[27] X. Zang *et al.*, “Metasurfaces for manipulating terahertz waves,” *Light Adv. Manuf.*, vol. 2, no. 2, p. 148, 2021.

[28] B. Ferguson and X.-C. Zhang, “Materials for terahertz science and technology,” *Nat. Mater.*, vol. 1, no. 1, pp. 26–33, Sep. 2002.

[29] N. Oshima, K. Hashimoto, S. Suzuki, and M. Asada, “Terahertz Wireless Data Transmission With Frequency and Polarization Division Multiplexing Using Resonant-Tunneling-Diode Oscillators,” *IEEE Trans. Terahertz Sci. Technol.*, vol. 7, no. 5, pp. 593–598, Sep. 2017.

[30] R. T. Ako, W. S. L. Lee, S. Atakaramians, M. Bhaskaran, S. Sriram, and W. Withayachumnankul, “Ultra-wideband tri-layer transmissive linear polarization converter for terahertz waves,” *APL Photonics*, vol. 5, no. 4, p. 046101, Apr. 2020.

[31] W. S. L. Lee *et al.*, “Dielectric-resonator metasurfaces for broadband terahertz quarter- and half-wave mirrors,” *Opt. Express*, vol. 26, no. 11, p. 14392, May 2018.

[32] C.-C. Chang, Z. Zhao, D. Li, A. J. Taylor, S. Fan, and H.-T. Chen, “Broadband Linear-to-Circular Polarization Conversion Enabled by Birefringent Off-Resonance Reflective Metasurfaces,” *Phys. Rev. Lett.*, vol. 123, no. 23, p. 237401, Dec. 2019.

[33] C. Pfeiffer and A. Grbic, “Millimeter-Wave Transmitarrays for Wavefront and Polarization Control,” *IEEE Trans. Microw. Theory Tech.*, vol. 61, no. 12, pp. 4407–4417, Dec. 2013.

[34] R. T. Ako, W. S. L. Lee, M. Bhaskaran, S. Sriram, and W. Withayachumnankul, “Broadband and wide-angle reflective linear polarization converter for terahertz waves,” *APL Photonics*, vol. 4, no. 9, p. 096104, Sep. 2019.

[35] S. M. A. Momeni Hasan Abadi and N. Behdad, “A broadband, circular-polarization selective surface,” *J. Appl. Phys.*, vol. 119, no. 24, p. 244901, Jun. 2016.

[36] C. Pfeiffer and A. Grbic, “Bianisotropic Metasurfaces for Optimal Polarization Control: Analysis and Synthesis,” *Phys. Rev. Appl.*, vol. 2, no. 4, p. 044011, Oct. 2014.

[37] X. You, C. Fumeaux, and W. Withayachumnankul, “Tutorial on broadband transmissive metasurfaces for wavefront and polarization control of terahertz waves,” *J. Appl. Phys.*, vol. 131, no. 6, p. 061101, Feb. 2022.

[38] L. Cong, N. Xu, J. Gu, R. Singh, J. Han, and W. Zhang, “Highly flexible broadband terahertz metamaterial quarter-wave plate,” *Laser Photon. Rev.*, vol. 8, no. 4, pp. 626–632, Jul. 2014.

[39] X. You *et al.*, “Broadband terahertz transmissive quarter-wave metasurface,” *APL Photonics*, vol. 5, no. 9, p. 096108, Sep. 2020.

[40] M. Jia *et al.*, “Efficient manipulations of circularly polarized terahertz waves with transmissive metasurfaces,” *Light Sci. Appl.*, vol. 8, no. 1, p. 16, Dec. 2019.

[41] C. Menzel, C. Rockstuhl, and F. Lederer, “Advanced Jones calculus for the classification of periodic metamaterials,” *Phys. Rev. A*, vol. 82, no. 5, p. 053811, Nov. 2010.

[42] N. P. Armitage, “Constraints on Jones transmission matrices from time-reversal invariance and discrete spatial symmetries,” *Phys. Rev. B*, vol. 90, no. 3, p. 035135, Jul. 2014.

[43] L. Peng, X.-F. Li, X. Jiang, and S. Li, “A Novel THz Half-Wave Polarization Converter for Cross-Polarization Conversions of Both Linear and Circular Polarizations and Polarization Conversion Ratio Regulating by Graphene,” *J. Light. Technol.*, vol. 36, no. 19, pp. 4250–4258, Oct. 2018.

[44] X. Zhang, D. Kong, Y. Yuan, S. Mei, L. Wang, and G. Wang, “Broadband and dispersion-free reflective silver metasurfaces as half-wave plate and vortex-beam generator,” *Opt. Commun.*, vol. 465, no. February, p. 125561, Jun. 2020.

[45] Y. Nakata, Y. Taira, T. Nakanishi, and F. Miyamaru, “Freestanding transparent terahertz half-wave plate using subwavelength cut-wire pairs,” *Opt. Express*, vol. 25, no. 3, p. 2107, Feb. 2017.

[46] D. Headland *et al.*, “Dielectric Resonator Reflectarray as High-Efficiency Nonuniform Terahertz Metasurface,” *ACS Photonics*, vol. 3, no. 6, pp. 1019–1026, Jun. 2016.

[47] T. Niu *et al.*, “Experimental demonstration of reflectarray antennas at terahertz frequencies,” *Opt. Express*, vol. 21, no. 3, p. 2875, Feb. 2013.

[48] Q. Cheng *et al.*, “Broadband achromatic metalens in terahertz regime,” *Sci. Bull.*, vol. 64, no. 20, pp. 1525–1531, Oct. 2019.

[49] N. Yu and F. Capasso, “Flat optics with designer metasurfaces,” *Nat. Mater.*, vol. 13, no. 2, pp. 139–150, Feb. 2014.

[50] S. M. Kamali, E. Arbabi, A. Arbabi, and A. Faraon, “A review of dielectric optical metasurfaces for wavefront control,” *Nanophotonics*, vol. 7, no. 6, pp. 1041–1068, Jun. 2018.

[51] H.-T. Chen, A. J. Taylor, and N. Yu, “A review of metasurfaces: physics and applications,” *Reports Prog. Phys.*, vol. 79, no. 7, p. 076401, Jul. 2016.

[52] E. B. Lima, S. A. Matos, J. R. Costa, C. A. Fernandes, and N. J. G. Fonseca, “Circular Polarization Wide-Angle Beam Steering at Ka-Band by In-Plane Translation of a Plate Lens Antenna,” *IEEE Trans. Antennas Propag.*, vol. 63, no. 12, pp. 5443–5455, Dec. 2015.

[53] H. Yi, S. Qu, and C. H. Chan, “Low-cost two-layer terahertz transmit array,” *Electron. Lett.*, vol. 53, no. 12, pp. 789–791, Jun. 2017.

[54] C. Song, L. Zhu, and L. Pan, “Design of transmittarray feed by filtering dielectric antenna for <scp>5G</scp>,” *Int. J. RF Microw. Comput. Eng.*, vol. 30, no. 7, pp. 1–8, Jul. 2020.

[55] C.-C. Chang, D. Headland, D. Abbott, W. Withayachumnankul, and H.-T. Chen, “Demonstration of a highly efficient terahertz flat lens employing tri-layer metasurfaces,” *Opt. Lett.*, vol. 42, no. 9, p. 1867, May 2017.

[56] F. Aieta *et al.*, “Aberration-Free Ultrathin Flat Lenses and Axicons at Telecom Wavelengths Based on Plasmonic Metasurfaces,” *Nano Lett.*, vol. 12, no. 9, pp. 4932–4936, Sep. 2012.

[57] M. R. Akram, C. He, and W. Zhu, “Bi-layer metasurface based on Huygens’ principle for high gain antenna applications,” *Opt. Express*, vol. 28, no. 11, p. 15844, May 2020.

[58] H. Li, G. Wang, T. Cai, J. Liang, and H. Hou, “Bifunctional circularly-polarized lenses with simultaneous geometrical and propagating phase control metasurfaces,” *J. Phys. D. Appl. Phys.*, vol. 52, no. 46, p. 465105, Nov. 2019.

[59] S. Pancharatnam, “Generalized theory of interference and its applications,” *Proc. Indian Acad. Sci. - Sect. A*, vol. 44, no. 6, pp. 398–417, Dec. 1956.

[60] M. V Berry and P. R. S. L. A, “Quantal phase factors accompanying adiabatic changes,” *Proc. R. Soc. London. A. Math. Phys. Sci.*, vol. 392, no. 1802, pp. 45–

57, Mar. 1984.

[61] W. Mo, X. Wei, K. Wang, Y. Li, and J. Liu, “Ultrathin flexible terahertz polarization converter based on metasurfaces,” *Opt. Express*, vol. 24, no. 12, p. 13621, Jun. 2016.

[62] F. Ding, Z. Wang, S. He, V. M. Shalaev, and A. V. Kildishev, “Broadband High-Efficiency Half-Wave Plate: A Supercell-Based Plasmonic Metasurface Approach,” *ACS Nano*, vol. 9, no. 4, pp. 4111–4119, Apr. 2015.

[63] X. Ding *et al.*, “Ultrathin Pancharatnam-Berry Metasurface with Maximal Cross-Polarization Efficiency,” *Adv. Mater.*, vol. 27, no. 7, pp. 1195–1200, Feb. 2015.

[64] P. Naseri, F. Khosravi, and P. Mousavi, “Antenna-Filter-Antenna-Based Transmit-Array for Circular Polarization Application,” *IEEE Antennas Wirel. Propag. Lett.*, vol. 16, no. December 2018, pp. 1389–1392, 2017.

[65] Z. Li, J. Su, and Z. Li, “A novel high-gain circularly polarized planar lens antenna based on the element rotation method,” in *2017 Sixth Asia-Pacific Conference on Antennas and Propagation (APCAP)*, 2017, pp. 1–3.

[66] L. Shao-he, L. Jiu-sheng, and S. Jian-zhong, “Terahertz wave front manipulation based on Pancharatnam-Berry coding metasurface,” *Opt. Mater. Express*, vol. 9, no. 3, p. 1118, Mar. 2019.

[67] M. I. Khan and F. A. Tahir, “A compact half and quarter-wave plate based on bi-layer anisotropic metasurface,” *J. Phys. D. Appl. Phys.*, vol. 50, no. 43, p. 43LT04, Nov. 2017.

[68] A. Moreno-Peñarrubia, S. A. Kuznetsov, and M. Beruete, “Ultrathin Subterahertz Half-Wave Plate With High Conversion Efficiency Based on Zigzag Metasurface,” *IEEE Trans. Antennas Propag.*, vol. 68, no. 11, pp. 7700–7704, Nov. 2020.

[69] Z. H. Jiang, Y. Zhang, J. Xu, Y. Yu, and W. Hong, “Integrated Broadband Circularly Polarized Multibeam Antennas Using Berry-Phase Transmit-Arrays for Ka-Band Applications,” *IEEE Trans. Antennas Propag.*, vol. 68, no. 2, pp. 859–872, Feb. 2020.

[70] Y. Liu, A. Zhang, Z. Xu, S. Xia, and H. Shi, “Wideband and low-profile transmitarray antenna using transmissive metasurface,” *J. Appl. Phys.*, vol. 125, no. 4, p. 045103, Jan. 2019.

[71] M. J. Veljovic and A. K. Skrivervik, “Circularly Polarized Transmitarray Antenna for CubeSat Intersatellite Links in K -Band,” *IEEE Antennas Wirel. Propag. Lett.*, vol. 19, no. 10, pp. 1749–1753, Oct. 2020.

[72] R. Mao, G. Wang, T. Cai, K. Liu, D. Wang, and B. Wu, “Ultra-thin and high-efficiency full-space Pancharatnam-Berry metasurface,” *Opt. Express*, vol. 28, no. 21, p. 31216, Oct. 2020.

[73] M. S. Kong *et al.*, “Terahertz radiation using log-spiral-based low-temperature-grown InGaAs photoconductive antenna pumped by mode-locked Yb-doped fiber laser,” *Opt. Express*, vol. 24, no. 7, p. 7037, Apr. 2016.

[74] D.-Q. Zhang, F.-Z. Shu, Z.-W. Jiao, and H.-W. Wu, “Tunable wave plates based

on phase-change metasurfaces," *Opt. Express*, vol. 29, no. 5, p. 7494, Mar. 2021.

[75] Q. Yang *et al.*, "Polarization-Sensitive Dielectric Membrane Metasurfaces," *Adv. Opt. Mater.*, vol. 8, no. 20, p. 2000555, Oct. 2020.

[76] D. Wang, Y. Gu, Y. Gong, C.-W. Qiu, and M. Hong, "An ultrathin terahertz quarter-wave plate using planar babinet-inverted metasurface," *Opt. Express*, vol. 23, no. 9, p. 11114, May 2015.

[77] B. Yang, W.-M. Ye, X.-D. Yuan, Z.-H. Zhu, and C. Zeng, "Design of ultrathin plasmonic quarter-wave plate based on period coupling," *Opt. Lett.*, vol. 38, no. 5, p. 679, Mar. 2013.

[78] T. Zeghdoudi, Z. Kebci, A. Mezeghrane, A. Belkhir, and F. I. Baida, "Half-wave plate based on a birefringent metamaterial in the visible range," *Opt. Commun.*, vol. 487, no. October 2020, p. 126804, May 2021.

[79] H. Gu, X. Chen, C. Zhang, H. Jiang, and S. Liu, "Study of the retardance of a birefringent waveplate at tilt incidence by Mueller matrix ellipsometer," *J. Opt.*, vol. 20, no. 1, p. 015401, Jan. 2018.

[80] R. C. Jones, "A New Calculus for the Treatment of Optical Systems I Description and Discussion of the Calculus," *J. Opt. Soc. Am.*, vol. 31, no. 7, p. 488, Jul. 1941.

[81] V. S. Asadchy, A. Díaz-Rubio, and S. A. Tretyakov, "Bianisotropic metasurfaces: physics and applications," *Nanophotonics*, vol. 7, no. 6, pp. 1069–1094, Jun. 2018.

[82] J. E. Roy and L. Shafai, "Reciprocal circular-polarization-selective surface," *IEEE Antennas Propag. Mag.*, vol. 38, no. 6, pp. 18–33, Dec. 1996.

[83] X. Wu, Y. Meng, L. Wang, J. Tian, S. Dai, and W. Wen, "Anisotropic metasurface with near-unity circular polarization conversion," *Appl. Phys. Lett.*, vol. 108, no. 18, p. 183502, May 2016.

[84] P. E. Sieber and D. H. Werner, "Infrared broadband quarter-wave and half-wave plates synthesized from anisotropic Bézier metasurfaces," *Opt. Express*, vol. 22, no. 26, p. 32371, Dec. 2014.

[85] M. R. Akram, M. Q. Mehmood, X. Bai, R. Jin, M. Premaratne, and W. Zhu, "High Efficiency Ultrathin Transmissive Metasurfaces," *Adv. Opt. Mater.*, vol. 7, no. 11, p. 1801628, Jun. 2019.

[86] W. Luo, S. Sun, H.-X. Xu, Q. He, and L. Zhou, "Transmissive Ultrathin Pancharatnam-Berry Metasurfaces with nearly 100% Efficiency," *Phys. Rev. Appl.*, vol. 7, no. 4, p. 044033, Apr. 2017.

[87] F. Wang, Z. Li, W. Wang, L. Wu, and Y. Wei, "Highly Efficient Polarization Control Based on All-Dielectric Metasurfaces," *IEEE Access*, vol. 10, pp. 32172–32179, 2022.

[88] Y. He and G. V. Eleftheriades, "Design of thin infrared quarter-wave and half-wave plates using antenna-array sheets," *Opt. Express*, vol. 21, no. 21, p. 24468, Oct. 2013.

[89] X.-P. Dong, J.-R. Cheng, F. Fan, S.-T. Xu, X.-H. Wang, and S.-J. Chang,

“Wideband sub-THz half-wave plate using 3D-printed low-index metagratings with superwavelength lattice,” *Opt. Express*, vol. 27, no. 1, p. 202, Jan. 2019.

[90] J. D. Baena, J. P. del Risco, A. P. Slobozhanyuk, S. B. Glybovski, and P. A. Belov, “Self-complementary metasurfaces for linear-to-circular polarization conversion,” *Phys. Rev. B*, vol. 92, no. 24, p. 245413, Dec. 2015.

[91] J. Pablo, J. Domingo, and B. Doello, “Metasuperficies para filtrado y absorción en el rango de microondas,” 2016.

[92] F. Falcone *et al.*, “Babinet Principle Applied to the Design of Metasurfaces and Metamaterials,” *Phys. Rev. Lett.*, vol. 93, no. 19, p. 197401, Nov. 2004.

[93] M. Navarro-Cia, S. A. Kuznetsov, M. Aznabet, M. Beruete, F. Falcone, and M. S. Ayza, “Route for Bulk Millimeter Wave and Terahertz Metamaterial Design,” *IEEE J. Quantum Electron.*, vol. 47, no. 3, pp. 375–385, Mar. 2011.

[94] E. Abbe, “VII.-On the Estimation of Aperture in the Microscope.,” *J. R. Microsc. Soc.*, vol. 1, no. 3, pp. 388–423, Jun. 1881.

[95] E. Abbe, “Beiträge zur Theorie des Mikroskops und der mikroskopischen Wahrnehmung,” *Arch. für Mikroskopische Anat.*, vol. 9, no. 1, pp. 413–468, Dec. 1873.

[96] Rayleigh, “XXXI. Investigations in optics, with special reference to the spectroscope,” *London, Edinburgh, Dublin Philos. Mag. J. Sci.*, vol. 8, no. 49, pp. 261–274, Oct. 1879.

[97] E. A. ASH and G. NICHOLLS, “Super-resolution Aperture Scanning Microscope,” *Nature*, vol. 237, no. 5357, pp. 510–512, Jun. 1972.

[98] J. B. Pendry, “Negative Refraction Makes a Perfect Lens,” *Phys. Rev. Lett.*, vol. 85, no. 18, pp. 3966–3969, Oct. 2000.

[99] V. Torres *et al.*, “Experimental Demonstration of a Millimeter-Wave Metallic ENZ Lens Based on the Energy Squeezing Principle,” *IEEE Trans. Antennas Propag.*, vol. 63, no. 1, pp. 231–239, Jan. 2015.

[100] V. Pacheco-Peña, B. Orazbayev, V. Torres, M. Beruete, and M. Navarro-Cía, “Ultra-compact planoconcave zoned metallic lens based on the fishnet metamaterial,” *Appl. Phys. Lett.*, vol. 103, no. 18, p. 183507, Oct. 2013.

[101] P. Lalanne and P. Chavel, “Metalenses at visible wavelengths: past, present, perspectives,” *Laser Photon. Rev.*, vol. 11, no. 3, p. 1600295, May 2017.

[102] X. Yi, T. Su, B. Wu, J.-Z. Chen, L. Yang, and X. Li, “A Double-Layer Highly Efficient and Wideband Transmitarray Antenna,” *IEEE Access*, vol. 7, pp. 23285–23290, 2019.

[103] L. Wang, S. Liu, X. Kong, Y. Wen, and X. Liu, “Broadband vortex beam generating for multi-polarisations based on a single-layer quasi-spiral metasurface,” *Electron. Lett.*, vol. 55, no. 22, pp. 1168–1170, Oct. 2019.

[104] S. Jiang, C. Chen, H. Zhang, and W. Chen, “Achromatic electromagnetic metasurface for generating a vortex wave with orbital angular momentum (OAM),” *Opt. Express*, vol. 26, no. 5, p. 6466, Mar. 2018.

[105] A. Arbabi and A. Faraon, “Fundamental limits of ultrathin metasurfaces,” *Sci. Rep.*, vol. 7, no. 1, p. 43722, May 2017.

[106] A. Moreno-Peñarrubia, S. A. Kuznetsov, and M. Beruete, “Ultrathin Subterahertz Half-Wave Plate With High Conversion Efficiency Based on Zigzag Metasurface,” *IEEE Trans. Antennas Propag.*, vol. 68, no. 11, pp. 7700–7704, Nov. 2020.

[107] D. A. B. Miller, “Huygens’s wave propagation principle corrected,” *Opt. Lett.*, vol. 16, no. 18, p. 1370, Sep. 1991.

[108] I. V. Minin and O. V. Minin, *Diffractional Optics of Millimetre Waves*. CRC Press, 2004.

[109] B. Orazbayev, V. Pacheco-Peña, M. Beruete, and M. Navarro-Cía, “Exploiting the dispersion of the double-negative-index fishnet metamaterial to create a broadband low-profile metallic lens,” *Opt. Express*, vol. 23, no. 7, p. 8555, Apr. 2015.

[110] “CST Microwave Studio.” [Online]. Available: https://www.cst.com/products/cstmws. [Accessed: 08-Dec-2018].

[111] T. Weiland, “A Discretization Method for the Solution of Maxwell’s Equations for Six-Component Fields,” *Arch. Elektron. und Uebertragungstechnik*, vol. 31, pp. 116–120, Feb. 1977.

[112] “MATLAB.” [Online]. Available: https://www.mathworks.com/products/matlab.html.

[113] “AB Millimetre,” *http://www.abmillimetre.com/*. [Online]. Available: http://www.abmillimetre.com/.

[114] “Agilent Technologies.” [Online]. Available: https://www.agilent.com/Agilent404?s=https://www.agilent.com/home.